VARIABLE SHEARING HOLOGRAPHY

by

Prithiviraj Shanmugam

A dissertation submitted to the faculty of
The University of North Carolina at Charlotte
in partial fulfillment of the requirements
for the degree of Doctor of Philosophy in
Mechanical Engineering

Charlotte

2023

Approved by:

Dr. Konstantinos Falaggis

Dr. Matthew A Davies

Dr. Jimmie Miller

Dr. Taufiquar Khan

ABSTRACT

PRITHIVIRAJ SHANMUGAM. Variable Shearing Holography. (Under the direction of DR. KONSTANTINOS FALAGGIS)

From the perspective of manufacturing, it is not always ideal to use conventional methods of surface and optical metrology. Many optical metrology systems like interferometry use a stable temperature-controlled environment in a laboratory setting as they are sensitive to such disturbances. The main contributing factor to these levels of sensitivity is the presence of a reference mirror in non-common path configurations. In many interferometric systems, interference patterns are generated by overlapping the wavefield generated from the object being measured with that generated from a reference mirror. Different algorithms can be used further by modulating the interference patterns to generate the surface maps. Similar setups and algorithms could be used to not only generate the surface maps, but also the object complex wavefield which extends its applications in digital holography. The goal of this research is to develop interferometric holography systems that are robust to environmental effects and suitable for in-situ metrology in manufacturing processes. Part 1 of this dissertation focuses on developing a lateral shear interferometric holography system using a pair of geometric-phase (GP) gratings. Two designs are proposed which allowed for different shear selection strategies. The proposed designs are robust to environmental effects by virtue of its design as a self-referenced and common-path configuration. A polarized camera sensor is used to record the interferograms with different phase shifts. Using an alternating projection algorithm, the recorded intensity maps are used to estimate the object wavefield. The errors generated by the algorithm are studied as a function of the shears selected to record the interferograms using

synthetic intensity maps for both designs. The correlation is investigated using spatial and frequency information density functions and the errors generated by both designs are compared. Part 2 investigates the limitations of selected shears from the perspective of spatial information density function. The major outcome from Parts 1 and 2 is the proof that the shear selection strategies, the shear amounts, and the shear orientations affect the wavefield reconstruction. This leads to Part 3 of the dissertation which focuses on the optimal selection of shears for this system. Due to the complexity in the equations that govern the effect of shears on the reconstruction of different surface frequencies, a statistical approach was opted to optimize the shears based on simulations that reconstructed a defocused point source wavefield. A point source wavefield is used for these simulations because it is the ideal wavefield demonstrating the reconstruction of all possible frequencies within the field of view. The results were compared to frequency information density maps to correlate the results. Parts 1,2 and 3 show a complete work starting from exploring designs to identifying optimal shear settings for a coherent digital holography system to measure transmissive and reflective samples. Part 4 shows a secondary application for this system that uses the GP grating pairs to make a fringe projection system that is suitable for diffused surfaces. The system provides flexibility to adjust the characteristics of the projected fringes easily by changing the space between the gratings and the grating pair orientation. Example measurements are presented, and the capabilities of the setup are demonstrated. The proposed design can produce adjustable fringe patterns with fringe spacing varying from large values to as small as sub-millimeter distances. The fringe orientation can also be changed, and the patterns can be projected on objects of wide range of sizes without losing the fringe contrast.

DEDICATION

I would like to dedicate this work to my parents who have constantly supported and motivated me to get to the finish line. I wouldn’t be who I am without them. I would also like to dedicate this work to my advisor/mentor, Dr. Konstantinos Falaggis, who has constantly motivated me and has been a source of inspiration.

ACKNOWLEDGEMENTS

I would like to start by expressing my deepest gratitude to my mentor and dissertation advisor Dr. Konstantinos Falaggis. His continuous guidance, dedicated support and encouragement were elemental in me reaching the finish line in this journey. I am grateful to him for his passion and support in improving my research skills, and knowledge in the field of optical metrology and optimization processes. His research approach through scrum played a key role in experiencing an effective and exponential learning curve in this field. I would like to extend my thanks to Dr. Jimmie Miller, Dr. Matthew A. Davies and Dr. Christopher J. Evans for the numerous conversations and technical insights over the years in my Ph.D. program. I would also like to thank Dr. Rosario Porras for her insights in the project from the perspective of optical science and presentation skills. I thank former UNCC students, Alyson Light and Avery Turley for their technical insights and training at the initial stages of the project. Special thanks to all my lab partners, Ana Hiza Ramirez-Andrade, John Hawthorn and Sevda Mamaghani for the endless discussions and assistance. I would like to extend my thanks to Clark Hovis, Dhanooj Bobba, Jacob Brooks, Jesse Redford and Rehab Abdelazim for all the discussions in the office and also through the ASPE student chapter. I am grateful for the infrastructure and labs made available through the Center for Precision Metrology and also for the trainings provided by Greg Caskey. I would like to thank Jonathan Koerber and Dr. Thomas Suleski for collaborative works through II-VI foundation. I would also like to thank Sujithra Chandrasekaran and Dr. Ahmed El-Ghannam for the opportunity to do collaborative works.

This project was sponsored by the Center for Precision Metrology. I would like to thank the Center for Precision Metrology and its Director, Dr. Edward Morse for financial support without which this dissertation wouldn’t have been possible. I would also like to thank the Center for

Freeform Optics and its Directors, Dr. Thomas Suleski, Dr. Konstantinos Falaggis, Dr. Jannick Rolland and Dr. John Lambropoulos for the financial support and opportunity to work on other projects in the course of the Ph.D. program.

TABLE OF CONTENTS

LIST OF TABLES

LIST OF FIGURES

LIST OF ABBREVIATIONS

GP	Geometric Phase
LP	Linear Polarization
LCP	Left Circular Polarization
RCP	Right Circular Polarization
rad	Radians
a.u.	Arbitrary units
px	Pixels
FIDF	Frequency Information Density Function
SIDF	Spatial Information Density Function

CHAPTER 1: BACKGROUND AND MOTIVATION

1.1 Interferometry and Holography

Quantitative measurement of surface is an important topic in many fields such as surface engineering, imaging bio-samples, optical fabrication, etc. in a small scale and can also be extended to a large scale such as for reverse engineering and in manufacturing and assembly. A complex wavefield consists of an amplitude component and a phase component. For many optical metrology techniques, an understanding of both, the amplitude and phase properties of a complex wavefield is important. When imaging an object, the depth information of the object is encoded in the phase of the complex wavefield, and different mechanisms are often employed to retrieve the phase information to build the height map of the object under measurement. One of the most common methods for phase retrieval or height map reconstruction is interferometry. Many conventional interferometric systems use a reference mirror to generate a reference wavefield and combine it with the object wavefield to produce interference patterns. The interference patterns can be modulated through phase modulation and the object surface information can be retrieved through different algorithms. The common option found in commercial instruments for smooth and polished surfaces is the use of phase-shifting mechanisms and algorithms. These are often available in Michelson, Fizeau, or Mach-Zehnder configurations. These configurations can be used with constant phase shifts [1] or using random phase shifts [2,3]. The phase shifts are introduced by changing the optical path distance by moving the reference mirror using a piezoelectric transducer (PZT) [4]. An alternative approach is to introduce a phase shift by manipulating the polarization states of the overlapping beams [5–7]. The general idea is that the object and reference beams are orthogonally and circularly polarized, and then brought to the same state of linear polarization. This induces a phase shift between the two beams which produces interference patterns on the camera plane. Changing the angle of linear polarization changes the phase shift between the interfering beams and a phase shifting algorithm can be applied to recover the phase map.

Holography, according to Peter de Groot et. al. [8], is a two-step process: (a) Recording the amplitude and phase of a propagating wavefield as intensity images using interference, and (b) reconstruction of the propagating wavefield from the recorded intensity images using optics or digital reconstruction algorithms. The above-mentioned interferometric systems can be further modified to record both phase and amplitude and estimate complex wavefields. This expands their applications in the field of digital holography [9,10] as the estimated complex wavefields can be further processed with wave propagation algorithms like angular spectrum [11,12] and perform numerical refocusing. Another approach that can measure both smooth and rough surfaces is coherence scanning interferometry [13–16]. This method uses an incoherent light source of a known wavelength bandwidth and characterizes the object surface by scanning along the vertical axis and analyzing the fringe modulation within the coherence envelope of the light source. This is often used with a Mirau or a Michelson configuration. A common limitation in all these systems is that they use a separate reference mirror to generate the reference wave, and so all these designs are sensitive to environmental disturbances. These systems need a temperature-controlled laboratory setting and are not suitable for harsh environments such as in-situ metrology. The use of systems that do not rely on a reference wave is often found as suitable solutions for implementing in-situ metrology, especially in environments that are prone to experience more vibrations.

1.2 Shear interferometry

Shear interferometry is an example technique that does not rely on reference wave generation. In shear interferometry, the system creates a copy of the object wavefield, and one or both object wavefields are modulated differently and overlapped to produce interference patterns. Depending on how the object beams are modulated, different types of shear interferometry systems exist. Some of the different shear configurations that can be found across the literature are summarized in [4,17]. Lateral shear interferometry systems are more common and can be easily realized by modifying conventional interferometry designs such as Michelson and Mach-Zehnder [4]. In a lateral shearing configuration, a copy of the object wavefield is created and either one or both object wavefields are laterally displaced relative to each other through different shearing mechanisms. Figure 1.1 shows an example of how conventional designs can be modified to function as a shear interferometer.

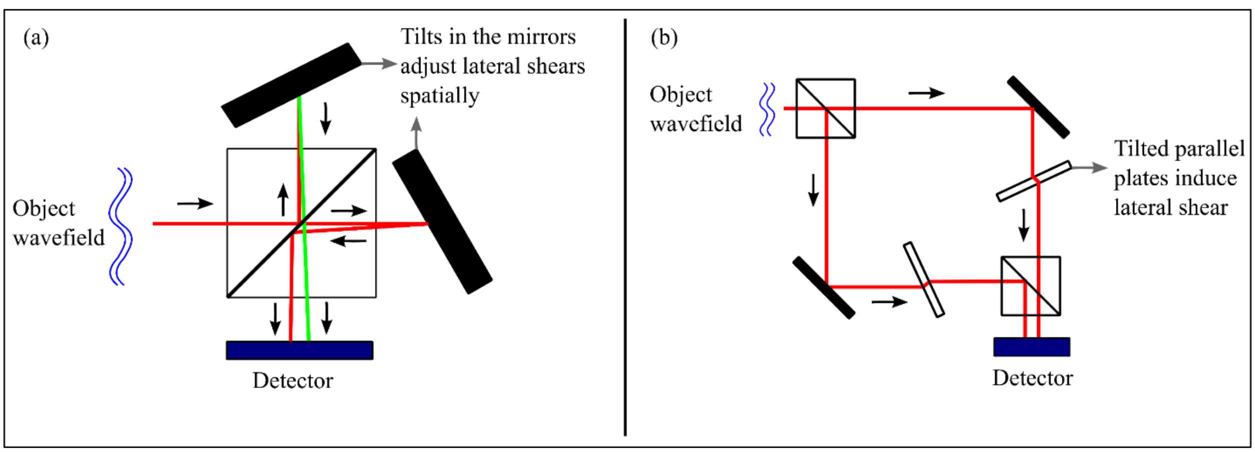

FIGURE 1.1: Modification of conventional designs to perform shear interferometry.
(a) Michelson interferometry design, (b) Mach-Zehnder design.

Since a separate reference beam is not generated in these systems, it is possible to design these systems in common path configurations [18] which makes the system robust and suitable for harsh environments. A shear interferometry system can be implemented in two methods which decide which type of algorithm can be used to evaluate the phase information as an interferometer or to evaluate the complex wavefield as a holography system. The first approach is to create a copy of the object wavefield and modulate the copy while the original wavefield is left undisturbed. The shear interferometry setup presented by Falldorf et. al. in [19–21] follows this approach where the object wavefield was sheared using a spatial light modulator (SLM). The spatial light modulator functioned as both the shearing element as well as for introducing phase shift when recording the interferograms. The object wavefield is linearly polarized and is laterally sheared in the Fourier domain of a 4f setup using the SLM. The zeroth order overlaps with the first-order diffracted wavefield from the SLM and after passing through a linear polarizer, the overlapping wavefields interfere on the camera plane. The setup was tested using both, coherent illumination (532nm Nd: YAG laser) [19] and partially coherent light (fiber-coupled LED with central wavelength 625nm) [20,21]. The second approach to shear interferometry is to create a copy of the object wavefield and modulate both object wavefields simultaneously. This approach was used by Choi et. al. [22] in a radial shearing configuration using a geometric phase (GP) lens. In radial shearing interferometry, the object wavefield and its copy are modulated by magnifying them to different sizes. The difference in magnification amount and the overlap between the modulated object wavefields cause the wavefields to interfere. In the setup presented by Choi et. al. [22], the object is illuminated by an incoherent broadband source, and the light scattered from the object is collected using an objective lens. A geometric phase lens is a polarization-directed flat lens that has a fixed focal length and acts either as a positive or negative lens depending on the polarization state of the input light. In the experiment, the input object wavefield is linearly polarized and passed through the GP lens. A linearly polarized light is a combination of left and right circular polarized light. The GP lens converts the right circular polarized light to the left circular polarized and converges with a positive focal length. Simultaneously, the GP lens converts the left circular polarized to right circular polarized light and diverges with a negative focal length. This enables radial shearing in the setup. The two object wavefields are then brought to the same state of linear polarization with a linear polarizer before overlapping on the camera plane to produce the interference patterns. A relay lens is used after the GP lens to flatten the wavefronts to enhance the fringe visibility while recording the intensity maps. Since the phase shift is based on manipulating the polarization states of the overlapping beams, phase shifting is introduced by rotating one of the linear polarizers.

This dissertation uses the second approach of implementing shear interferometry where both, the object wavefield and its copy are modulated but in a lateral shearing configuration. This is implemented using GP gratings. Similar to a GP lens, a GP grating uses a linearly polarized light as input and then splits the wavefield into left and right circular polarization states in the positive and negative diffraction angles depending on the polarization states. The difference between the GP lens and GP grating is shown in figure 1.2. More details on the functioning of GP gratings can be found in [23]. The functioning of the two GP gratings can be realized in Jones matrix by rewriting the GP grating pair as two opposite circular polarizers with a phase difference $(\Delta\phi = \phi_2 - \phi_1)$ between them as shown in Eq 1.1 [23].

$$J_{out} = \frac{j}{2}\left\{exp(j\phi_1)\begin{bmatrix}1 & j\\ -j & 1\end{bmatrix} + exp(j\phi_2)\begin{bmatrix}1 & -j\\ j & 1\end{bmatrix}\right\} \tag{1.1}$$

The results of interacting wavefields with different polarization states are shown in Appendix-A. The GP gratings used in the experiments in this dissertation are from Edmund optics (#12-677 - VIS Coated, 25mm Square, 5° Diffraction Polarization Grating).

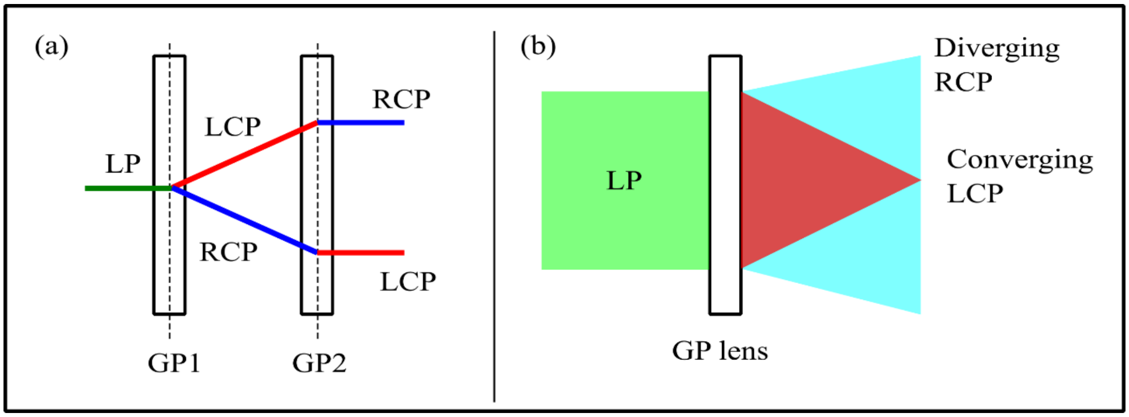

FIGURE 1.2: Functioning of GP elements demonstrating shearing. (a) GP gratings, (b) GP lens

1.3. Phase and Wavefield reconstruction algorithms

The algorithm that is used to estimate the phase or the height map is based on the mechanism used for modulating the fringe patterns during measurement. For systems that use a reference mirror and a phase shifting mechanism with constant phase shifts, Surrel [1] developed a general framework for deriving equations for implementing the N-step phase-shifting algorithm. Other unconventional phase-shifting algorithms with constant phase shifts that do not fit in this framework have also been explored in the literature [24,25]. For cases where the phase shifts are not equal, random, and unknown, Wang et. al. [2] and Albertazzi et. al. [3,26] have studied and developed algorithms that can detect the phase shift between the recorded frames and estimate phase maps from the recorded interference patterns.

For interferometric systems that do not use a reference mirror, such as in shear interferometry, direct use of phase shifting algorithms might not always be the solution to extract phase information of the object surface. One exception to this statement was shown by the radial shearing interferometer developed by Choi et. al. [22]. The use of the GP lens in Choi et. al. [22] expands one of the sheared wavefronts to a large extent that it could be approximated as a flat reference and so the use of a 4-step phase shifting algorithm was able to extract the phase. But, in the case of lateral shear interferometry, the use of a phase-shifting algorithm estimates the gradient of the phase map with respect to the lateral shear used while recording the interferograms. So alternative approaches to extracting the phase information is needed.

Earlier approaches to solving interferograms from shear interferometry can be classified into zonal reconstruction and model reconstruction. Rimmer [27] presented a zonal reconstruction approach by considering phase reconstruction as a least squares problem. The method uses two orthogonal shears to create a series of linear equations that can be assembled in a matrix format and turned into a least-squares problem to estimate the phase. A preliminary analysis was also done by the author to understand the propagation of errors in estimating the phase. A similar study was also conducted by Fried [28] where the algorithm was developed as a generalized wavefront reconstruction technique based on the phase difference between two measurements with a least-squares approach. A more detailed analysis in the evaluation of noise and error was also done in this study. With advancements in computational power, more approaches on zonal reconstruction are still being explored. Dai et. al. [29] designed and implemented an algorithm that can be used for any aperture shape to produce high spatial resolution reconstruction and can be used to work in tandem with Gerchberg-type algorithms [30,31] using two orthogonal shears.

In Model reconstruction methods, a set of model functions are used, and the coefficients of difference model functions are estimated to best fit the acquired interferograms. Some prior knowledge about the shape of the object surface is needed to identify the best model suitable for the wavefront reconstruction. Harbers et. al. [32] presented a model reconstruction method by using Zernike polynomials to estimate the object wavefront.

With the advancements in computational power these days, optimization algorithms are often adopted to solve the shear interferometry problem to estimate the object wavefield. In the shear interferometry systems presented by Falldorf et. al. in [19–21], the object wavefield is left undisturbed while the copy of the object wavefield is sheared using an SLM. The authors defined a loss function based on the cross-amplitude and the estimate of the object wavefield. The cross-amplitude term was evaluated by applying phase shifting algorithm to the recorded interferograms. Using the loss function and its gradient, the authors used a gradient descent iterative approach to estimate the object wavefield.

Our initial approach to solving and estimating the object wavefield was inspired by the gradient approach method used by Falldorf et. al. [19–21]. In the works done by Falldorf et. al. [19], for an object wavefield of $u(\vec{x})$ and shear $\overrightarrow{s_n}$, the complex cross-amplitude $M_n(\vec{x})$ (Eq. 1.2), loss function L (Eq. 1.3) and the gradient of the loss function ∇L (Eq. 1.4) are defined as follows.

$$M_n(\vec{x}) = u^*(\vec{x}) \cdot u(\vec{x} + \overrightarrow{s_n}) \tag{1.2}$$

$$L = \sum_n \| M_n(\vec{x}) - f^*(\vec{x}) f(\vec{x} + \overrightarrow{s_n}) \|^2 = \sum_n \| \psi_n(\vec{x}) \|^2 \tag{1.3}$$

$$\nabla L^{(m)}(\vec{x}) = -2 \sum_n \left[f^{(m)}(\vec{x} + \overrightarrow{s_n}) \cdot \psi_n^{(m)*}(\vec{x}) + f^{(m)}(\vec{x} - \overrightarrow{s_n}) \cdot \psi_n^{(m)*}(\vec{x} - \overrightarrow{s_n}) \right] \tag{1.4}$$

The shearing interferometry setup used in this dissertation uses a pair of GP gratings to implement the shear. So, both, the object wavefield and its copy are sheared laterally and symmetrically about the optical axis. Derivations similar to Eq. 1.2-1.4 were done for this case of lateral shearing and are shown below in Eq. 1.5-1.7.

$$M_n(\vec{x}) = u^*(\vec{x} - \overrightarrow{s_n}) \cdot u(\vec{x} + \overrightarrow{s_n}) \tag{1.5}$$

$$L = \sum_n \| M_n(\vec{x}) - f^*(\vec{x}) f(\vec{x} + \overrightarrow{s_n}) \|^2 = \sum_n \| \psi_n(\vec{x}) \|^2 \tag{1.6}$$

$$\nabla L^{(m)}(\vec{x}) = -2 \sum_n \left[f^{(m)}(\vec{x} + \overrightarrow{s_n}) \cdot \psi_n^{(m)*}(\vec{x} + \overrightarrow{s_n}) + f^{(m)}(\vec{x} - \overrightarrow{s_n}) \cdot \psi_n^{(m)*}(\vec{x} - \overrightarrow{s_n}) \right] \tag{1.7}$$

The presence of the $\psi_n(\vec{x} + \overrightarrow{s_n})$ and $\psi_n(\vec{x} - \overrightarrow{s_n})$ complicates the optical setup which is not feasible to implement using GP gratings without introducing significant errors during the measurement process. So, for the optical setup that is discussed in this dissertation, an optimization approach that does not depend on the gradient of the loss function is required. One such algorithm was developed by Konijnenberg et. al. [33] for a lens-less imaging system in the X-ray and Extreme Ultraviolet (EUV) community. This is an alternating projections algorithm that is based on work done by Youla [34] for image restoration. The algorithm developed by Konijnenberg et. al. [33] has been analyzed and modified for the optical community in this dissertation to work for lateral shearing in the spatial domain. Further, the algorithm has also been modified with acceleration techniques based on multiresolution strategies [35] to improve the convergence rate and achieve faster wavefield reconstruction. Further, the multiresolution technique also renders the reconstruction algorithm impervious to the choice of initial guess. The modified alternating projections algorithm developed in this dissertation was also analyzed to detect the presence of any artifacts that result from the algorithm and further modifications were done to mitigate these effects. The details of the modification are available in Chapter 2 of this dissertation.

1.4. Dissertation Objectives

The objectives of the dissertation are as follows:

- Design and build a lateral shear interferometry system that can also function as a holography system
- Develop a working algorithm that can work with the optical setup to reconstruct wavefield

- Characterize the effects of shear on the reconstructed wavefield
- Identify strategies to optimize the shear selection
- Explore applications to expand the use of GP gratings for measuring diffused surfaces

1.5. Dissertation Structure and Outcomes

The research work presented in this dissertation follows the Three-Article Dissertation Guidelines of UNC Charlotte. Chapter 2 presents the first article titled “Variable Shearing Holography with Applications to phase imaging and Metrology”, published in Light: Advanced Manufacturing in 2022. Chapter 2 discusses and compares two designs for using GP gratings for lateral shear interferometry systems. A modified version of an alternating projection algorithm is developed and tested with these setups. The effect of selected shears on reconstructed wavefields is studied through transfer functions defined as spatial information density function (SIDF) and frequency information density function (FIDF). Chapter 3 presents a conference proceeding titled “Variable Shearing Holography with geometric phase elements” published and presented in SPIE Optical Engineering + Applications in 2022 in San Diego, California, United States. Chapter 3 discusses the limitations of shears from the perspective of the spatial information density function. Chapter 4 presents the second article titled “Effective selection of shears in variable lateral shearing holography”. This chapter presents a statistical analysis based on simulations using synthetic intensity maps to study the effect of shears on the reconstruction of wavefields. A synthetically generated defocused point source was used in this study since it comprises a wide range of frequencies in the selected field of view. The work provides an effective set of shear parameters to reconstruct wavefields with minimal errors. The result of this study is also compared with corresponding frequency information density maps to correlate the results. This article has been submitted to Applied Optics and is awaiting a reviewer/editorial response. Chapter 5 presents the third article titled “Fringe projection using geometric phase elements” which has been submitted to Applied Optics and is awaiting reviewer/editorial response. Chapters 2 and 3 present the use of GP grating pairs as a shear interferometry system for reflective and transmissive surfaces. Chapter 4 presents the best shears to operate the shear interferometry setup that is presented in Chapters 2 and 3. Chapter 5 presents a secondary application to the GP grating pair setup to operate as a fringe projection system that is suitable for diffused surfaces. Chapter 6 concludes the dissertation by summarizing the highlights and major outcomes of the project.

1.6 Real-world Applications from the Dissertation

Reference-less systems with single-path designs enable systems that are robust to environmental noise, extending their applications in harsh environments outside laboratories. An example of such design is demonstrated by Viotti and Albertazzi in [36] where the authors demonstrate the use of a portable speckle interferometry setup to evaluate stresses and detect defects on gas pipelines. Additionally, the use of flat optics has been attracting a lot of researchers to implement extremely compact systems using common path designs. Choi et. al. [22] demonstrated the use of geometric polarization gratings to implement an incoherent holographic shear interferometric system based on radial shearing. The studies conducted in this dissertation show a design for using geometric polarization gratings to implement a holographic interferometric system based on lateral shearing. An example of compact design based on the systems discussed in this dissertation is shown in Figure 1.3. These systems can also be integrated into existing designs such as the radial shearing system by Choi et. al. [22] to create hybrid systems for measuring different types of surfaces.

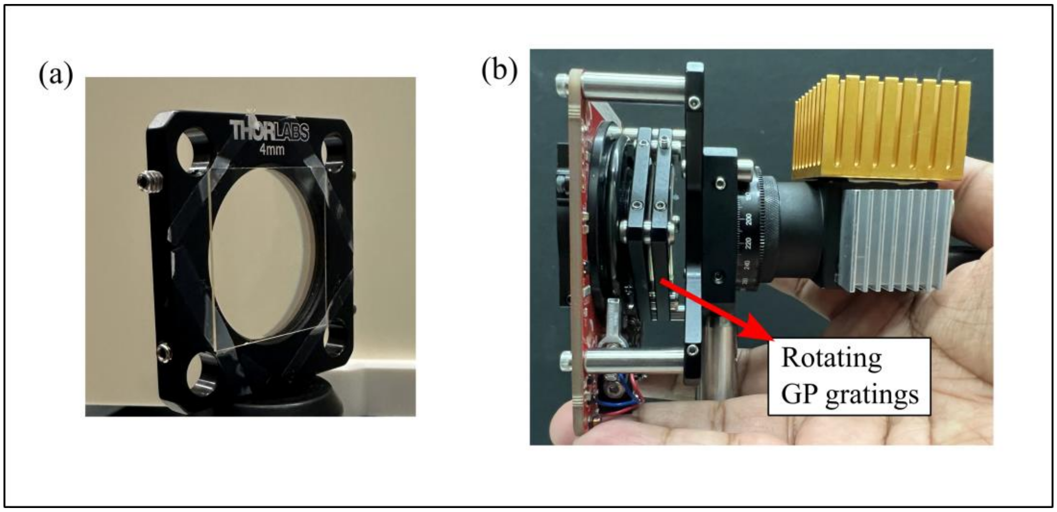

FIGURE 1.3: (a) GP grating, (b) Compact holographic shear interferometric system using geometric phase gratings

The dissertation also presents the equations necessary for developing a wavefield reconstruction algorithm using this setup. The reconstruction algorithm developed in this dissertation is not limited to setups using GP gratings but can be used for any lateral shearing interferometric setup that shears symmetrically about the optical axis. Further, this dissertation also presents guidelines for effective shear selection strategies that can be extended to work with any shear interferometric systems that use symmetrical lateral shearing. The dissertation also presents the idea that the use of GP grating pairs is not limited to interferometric systems but can also be used to make fringe projection systems. This shows the potential applications of the designs discussed in this dissertation to be used in different fields ranging from bio-samples using holographic systems to additively manufactured surfaces using fringe projection systems.

REFERENCES

1. Y. Surrel, "Design of algorithms for phase measurements by the use of phase stepping," Appl. Opt. **35**, 51 (1996).

2. Z. Wang and B. Han, "Advanced iterative algorithm for phase extraction of randomly phase-shifted interferograms," Opt. Lett. **29**, 1671 (2004).

3. A. Albertazzi, A. V. Fantin, D. P. Willemann, and M. E. Benedet, "Phase Maps Retrieval from Sequences of Phase Shifted Images with Unknown Phase Steps Using Generalized N-Dimensional Lissajous Figures—Principles and Applications," Int. J. Optomechatronics **8**, 340–356 (2014).

4. D. Malacara, ed., *Optical Shop Testing* (John Wiley & Sons, Inc., 2007).

5. S. Pancharatnam, "Generalized theory of interference, and its applications," Proc. Indian Acad. Sci. - Sect. A **44**, 247–262 (1956).

6. M. P. Kothiyal and C. Delisle, "Shearing interferometer for phase shifting interferometry with polarization phase shifter," Appl. Opt. **24**, 4439 (1985).

7. S. Sarkar, N. Ghosh, S. Chakraborty, and K. Bhattacharya, "Self-referenced rectangular path cyclic interferometer with polarization phase shifting," Appl. Opt. **51**, 126 (2012).

8. P. J. de Groot, L. L. Deck, R. Su, and W. Osten, "Contributions of holography to the advancement of interferometric measurements of surface topography," Light Adv. Manuf. **3**, 1 (2022).

9. T.-C. Poon, ed., *Digital Holography and Three-Dimensional Display* (Springer US, 2006), Vol. 148.

10. J. Rosen, A. Vijayakumar, M. Kumar, M. R. Rai, R. Kelner, Y. Kashter, A. Bulbul, and S. Mukherjee, "Recent advances in self-interference incoherent digital holography," Adv. Opt. Photonics **11**, 1 (2019).

11. T. Kozacki, K. Falaggis, and M. Kujawinska, "Computation of diffracted fields for the case of high numerical aperture using the angular spectrum method," Appl. Opt. **51**, 7080–7088 (2012).

12. K. Falaggis, T. Kozacki, and M. Kujawinska, "Computation of highly off-axis diffracted fields using the band-limited angular spectrum method with suppressed Gibbs related artifacts," Appl. Opt. **52**, 3288–3297 (2013).

13. P. Pavliček and O. Hýbl, "White-light interferometry on rough surfaces—measurement uncertainty caused by noise," Appl. Opt. **51**, 465 (2012).

14. P. Pavliček and O. Hýbl, "White-light interferometry on rough surfaces--measurement uncertainty caused by surface roughness," Appl. Opt. **47**, 2941–2949 (2008).

15. C. O Mahony, M. Hill, M. Brunet, R. Duane, and A. Mathewson, "Characterization of micromechanical structures using white-light interferometry," Meas. Sci. Technol. **14**, 1807–1814 (2003).

16. C. Hovis, H. Shahinian, and C. Evans, "Observations on the effect of retrace error in scanning white light interferometry of smooth optical surfaces," in *Optical Design and Fabrication 2019 (Freeform, OFT)* (OSA, 2019), Vol. Part F161-, p. OM4A.2.

17. O. Bryngdahl and W.-H. Lee, "Shearing interferometry in polar coordinates," J. Opt. Soc. Am. **64**, 1606 (1974).

18. R. Porras-Aguilar, K. Falaggis, J. C. Ramirez-San-Juan, and R. Ramos-Garcia, "Self-calibrating common-path interferometry," Opt. Express **23**, 3327 (2015).

19. C. Falldorf, C. von Kopylow, and R. B. Bergmann, "Wave field sensing by means of computational shear interferometry," J. Opt. Soc. Am. A **30**, 1905 (2013).

20. C. Falldorf, M. Agour, and R. B. Bergmann, "Advanced wave field sensing using computational shear interferometry," Interferom. XVII Adv. Appl. **9204**, 92040C (2014).

21. C. Falldorf, M. Agour, and R. B. Bergmann, "Digital holography and quantitative phase contrast imaging using computational shear interferometry," Opt. Eng. **54**, 024110 (2015).

22. K. Choi, J. Yim, and S.-W. Min, "Achromatic phase shifting self-interference incoherent digital holography using linear polarizer and geometric phase lens," Opt. Express **26**, 16212 (2018).

23. P. Blain, P. Piron, Y. Renotte, and S. Habraken, "An in-line shearography setup based on circular polarization gratings," Opt. Lasers Eng. **51**, 1053–1059 (2013).

24. C. Quan, C. J. Tay, X. Kang, X. Y. He, and H. M. Shang, "Shape measurement by use of liquid-crystal display fringe projection with two-step phase shifting," Appl. Opt. **42**, 2329 (2003).

25. L. I. Muravsky, O. P. Ostash, A. B. Kmet', T. I. Voronyak, and I. M. Andreiko, "Two-frame phase-shifting interferometry for retrieval of smooth surface and its displacements," Opt. Lasers Eng. **49**, 305–312 (2011).

26. A. Albertazzi Jr., A. Fantin, M. Benedet, D. Willemann, and A. Maia, "Performance evaluation of a phase retrieval algorithm from sequences of interferograms with unknown phase shifts using generalized N-dimensional Lissajous figures," 92030O (2014).

27. M. P. Rimmer, "Method for Evaluating Lateral Shearing Interferograms," Appl. Opt. **13**,

623 (1974).

28. D. L. Fried, "Least-square fitting a wave-front distortion estimate to an array of phase-difference measurements," J. Opt. Soc. Am. **67**, 370 (1977).

29. F. Dai, F. Tang, X. Wang, and O. Sasaki, "Generalized zonal wavefront reconstruction for high spatial resolution in lateral shearing interferometry," J. Opt. Soc. Am. A **29**, 2038 (2012).

30. R. W. Gerchberg and W. O. Saxton, "A Practical Algorithm for the Determination of Phase from Image and Diffraction Plane Pictures," Optik (Stuttg). **35**, 237–246 (1972).

31. W. Zou and J. P. Rolland, "Iterative zonal wave-front estimation algorithm for optical testing with general-shaped pupils," J. Opt. Soc. Am. A **22**, 938 (2005).

32. G. Harbers, P. J. Kunst, and G. W. R. Leibbrandt, "Analysis of lateral shearing interferograms by use of Zernike polynomials," Appl. Opt. **35**, 6162 (1996).

33. A. P. Konijnenberg, A. C. C. de Beurs, G. S. M. Jansen, H. P. Urbach, S. Witte, and W. M. J. Coene, "Phase retrieval algorithms for lensless imaging using diffractive shearing interferometry," J. Opt. Soc. Am. A **37**, 914 (2020).

34. D. Youla, "Generalized Image Restoration by the Method of Alternating Orthogonal Projections," IEEE Trans. Circuits Syst. **25**, 694–702 (1978).

35. K. Falaggis, T. Kozacki, and M. Kujawinska, "Accelerated single-beam wavefront reconstruction techniques based on relaxation and multiresolution strategies," Opt. Lett. **38**, 1660 (2013).

36. M. R. Viotti and A. Albertazzi G., Jr., "Industrial inspections by speckle interferometry: general requirements and a case study," in *Optical Measurement Systems for Industrial Inspection VI*, P. H. Lehmann, ed. (2009), Vol. 7389, p. 73890G.

CHAPTER 2: (PAPER 1) VARIABLE SHEARING HOLOGRAPHY WITH APPLICATIONS TO PHASE IMAGING AND METROLOGY

Citation

Prithiviraj Shanmugam, Alyson Light, Avery Turley, Konstantinos Falaggis. Variable shearing holography with applications to phase imaging and metrology[J]. Light: Advanced Manufacturing 3, 3(2022). doi: 10.37188/lam.2022.016

Copyright Permissions

2.1 Introduction

Single-beam wavefront reconstruction techniques are exciting alternatives to interferometry. These techniques are inherently robust to vibrations and often can be designed in a compact optical setup. Recent research expands those techniques to partial coherent sources, where LEDs are employed in place of lasers. Another interesting field is the area of bio-imaging, where existing microscopes are converted into phase measuring devices using a single-beam phase wavefront reconstruction add-on. A further appealing aspect is that many single-beam systems can be designed to work with no beamsplitter, allowing the sensor to be closer to the sample and enabling simpler optical measurements with higher-numerical aperture. In phase retrieval, there are two representative families of wavefront reconstruction techniques. Firstly, techniques based on deterministic models [1–5], and secondly, techniques that employ an iterative solver that utilizes wave-propagation techniques [6,7] or Fourier relationships [8,9]. With the advent of faster computer systems, new cameras are often developed with a higher pixel count, diminishing many advances of the higher computational power. Optical measurement technologies need to adapt to survive this trend through more innovative algorithms, new measurement concepts, or both.

For instance, in the field of phase retrieval, the convergence may be improved using multi-resolution and relaxation techniques [10]. Another possibility is to alter the illumination [11] or combine deterministic and iterative algorithms [12].

However, the elephant in the room of all methods mentioned above is the inverse problem resulting from the data produced by the unmodulated optical beam. In other words, often, the data is too similar, and significant efforts need to be made to reduce the similarity (e.g., repeating the measurement at a large defocus distance [3]).

Recent advances in computational shear interferometry [13,14] allow actively modulating an incident beam as it interferes with itself. Modulation of the beam increases instantly the diversity in the data. In particular, when employed with phase-shifting techniques [15], it is possible to obtain the complex cross-term of two interfering wavefields directly. Despite this sophistication, the system by Falldorf requires a spatial light modular (SLM), which significantly contributes to the system costs. The wavefront reconstruction technique reported by Falldorf et al. [13] is based on a gradient descent approach for non-symmetric shearing systems. However, compared to the non-symmetric case, deriving the grading of a that non-holomorphic function for the case of a “symmetric” shearing system is not straightforward. Hence other approaches like the alternating projections by Konijnenberg [16] are preferred reconstruction algorithms.

Recent advances in geometric phase (GP) elements lead to the development of GP gratings and GP lenses that can be employed in lateral and radial shearing interferometry [17–19], with polarization phase-shifting capabilities [20,21]. The remaining quest is to recover the correct wavefront from the captured phase-shifted interferograms.

This paper proposes a variable shearing interferometer that consists of a series of GP gratings and polarization optics. This setup enables measuring a series of phase-shifted interferograms for a given shear amount, as shown in Figure 2.1. In a subsequent step, we reconstruct the wavefield using a modified version of the alternating projections algorithm, developed by Konijnenberg [16], and a series of interferograms with different amounts of shear. The discussed systems are the first experimentally demonstrated GP grating-based variable shear interferometers for complex wavefield reconstructions. We discuss various possible configurations of these instruments and demonstrate the success of two distinct shear selection strategies (employing one or two grating pairs). We analyze these findings using the “frequency information density” and the “spatial information density” analyses based on transfer function and support function concepts introduced by Servin in [22]. We further show a GP grating configuration with a fixed shear amount, but an adjustable rotational shear axis (one mechanical rotational axis) is sufficient to obtain robust measurements while maintaining phase-shifting capabilities using a pixelated polarization camera. We also investigate the effect of other error sources (e.g., imperfect shear estimation), which affects the resolution of the reconstructed wavefront. This effect is not commonly known (for coherent systems, the resolution is often a result of numerical aperture, pixel size, or spatial coherence of the source). To mitigate this source of error, we report a shear detection technique using the peaks of the second derivative of the autocorrelation function of the holograms. Measuring the shear amount directly from the hologram is different from relying on a well-calibrated system and increases the system's accuracy.

2.2. Results

2.2.1. Shear Selection

Polarization gratings, also known as geometric phase (GP) gratings, are liquid crystal polymer-based optical gratings with a diffraction angle that depends on the polarization and wavelength of light. GP gratings are designed to diffract right-handed circularly polarized light (RHCP) and left-handed circularly polarized light (LHCP) at a negative angle and positive diffraction angle, respectively. The value of this angle depends on the prescription; commercially available gratings with various groove densities result in diffraction angles of the first-order between 3 and 10 degrees. The diffraction angle can be related directly to the wavelength and groove density using the well-known equation $m\,\lambda = d\,sin(\theta)$.

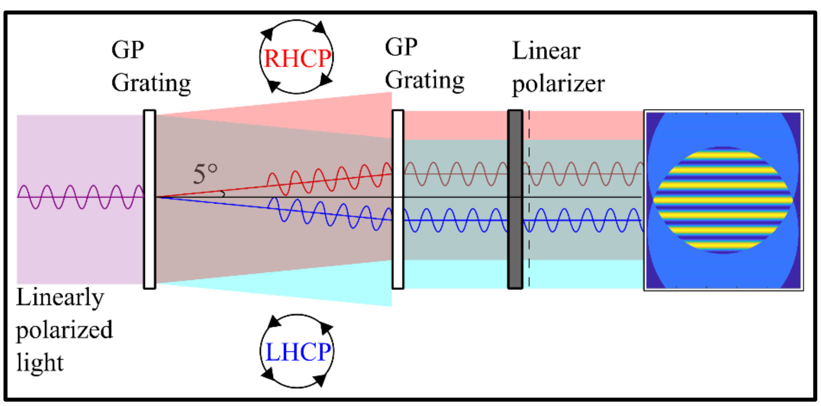

FIGURE 2.1: Principle of GP grating based shearing interferometry for the case of linearly polarized light

A lateral shear in the spatial domain is achieved when two GP gratings are placed consecutively [17], as shown in Figure 2.1. In that configuration, both identical GP gratings are aligned along the same axis and orientation. In this way, the first GP grating deflects the incoming beams at the angles +/- α, and the second GP grating compensates this deflection by diffracting the beam into -/+ α. The properties of these GP gratings in this configuration are outlined in [17]. Adjusting the distance between the first and the second GP grating allows adjusting the shear amount of the two interfering waves, as shown in Figure 2.2, enabling unique properties that can be used for adjustable shearing interferometry.

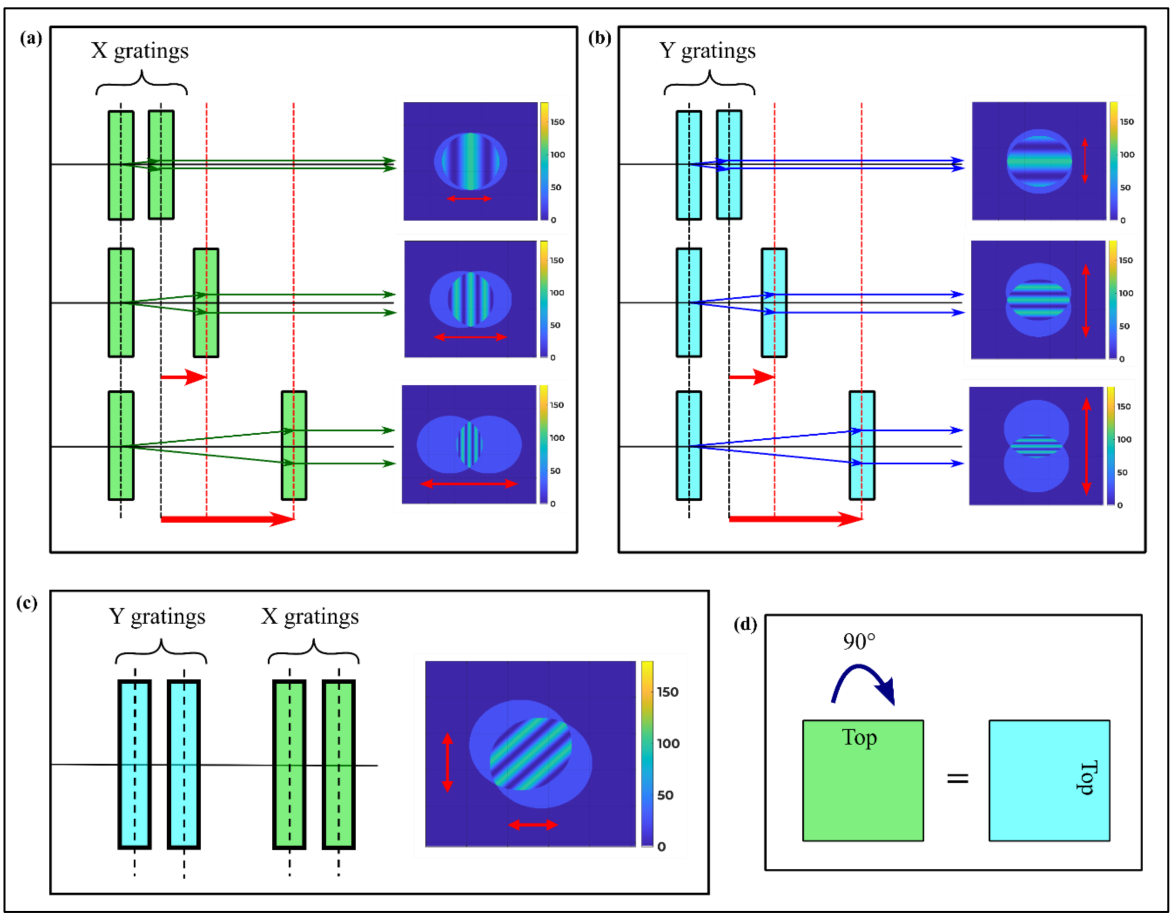

FIGURE 2.2: Examples of interferograms for the case of a spherical wave at the distance z = 350 mm with different shear amounts in x- and y- direction.

As shown in Figure 2.2, shearing along the y-axis is possible by flipping the gratings by 90 degrees. An instrument employing a series of four GP gratings enables shearing in both x- and y-direction. This configuration shears along the x- and y-axis independently. This system uses 4 gratings in total: one pair for x-shear and the other pair for y-shear.

A different possible configuration is to maintain a fixed shear between two beams and modulate the fringes by rotating the shear axis about the optical axis, as shown in Figure 2.3. This configuration requires only one GP gratings pair and is more compact than the other configuration of Figure 2.2c.

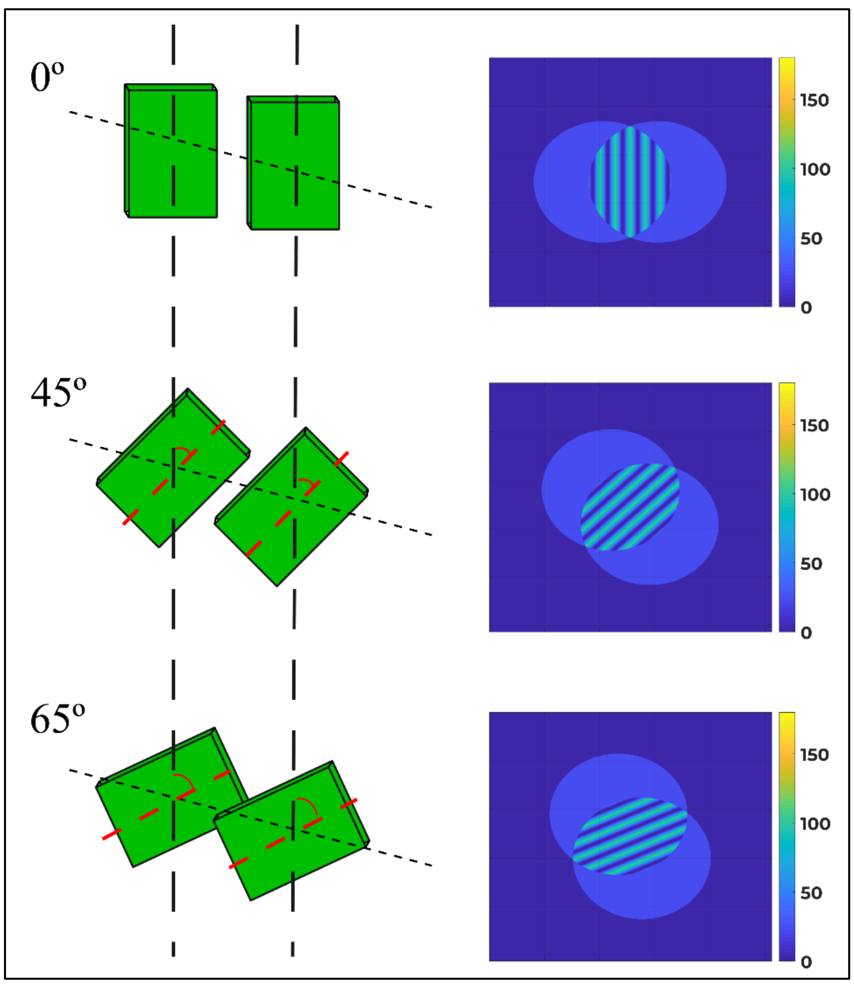

FIGURE 2.3: Examples of interferograms for the case of a spherical wave at the distance z = 250 mm with constant shear and different grating rotational angles

Furthermore, as the linearly polarized light at the instrument's input is converted into left and right circular polarized components, there is a need to employ a linear polarizer to make these two waves interfere. Notably, this configuration provides geometric phase-shifting capability [23], i.e., by rotating the axis of the polarizer, it is possible to create a series of phase-shifted interferograms, as shown in Figure 2.4. The relation between the polarization angle of the linear polarizer and the phase shift angle is demonstrated using Jones calculus in Appendix-B. In the following sections, we propose using GP gratings for multi-shear variable shearing interferometry with phase-shifting capability. We further evaluate the performance of the instrument with above-mentioned configurations using multi-shear wavefront reconstruction techniques.

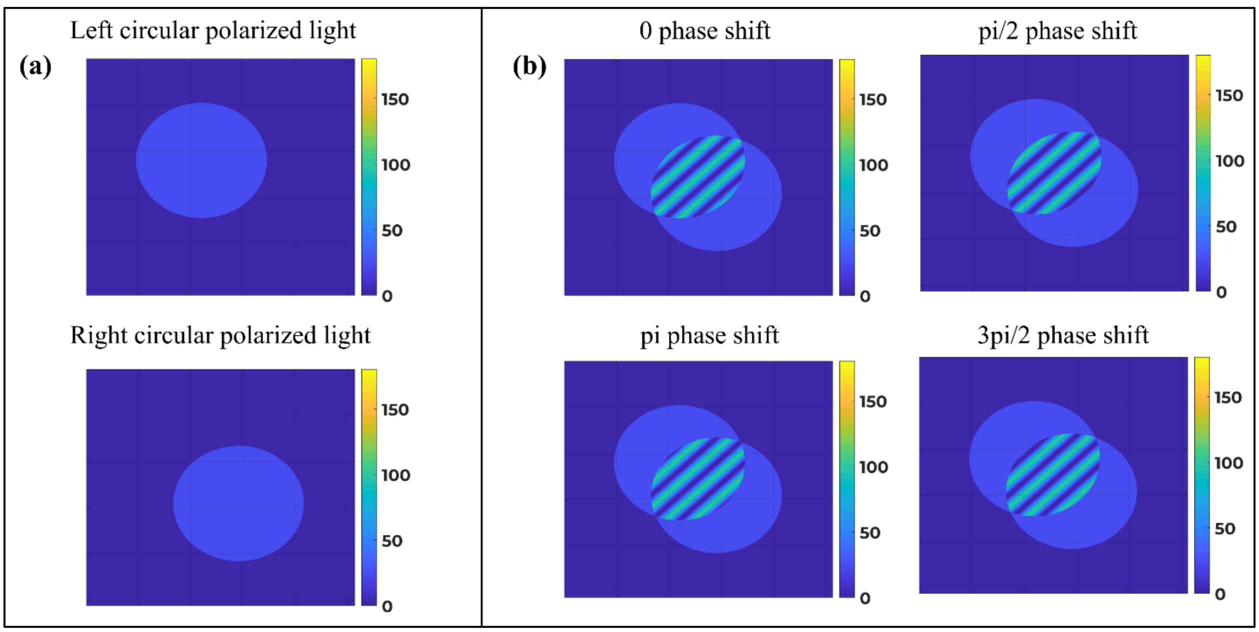

FIGURE 2.4: (a) Intensity distribution of a spherical wavefront with constant amplitude before reaching the linear polarizer, (b) Intensity after the linear polarizer for four different angles of the polarizer axis to produce a phase shift between the interfering waves of 0, π/2, π, and 3π/2

2.2.2. Wavefront reconstruction algorithm for multi-shear variable shear interferometry

The previous section showed how GP gratings could obtain a series of phase-shifted interferograms for various shear amounts. These interferograms allow calculating the complex cross-terms of the two-interfering waves at each shear. The challenge is to reconstruct the complex wavefield from this data. In this section, we present an iterative algorithm based on the approach of Konijnenberg [16] that was inspired by the alternating projection algorithms [9,24]. Consider a general wavefield u with the amplitude A and the phase ϕ as

$$u = A \cdot exp(i\phi) \tag{2.1}$$

which produces the following interferogram $I_{n,\delta}(\vec{x})$ in shearing, as

$$I_{n,\delta}(\vec{x}) = \left|u\left(\vec{x} + \overrightarrow{ds_n}\right)\right|^2 + \left|u\left(\vec{x} - \overrightarrow{ds_n}\right)\right|^2 + 2\Re\{C_n(\vec{x})\, exp(-i\delta)\} \tag{2.2}$$

Where $\overrightarrow{ds} = \left[ds_x\,, ds_y\right]$ and, ds_x and ds_y is the shear in x- and y- direction, δ is the phase shift induced by the rotating polarizer, and $C_n(\vec{x})$ is the complex cross-term

$$C_n(\vec{x}) = u^*\left(\vec{x} - \overrightarrow{ds_n}\right) \cdot u\left(\vec{x} + \overrightarrow{ds_n}\right) \tag{2.3}$$

The term $C_n(\vec{x})$ is estimated using phase-shifting techniques, which for the four-bucket algorithm results in

$$C_n(\vec{x}) = \left(I_{n,0}(\vec{x}) - I_{n,\pi}(\vec{x})\right) + i\left(I_{n,\frac{\pi}{2}}(\vec{x}) - I_{n,\frac{3\pi}{2}}(\vec{x})\right) \tag{2.4}$$

The reconstruction algorithm uses the term $C_n(\vec{x})$ that is obtained at different shears '$\overrightarrow{s_n}$' to reconstruct the object wavefield through an iterative process. In this work, we employ a modified version of alternating projections (AP) approach developed by Konijnenberg [16] for the x-ray community. The algorithm applies two distinct constraint sets, where each constraint allows only a limited family of solutions. The objective of the wavefield reconstruction algorithm is to identify the unique solution that satisfies all constraints (and for all shears). These constraints are satisfied by employing alternating projections between the two solution domains, in which we apply both so-called "object constraints" and so-called "measurement constraints."

Switching between "object constraints" and "measurement constraints" is applied continuously until the algorithm converges to a specific wavefield. The convergence can be conveniently estimated using the following loss function

$$L = \sum_{n=1}^{S} \left(\left| f^{M}{}_{n,+}(\vec{x}) - f^{O}{}_{n,+}(\vec{x}) \right|^2 + \left| f^{M}{}_{n,-}(\vec{x}) - f^{O}{}_{n,-}(\vec{x}) \right|^2 \right) \tag{2.5}$$

where subscript n denotes that the wavefield uses the shear $\overrightarrow{ds_n}$, S is the total number of shears, and for convenience, we define the estimated wavefield after N iterations as $f(\vec{x})$ to distinguish it from ideal real wavefield $u(\vec{x})$. The notation $f(\vec{x})$ is used as a general indication to represent estimated wavefields from both constraints, where the notation $f^{M}(\vec{x})$ denotes the estimate of the wavefield directly after the measurement constraint is applied, and $f^{O}(\vec{x})$denotes the estimate of the wavefield directly after the object constraint is applied. For further simplification, the symbols 'n,+' and 'n,-' in the subscript are used to represent positive and negative shears, i.e., $f_{n,\pm}(\vec{x}) = f\left(\vec{x} \pm \overrightarrow{ds_n}\right)$. Consequently, the estimated complex cross amplitude term can be presented as

$$\begin{aligned} C_{est,n}(\vec{x}) &= f^{*}\left(\vec{x} - \overrightarrow{ds_n}\right) \cdot f(\vec{x} + \overrightarrow{ds_n}) \\ &= f_{n,-}(\vec{x})^{*} \cdot f_{n,+}(\vec{x}) \end{aligned} \tag{2.6}$$

and can be generated using the estimated wavefield $f^{M}{}_{n}(\vec{x})$ at any shear $\overrightarrow{S_n}$.

Notably, in the presence of noise, there is no exact solution. However, the wavefield reconstruction algorithm estimates the best fit solution that matches the experiment data. The loss function serves as a metric to be observed for convergence with an increasing number of iterations.

Figure 2.5 shows the steps of the wavefield reconstruction algorithm. After an initial guess, the algorithm continuously applies the so-called object and measurement constraints alternatingly until the loss function reaches the desired level. The application of those constraints is discussed in more detail below.

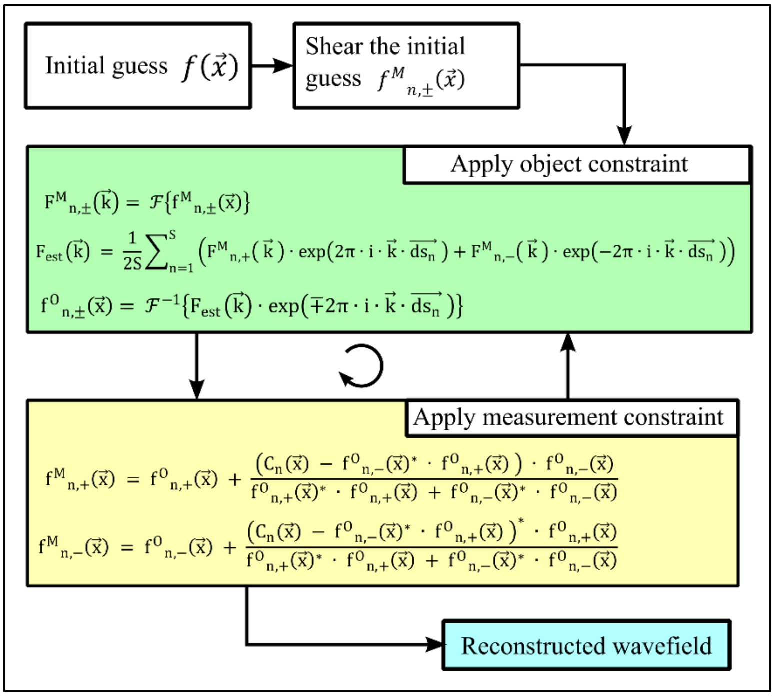

FIGURE 2.5: Principle of multi-shear wavefront reconstruction algorithm

2.2.3. Estimation of $f^M{}_{n,\pm}(\vec{x})$ using the initial guess

This step of the algorithm uses only the initial guess $f(\vec{x})$ in the first iteration to estimate $f^M{}_{n,\pm}(\vec{x})$. An initial guess is assumed for $f(\vec{x})$ (e.g., a spherical wave, a plane wave, or a random wavefield) and is laterally sheared by the same shears used in the experiment. For a wavefield $f(\vec{x})$, the shearing is done in the Fourier domain using the following equations.

$$F(\vec{k}) = \mathcal{F}\{f(\vec{x})\} \tag{2.7}$$

$$f^M{}_{n,\pm}(\vec{x}) = \mathcal{F}^{-1}\{F(\vec{k}).exp(\mp 2\pi\cdot i\cdot\vec{k}\cdot\overrightarrow{ds_n})\} \tag{2.8}$$

Assuming that the initial guess wavefield is from the measurement constraint domain, the initial guess and its sheared components are indicated as ${f^M}_{n,\pm}(\vec{x})$. A wavefield with constant phase and unit amplitude is used as an initial guess for the reconstructions done in this paper.

2.2.4. Application of the Object constraint

The object constraints are applied by transforming the sheared components of the estimated wavefield to the Fourier domain and compensating the shear for each ${\mathrm{f}^{\mathrm{M}}}_{\mathrm{n},\pm}(\vec{\mathrm{x}})$ to obtain $\mathrm{f}(\vec{\mathrm{x}})$ using the Fourier Shift theorem. All calculated values for $\mathrm{F}(\vec{\mathrm{k}})$ are averaged to obtain a more accurate result.

$$ {F^M}_{n,\pm}(\vec{k}) = \mathcal{F}\left\{ {f^M}_{n,\pm}(\vec{x}) \right\} \tag{2.9} $$

$$ \mathrm{F_{est}}(\vec{\mathrm{k}}) = \frac{1}{2\mathrm{S}} \sum_{\mathrm{n}=1}^{\mathrm{S}} \left({\mathrm{F}^{\mathrm{M}}}_{\mathrm{n},+}(\vec{\mathrm{k}}) \cdot \exp\left(2\pi \cdot \mathrm{i} \cdot \vec{\mathrm{k}} \cdot \overrightarrow{\mathrm{ds_n}}\right) + {\mathrm{F}^{\mathrm{M}}}_{\mathrm{n},-}(\vec{\mathrm{k}}) \cdot \exp\left(-2\pi \cdot \mathrm{i} \cdot \vec{\mathrm{k}} \cdot \overrightarrow{\mathrm{ds_n}}\right) \right) \tag{2.10} $$

Finally, $F_{est}(\vec{k})$ is transformed back into the spatial domain using the inverse Fourier transform. However, because the measurement constraints (applied in the second part of the iteration) require the wavefield for different shears, we apply again the Fourier shift theorem to obtain ${f^O}_{n,\pm}(\vec{x})$ as

$$ {\mathrm{f}^{\mathrm{O}}}_{\mathrm{n},\pm}(\vec{\mathrm{x}}) = \mathcal{F}^{-1}\left\{ \mathrm{F_{est}}(\vec{\mathrm{k}}) \cdot \exp\left(\mp 2\pi \cdot \mathrm{i} \cdot \vec{\mathrm{k}} \cdot \overrightarrow{\mathrm{ds_n}}\right) \right\} \tag{2.11} $$

2.2.5. Application of the Measurement constraint

The measurement constraint equations use the estimated wavefield from the object constraint ${\mathrm{f}^{\mathrm{O}}}_{\mathrm{n},\pm}(\vec{\mathrm{x}})$ and the measured complex cross-term $\mathrm{C_n}(\vec{\mathrm{x}})$(obtained from phase shifting) to estimate the wavefield solution in the measurement constraint domain. The following equations are a modified version of the equations used by Konijnenberg in [16] to estimate the wavefield.

$$f^{M}{}_{n,+}(\vec{x}) = f^{O}{}_{n,+}(\vec{x}) + \frac{\left(C_n(\vec{x}) - f^{O}{}_{n,-}(\vec{x})^{*} \cdot f^{O}{}_{n,+}(\vec{x})\right) \cdot f^{O}{}_{n,-}(\vec{x})}{\left|f^{O}{}_{n,+}(\vec{x})\right|^2 + \left|f^{O}{}_{n,-}(\vec{x})\right|^2} \tag{2.12}$$

$$f^{M}{}_{n,-}(\vec{x}) = f^{O}{}_{n,-}(\vec{x}) + \frac{\left(C_n(\vec{x}) - f^{O}{}_{n,-}(\vec{x})^{*} \cdot f^{O}{}_{n,+}(\vec{x})\right)^{*} \cdot f^{O}{}_{n,+}(\vec{x})}{\left|f^{O}{}_{n,+}(\vec{x})\right|^2 + \left|f^{O}{}_{n,-}(\vec{x})\right|^2} \tag{2.13}$$

2.2.6. Behavior of the algorithm

The algorithm uses two sets of constraint equations, object constraint (Eq. 2.10), and measurement constraint (Eqs. 2.12 and 2.13). Each set of constraint equations has a solution set. The algorithm starts with an initial guess projected onto the object constraint solution set by using the respective equations. This produces an estimated wavefield which is a projection on the object constraint solution set. This wavefield is then projected onto the measurement constraint solution set using the respective equations, and the process repeats until convergence. Ideally, the solution we are looking for is the one that is at the intersection of these two solution sets. However, in practice, due to noise and other external factors, such intersection does not exist, and the algorithm converges when the projections oscillate between the two solution sets with solutions at the closest proximity to each other.

2.2.7. Simulation using synthetic data

The performance of the algorithm was evaluated by simulations using MATLAB. Preliminary simulations were made for a resolution of 256 x 256 pixels. For this simulation, a point source was generated with a wavelength of 600 nm at a z-distance of 87.5 mm and was sampled with a pixel size of 3.45 μm. The reconstruction algorithm uses FFTs to shear the estimated wavefields at different steps in the reconstruction. The use of FFTs, in turn, implicitly imposes a periodic boundary condition. Therefore, we use an aperture for both simulations and experiments to mitigate problems during reconstruction that might arise from periodic properties of FFTs. For this reason, a circular aperture mask with a diameter of 180 pixels was applied. Future reconstruction algorithms may exclude samples that exceed the computational window, especially at larger shear. Those samples need to be reconstructed with measurements taken at smaller shear amounts.

A series of four phase-shifted intensities were generated for each shear position. The shears generated for this simulation are shown in Figure 2.6a. Additive white Gaussian noise (AWGN) with a standard deviation of 20% of the peak intensity has been added to the generated intensities to model the effect of noise in these simulations. Afterward, to realistically model the effect of cameras, an 8-bit discretization has been applied to the intensities.

For this simulation, a total of 48 interferograms have been generated corresponding to 12 different shears with 4 phase-shifted interferograms. The ideal wavefront and reconstructed wavefront are shown in Figures 2.6b and 2.6c, respectively. The corresponding phase error of the reconstructed wavefront is shown in Figure 2.6d. Further investigation of the error map showed the presence of high-frequency artifacts, as highlighted in Figure 2.7.

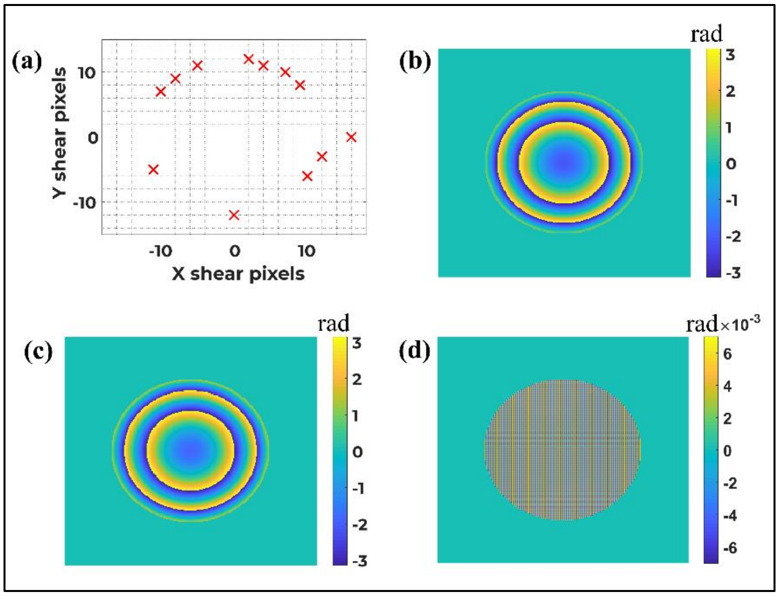

FIGURE 2.6: (Simulation) Results of reconstruction with simulation parameters: FoV 256 × 256 pixels, Pixel size 3.45 µm, Wavelength 0.6 µm, Aperture size 90 pixels, Z distance 87.5 mm. (a) Shear selection, (b) Ideal phase map, (c) Reconstructed phase map, (d) Error map between ideal and reconstructed data

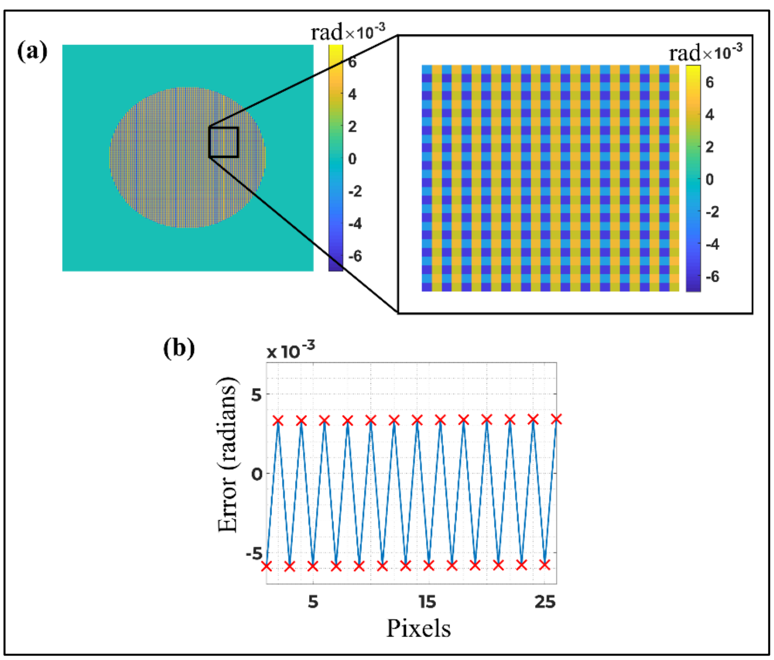

FIGURE 2.7: High frequency artifact from reconstruction algorithm.
(a) Error map zoomed, (b) Error map profile

These high-frequency artifacts occur at Nyquist frequency and appear to be a product of the reconstruction algorithm. Further analysis is required to investigate the source of these artifacts. For the reconstructions discussed in this paper, we use a low-pass Fourier filter to mitigate the formation of these artifacts.

Figure 2.8 shows error maps generated by mapping the difference between the ideal and reconstructed wavefield before and after applying the filter. A cross-section of the error profile before and after filtering is shown in Figures 2.8c and 2.8d, respectively. This simple procedure reduces the magnitude of the RMS error by one order of magnitude. Because a Fourier low-pass filter has been employed with a corner frequency of $k_c = \left(\frac{4}{5}\right) \cdot \left(\frac{1}{pixel\ size}\right)$, an artifact is produced along the boundary of the aperture. However, other filtering techniques may be applicable depending on the application, and even Zernike polynomials may be fitted to the data. The use of different filtering techniques is beyond the scope of this work.

2.2.8. Evolution of loss function

As mentioned earlier, the evolution of the loss function indicates how close the algorithm is to achieving the best solution or achieving convergence. The loss function is evaluated in these experiments by calculating the change between the solutions generated by the two constraints on positive and negative sheared estimated wavefields. The loss function was already defined in Eq. 2.5 and is reiterated here in Eq. 2.14 for convenience. Figure 2.9a shows the evolution of loss function during reconstructions done in Figure 2.8 before the filter was applied.

$$\mathrm{L} = \sum_{n=1}^{S} \left(\left| \mathrm{f^M}_{n,+}(\vec{x}) - \mathrm{f^O}_{n,+}(\vec{x}) \right|^2 + \left| \mathrm{f^M}_{n,-}(\vec{x}) - \mathrm{f^O}_{n,-}(\vec{x}) \right|^2 \right) \tag{2.14}$$

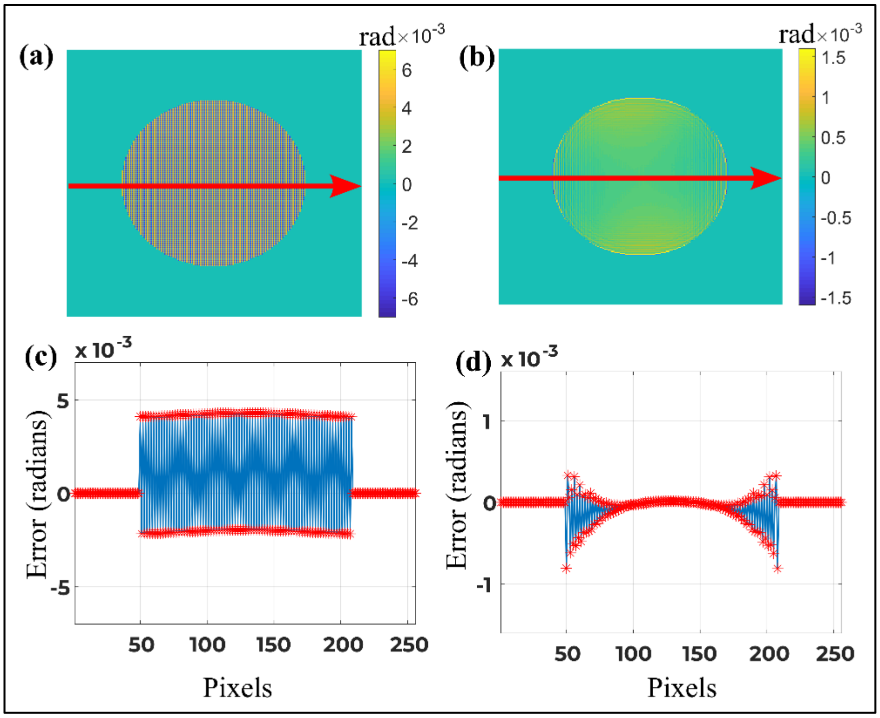

FIGURE 2.8: (a) Error map before filter (RMS error: 4.1E-3 rad), (b) Error map after filter (RMS error: 0.42E-3 rad), (c) Profile of error map before filter, (d) Profile of error map after filter

Figure 2.9a shows that the loss function converges after 30 iterations of the reconstruction without a Fourier filter. Given the filter's effectiveness in Figure 2.8, we have investigated the use of the filter within the reconstruction algorithm. The sudden surge at the start of the loss function in Figure 2.9a is a characteristic feature of phase retrieval and reconstruction algorithms. The temporary increase of the value of the Loss function is expected because the solver climbs out of the local minimum. Other phase retrieval algorithms such as the “hybrid input-output algorithm” [8] show a similar behavior.

Two cases were considered for this study: (i) using the filter after every 5 iterations and (ii) applying the filter in every iteration. Figure 2.9b shows that applying a filter enables a drop in the convergence values in both cases, thus indicating an improvement in the reconstruction process. Interestingly, the reconstruction algorithm for case (i) consistently converges back to the solution containing the high-frequency artifact. Therefore, we recommend employing a Fourier filter within the wavefront reconstruction algorithm to suppress all undesired artifacts continuously.

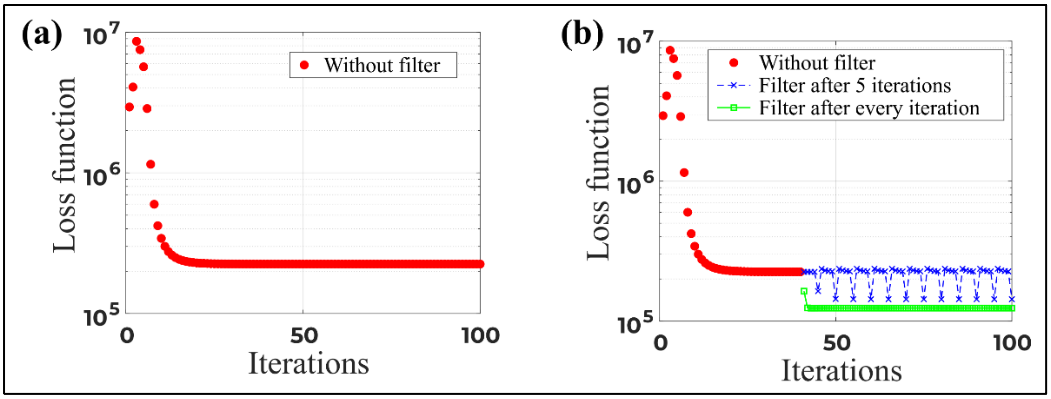

FIGURE 2.9: Evolution of loss function (a) without filter, (b) with filter

Please note, the algorithm described is a modified version of the alternating projections algorithm developed by Konijnenberg et al. in [16]. For better clarity we summarize the differences to the original algorithm from [16].

- The data recorded from experiments in [16] are in the Fourier domain. In this paper, all recorded data from experiments are in the spatial domain.
- Eq. 2.10 is the modified version of the object constraint equation. The original equation (Eq. 2.10 in [16]) was defined in the spatial domain. In this paper, this equation is defined in the Fourier domain.
- Eqs. 2.12 and 2.13 are the modified versions of the measurement constraint equations. The original equations (Eqs. 2.15 in [16]) were defined in the Fourier domain. In this paper, these equations are defined in the spatial domain.
- The algorithm in [16] uses two sets of equations in measurement constraint (Eqs. 2.15 and 2.16 in [16]), a rough-reconstruction equations for initial convergence (Eqs. 2.16

in [16]) and a fine-reconstruction equations for final refinement (Eqs. 2.15 in [16]). This paper only uses the modified versions of the fine reconstruction equations.

- After initial convergence, we include a Fourier filter in the measurement constraint equations to mitigate the effects of high-frequency artifacts.
- Multi-resolution technique [10] is incorporated into this algorithm to mitigate the effects of initial guess and improve convergence.

2.2.9. Comparison of the two configurations: (Simulation)

In the cartesian coordinate shear system, there is the freedom to choose the shear in the X and Y direction independently. However, the optical configurations shown in Figure 2.2 are restricted to one quadrant due to geometrical constrains. In principle, this limitation may be overcome using a 4f- optical setup (obtain positive and negative shears for a grating pair). However, this configuration increases the size of the system. There is freedom in the polar coordinate shear system to choose shears across all four quadrants, but these shears lie on a circle with a constant radius. When these shear systems are implemented experimentally, the shear amount cannot be controlled directly and estimated.

The choice of shear selection has an impact on the reconstruction of the wavefield. In general, increasing the number of shears provides more information on the object wavefield for the algorithm to reconstruct the wavefield. However, improper selection of shears could also lead to the algorithm not having sufficient frequencies to reconstruct the object wavefield, thus resulting in artifacts. We want to highlight this typical behavior of this system via simulation using a few exemplary sets of shears, as shown in Figure 2.10.

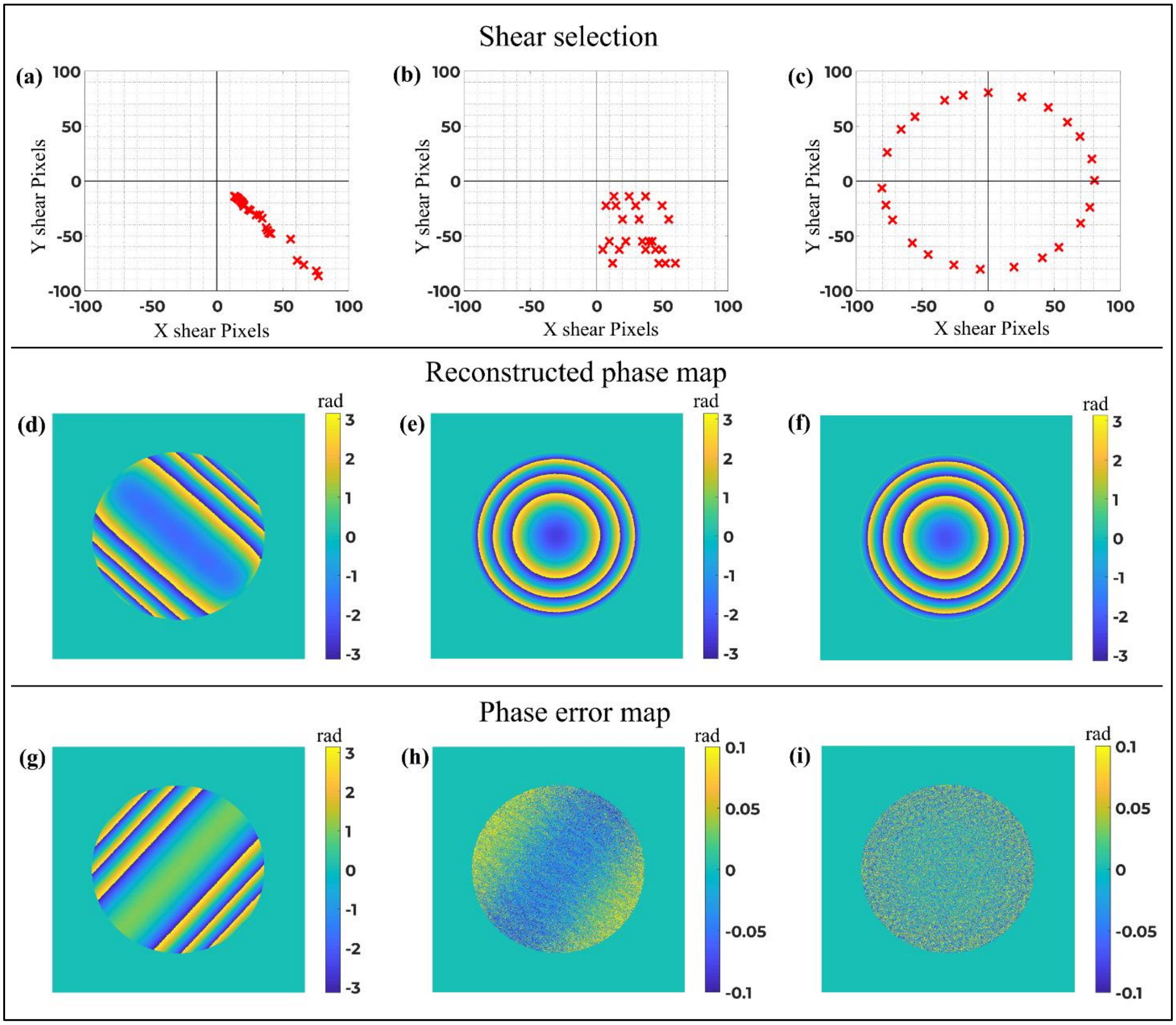

FIGURE 2.10: Comparison of reconstruction results between different configurations. (a) Shear selection for test 1 in cartesian coordinate configuration, (b) Shear selection for test 2 in cartesian coordinate configuration, (c) Shear selection for polar coordinate configuration, (d) Reconstructed phase map from test 1, (e) Reconstructed phase map from test 2, (f) Reconstructed phase map from polar coordinate configuration, (g) Phase error map from reconstruction using test 1 parameters, (h) Phase error map from reconstruction using test 2 parameters, (i) Phase error map from reconstruction using polar coordinate configuration

Each simulation was performed with 24 shears, where the selections are shown in Figures 2.10a, 2.10b, and 2.10c. The selections analyze two possible xy-shearing configurations shown in

Figure 2.10a and 2.10b (see Figure 2.2 for configuration) and the fixed shear with variable shear axis shown in Figure 2.10c (see Figure 2.3 for configuration).

In test 1 (Figure 2.10a), the shears have been selected along an approximately linear trend. The reconstructed phase map from this shear selection showed that some of the frequencies were not being reconstructed correctly, which is a consequence of the ambiguity that arises from the measured data. The reconstruction results are shown in Figures 2.10d and 2.10g. When the selection of shears was scattered across one quadrant (Figure 2.10b) as in test 2, the reconstruction algorithm had sufficient data to reconstruct most of the point-source wavefield, as shown in Figure 2.10e. However, the error map in Figure 2.10h shows a curvature, indicating the possibility of some missing frequencies. This slowly varying error is critical as it produces a so-called form error that is difficult to filter out when observing aperture size measurement objects (e.g., mirrors or lenses under test). This error may be less critical when the sample is small (e.g., in the case of a cell under a microscope). The shear selection shown in Figure 2.10c is based on a variable shearing axis but with a fixed shear amount. The latter system allows accessing all four quadrants, and the shears can be selected at all possible rotation angles of the shear axis. The reconstruction is shown in Figure 2.10f. The error map shown in Figure 2.10i shows that the error map is dominated only by high-frequency noise patterns, which can be filtered more easily. These results demonstrate that selecting shears across all quadrants results in better reconstruction because it provides more information for a successful reconstruction.

2.2.10. Transfer function analysis (see also [22]), to estimate frequency domain information densities

To better understand the results and characteristics features in the error maps of Figure 2.10, further study was done using transfer function analysis to investigate the effectiveness of the selected shear sets to transmit information for wavefield reconstruction. Extensive studies have been done by Falldorf [25] for non-symmetric shears and Servin [22] for symmetric shears in understanding the frequency response of spatially shearing systems. Inspired by Servin's description [22] for the transfer function, we define the frequency information density as

$$T(k_x, k_y) = \sum_{n=1}^{S} sin^2\left[2\pi\vec{k}.\overrightarrow{ds_n}\right] \tag{2.15}$$

where $\vec{k} = [k_x, k_y]$ is the frequency coordinate and $\overrightarrow{ds} = [ds_x, ds_y]$ is the shear in x- and y-directions. This transfer function analysis estimates the "frequency information density" at each spatial frequency coordinate for a given set of shears. These functions were evaluated and mapped for all three configurations as shown in Figure 2.11.

Figures 2.11(a), (b) and (c) are the frequency domain information density maps for the three shear sets described in Figure 2.10. Figures 2.11 (d), (e) and (f) are the same maps but zoomed in near low spatial frequencies to visualize better the behavior at these regions, where regions below the threshold of 2 are highlighted in red. Figure 2.11d shows a significantly high amount of frequency sets that have transfer function values below the threshold. These cluster appear to dominate in regions where kx ≈ ky. This indicates that a large number of frequencies along the 45-degree angle will have poor reconstruction in the estimated wavefield at longer spatial wavelengths. This conclusion is in agreement with the Figure 2.10g. A similar behavior is observed in Figures 2.11b and 2.11e, however, the number of frequency sets with transfer function values below the threshold of 2 are located at both low and high frequencies, with a minimal presence near low spatial frequencies. The locations of these cluster indicate that very low spatial frequencies will appear in the error map but will have better reconstruction than the previous shear set. This is observed in Figure 2.10h, but there are also high frequency errors present due to low values of the transfer function at higher spatial frequencies. The polar configuration in Figure 2.11f has no transfer function values below the threshold of 2, except for the (trivial) frequency at (0,0). This indicates good reconstruction of the estimated wavefield at all spatial frequencies.

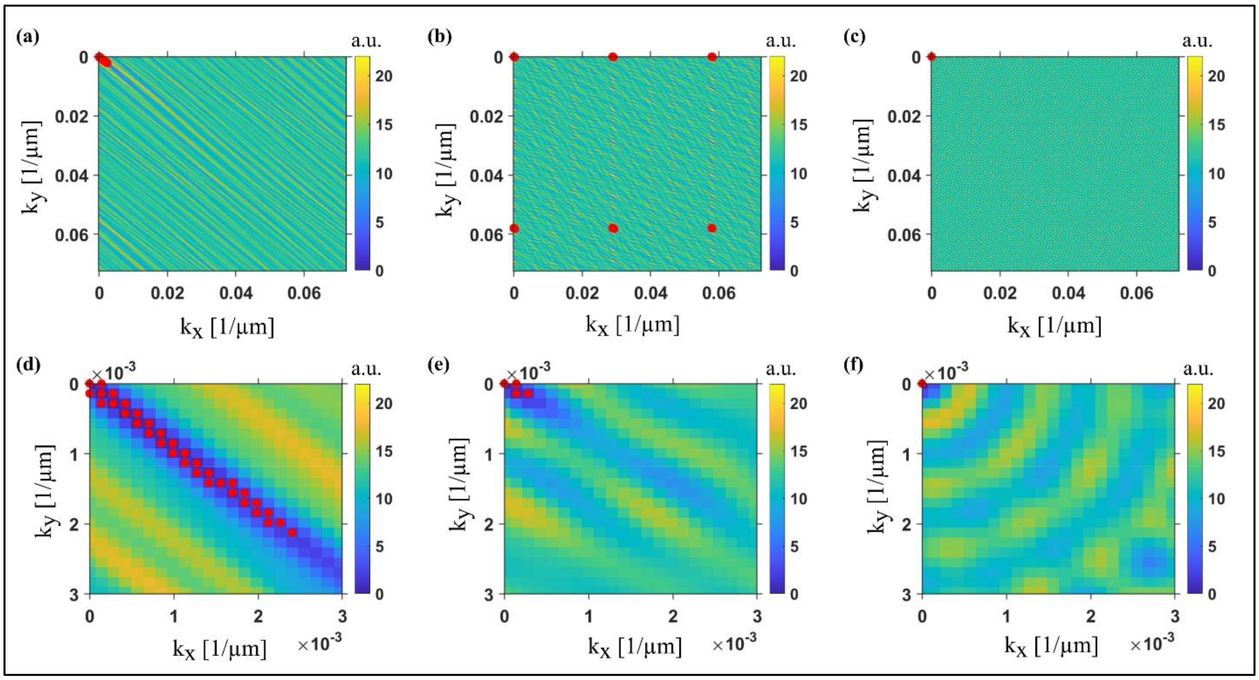

FIGURE 2.11: Transfer function analysis (Frequency information density plots with points below threshold 2): (a) Test 1in cartesian coordinate configuration (34 datapoints below threshold), (b) Test 2 in cartesian coordinate configuration (21 datapoints below threshold), (c) Polar coordinate configuration (1 datapoint below threshold), (d) Test 1 plot in cartesian coordinate configuration zoomed near small frequency regions, (e) Test 2 plot in cartesian coordinate configuration zoomed near small frequency regions, (f) Polar coordinate configuration plot zoomed near small frequency regions

2.2.11. Spatial support analysis (see also [22]), to estimate spatial domain information densities

The following section demonstrates how spatial overlaps between different shears impact the reconstruction of the final wavefield. When an object wavefield passes through the gratings, it splits in two, represented as beam 1 and 2 in Figure 2.12a. Depending on the shear amount, there is an overlap region between the two beams (overlap region is indicated in yellow). Since the overlap region produces an interference pattern, the phase information from the overlap region feeds into the algorithm. Figure 2.12b shows which areas of the input beam provide phase information to the reconstruction algorithm (regions indicated in yellow).

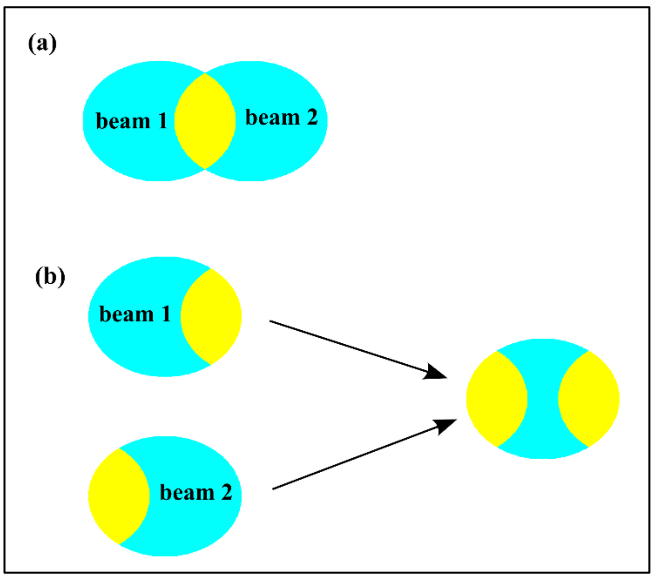

FIGURE 2.12: Demonstration of data recorded by each shear: (a) Beam 1 and 2 overlapping, (b) Summation of overlapped regions indicating regions that have data for reconstruction (yellow regions)

This idea is further extended to multi-shear interferometry in Figure 2.13. Figure 2.13a shows the overlap regions from an object beam with a diameter of 600 pixels sheared by 175 pixels along the x-direction. Figure 2.13b shows the overlap regions if a second shear is added to the measurement in the orthogonal direction by the same amount. In Figure 2.13b the yellow areas indicate regions with two overlaps, green areas indicate regions with one overlap, and the dark blue areas indicate regions with no overlap. This idea is extended over 24 shears in Figure 2.13c, showing a significantly higher count of overlaps (or number of effective measurements). This case also shows an example of a situation where the algorithm will not completely reconstruct all spatial frequencies near the wavefront's center because the chosen fixed shear is too large (175 pixels). Figure 2.13d shows an alternative set of 24 shears (i.e., with a small shear amount compared to (c) with 80.5pixels). There all of the spatial locations have been measured at least 20 times. The case presented in Figure 2.13d has the highest potential to successfully reconstruct the wavefield due to maximum overlap across the whole area.

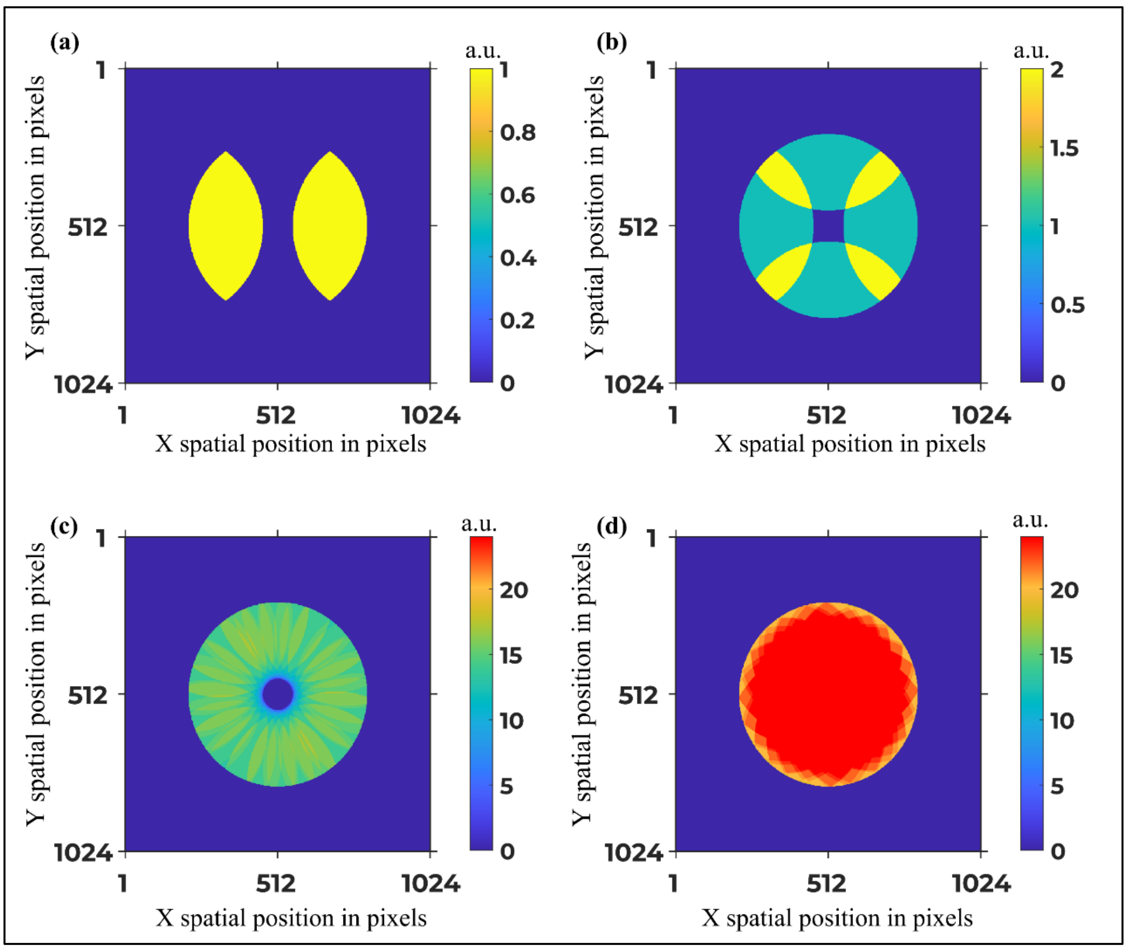

FIGURE 2.13: Spatial information density distribution for different shear patterns on 1024×1024-pixel maps with aperture diameter of 600 pixels. (a) Single shear of 175 pixels , (b) Two orthogonal and equal shears of 175 pixels, (c) 24 shears in polar configuration with a fixed shear of 175 pixels, (d) 24 shears in polar configuration with a fixed shear of 80.5 pixels

It should be noted that (as discussed by Servin [22]) the wavefront may be reconstructed even at regions where there is no overlap. This phenomenon is especially true for lower spatial frequencies because they do not need to be sampled everywhere. However, the reconstruction is increasingly difficult at higher spatial frequencies at a given location if no interference exists. The same concept is applied to the three configurations / shear sets discussed in Figure 2.10 and the overlap distribution is mapped in Figure 2.14. Figures 2.14 (a) and (b) show fewer overlaps along the boundary at 45-degree angle. The number of effective measurements drops from 24 to 13. On the contrary, Figure 2.14c shows uniform distribution of overlaps covering the majority area of the object beam. At the border, there are still 20 effective measurements recorded, which indicates better reconstruction across the whole area of the object.

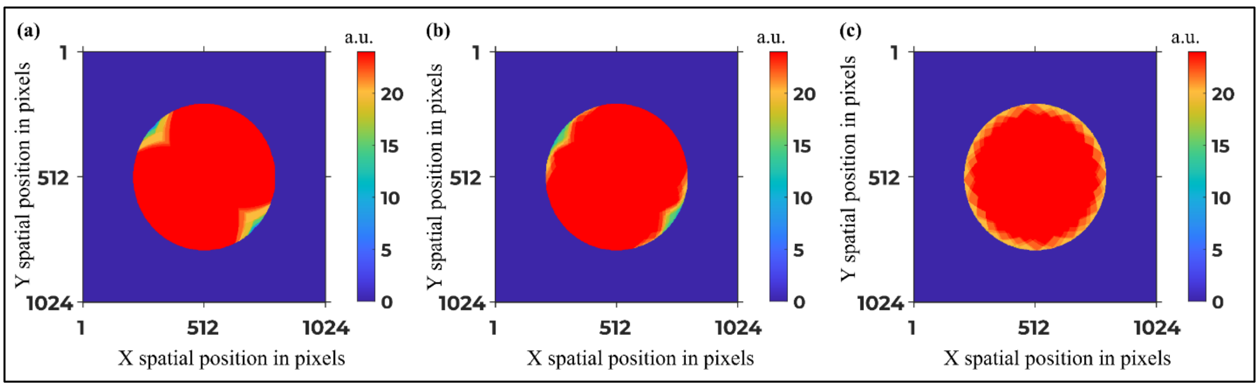

FIGURE 2.14: Spatial information density distribution across all three configurations with 24 shears. (a) Test 1 in cartesian coordinate system (linear pattern), (b) Test 2 in cartesian coordinate (shears in scattered pattern), (c) Polar coordinate system with shears at unequal angles

2.2.12. Effect of pixel shear errors on the resolution of the reconstruction (Monte Carlo simulation)

Any error present in the estimated shear value propagate through the reconstruction process and result in an error in the final reconstructed wavefield. This mismatch between actual and assumed shear amounts can result in error artifacts in the reconstructed wavefield or missing frequencies from the original wavefield. Monte-Carlo simulations were carried out to evaluate the effect of errors in the estimated pixel in reconstructing the wavefield by adding normal distributed random errors to the shear values in X and Y direction for the shear configuration in Figure 2.10c (100 simulations for each case). Furthermore, a total of 20% intensity noise (of the peak value) has been added to all interferograms to include the effects of noise in realistic measurement conditions.

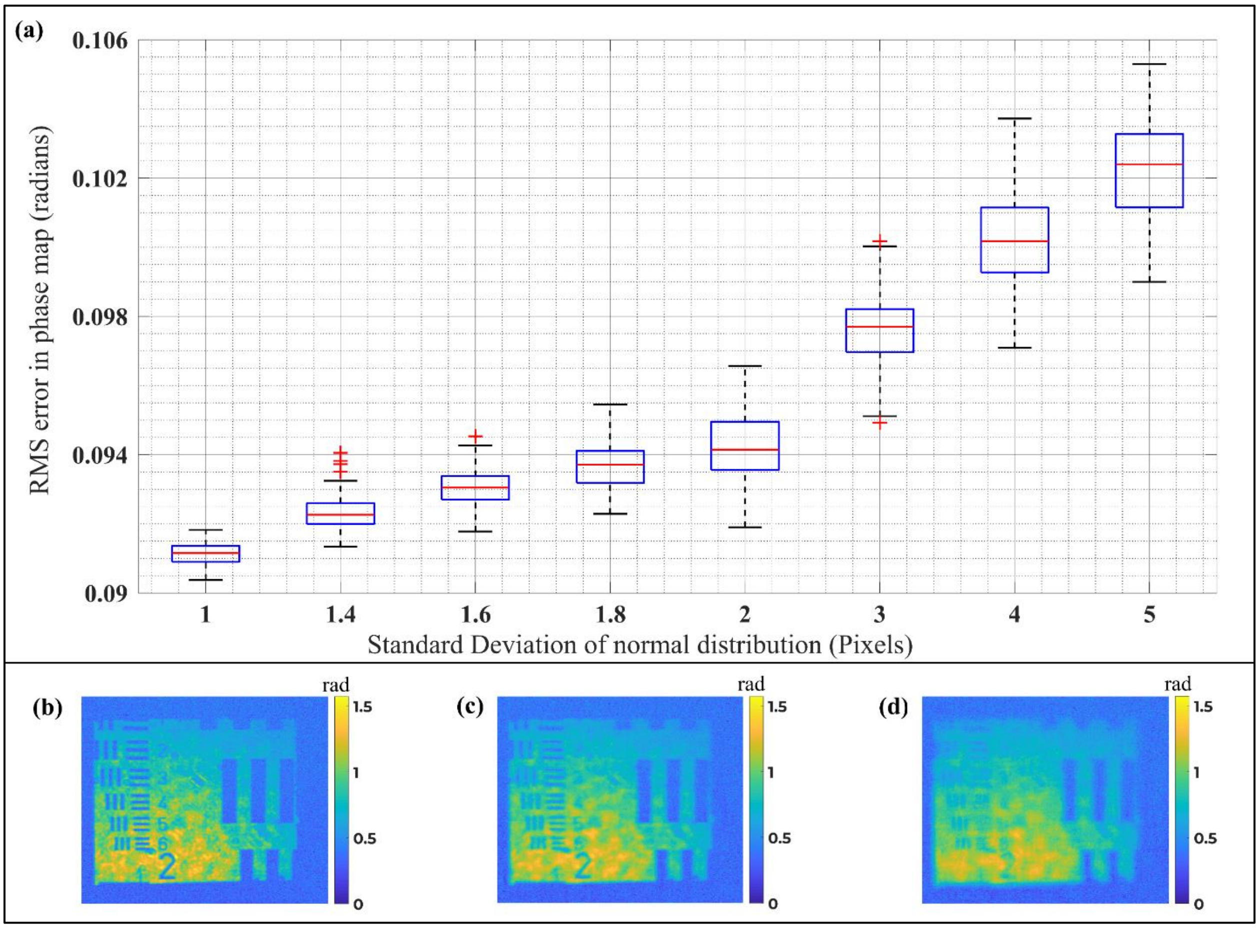

FIGURE 2.15: (a) Box-plot showing a summary of the simulations, (b) Reconstructed phase map at standard deviation 1 pixel, (c) Reconstructed phase map at standard deviation 3 pixels, (d) Reconstructed phase map at standard deviation 5 pixels

This series of simulations provides an overview of how the phase errors in reconstructed wavefields are affected by the imperfect shears. The results of the series of simulations have been summarized in a box plot, as shown in Figure 2.15. As expected, when observing the RMS error in the reconstructed phase, there is a clear correlation with the increasing amount of shear error. However, it is interesting to notice that the different spatial frequencies are affected in different ways; as the standard deviation of the shear error increases, the ability of the algorithm to reconstruct higher spatial frequencies decreases. Figures 2.15 (b), (c), and (d) show the measurement of a USAF target where the Monte Carlo simulation used a shear error of 1-, 3-, and 5-pixels standard deviation, respectively.

2.2.13. Additional processing of measurement data needed for experimental data (Shear detection)

The reconstruction algorithm requires the shear amount to be known. As concluded from the Monte Carlo simulations, the better the estimation of the shear amount, the lower the reconstruction error and the higher the spatial resolution. In this work, we have estimated the shear amount by calculating the auto-correlation of the recorded intensity maps. To increase the robustness of this estimation, we have removed the sinusoidal fringe modulation by averaging all four measured phase-shifted intensity patterns. One exemplary measurement is shown in Figure 2.16a. The second-order derivative of the auto-correlation map has been computed along one direction to further enhance the peak in the auto-correlation map. The resulting spikes for the case in Figure 2.16a are shown in Figure 2.16b, and they are prominently identifiable. The second-order derivative of the auto-correlation map comprises three peaks: a center peak and a peak on either side of the center peak, which is located at twice the value of the actual positive and negative shear amounts. The shear amount is estimated by tracking one of the peak positions to the center peak. The difference in X and Y coordinates of the side and center peak gives twice the shear value for each averaged intensity map. The actual shear can be detected down to an accuracy of 0.5 pixels.

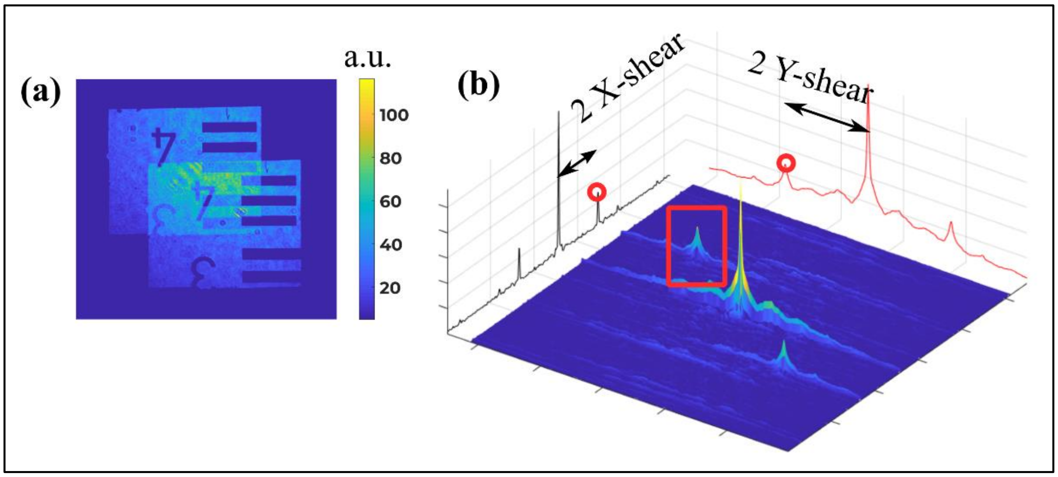

FIGURE 2.16: (a) Intensity map with sheared images of object, (b) Second derivative of auto-correlation map showing peaks corresponding to shear in X and Y direction

2.2.14. Additional compensation techniques for the polarization camera

When working with left and right circular polarized waves, it is convenient to employ pixelated polarization cameras to record four phase-shifted intensities simultaneously. The polarization camera enables single-shot phase-shifting during the measurement process for each shear. The single-shot phase-shifting capability offers an advantage in reducing the number of translation axes, enhanced stability, and mitigation of alignment errors. The reduction of the number of translation axes further ensures repeatability.

Commonly, each super-pixel on the detector of the polarization camera has four pixels that record the image at four different polarizer angles. As the two incident waves have a left-circular and right-circular polarization, it is possible to obtain simultaneously four interferograms at four different phase shifts. The orientation of this pixelated array is shown in Figure 2.17, which also shows an example of a defocused point source measured at a single fixed shear with 0°, 90°, 180°, and 270° phase shifts. The recorded intensities have a resolution of 1024 x 1024 pixels. One critical correction is needed before the phase can be calculated. The individual frames are often clustered in a super-pixel and can be separated without difficulty. However, all four frames are not located at the same spatial position. An additional interpolation is needed (e.g., including even the Fourier shift theorem) to obtain all four interferograms at the same spatial location. In this work, we have compensated this spatial mismatch for the interferograms I2, I3, and I4 (but not I1), to obtain an interferogram that is shifted by ½ super-pixels.

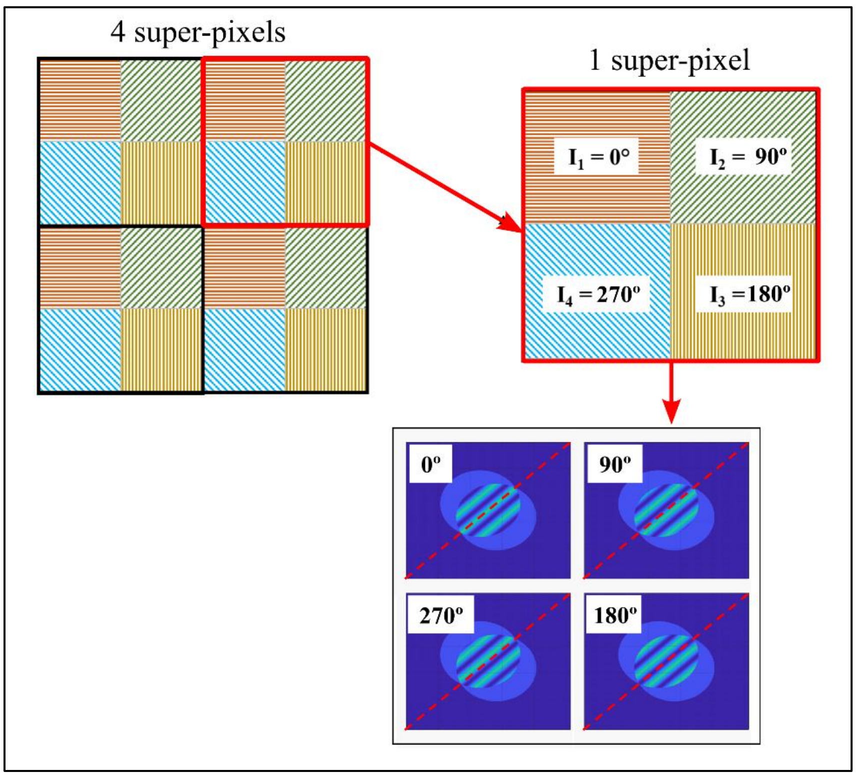

FIGURE 2.17: Schematic of the polarization camera sensor and intensity maps demonstrating the phase shifts (Intensity maps generated using synthetic defocused point source wavefield)

2.3. Experimental setup:

2.3.1. Cartesian Coordinate Shear configuration

Figure 2.18 shows the experimental setup for the Cartesian coordinate shear setup, along with a schematic showing the arrangement of optical components for the setup. The light source illuminating the object is a class 3B, 520 nm wavelength, 30 mW green laser. The object used for the experiments is a USAF target. Two sets of lenses with 4f configuration were used to keep the aperture 1 and the object in focus. Aperture 2 was used to limit the effects of stray light, back reflections, and the higher-order diffraction orders. A polarization camera was used to capture the four phase-shifted interferograms simultaneously (FLIR Blackfly-S model BFS-U3-51S5P-C). The grating arrangement is shown in detail in Figure 2.19.

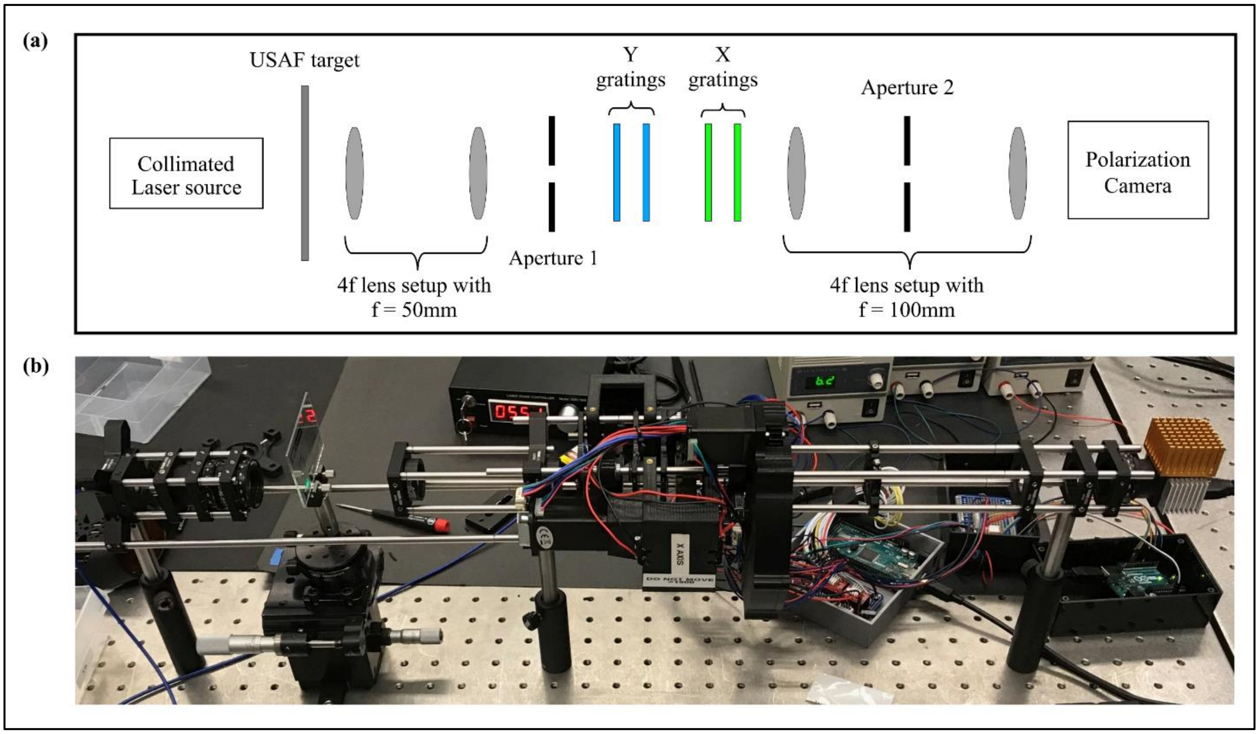

FIGURE 2.18: Experimental setup for Cartesian coordinate shear setup (a) Schematic (b) Experiment

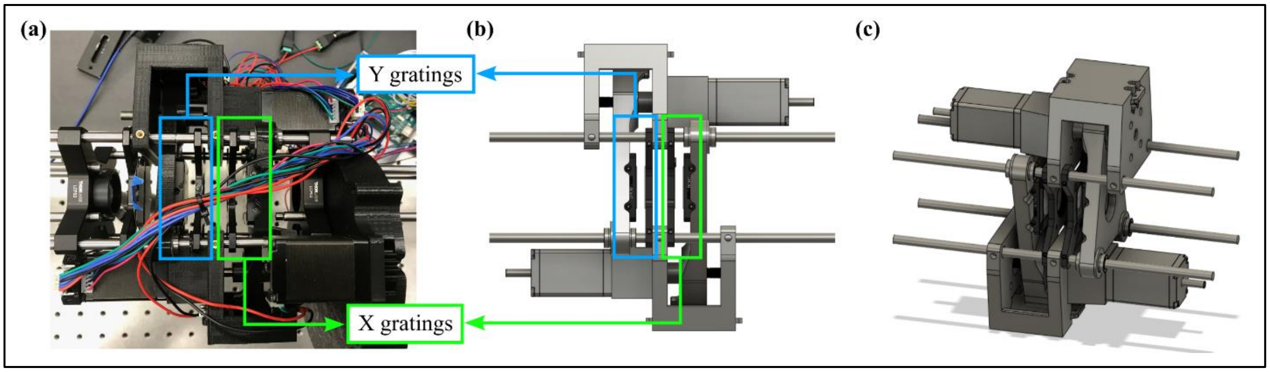

FIGURE 2.19: Grating arrangement in Cartesian coordinate shear setup (a) Experimental setup, (b) Schematic of the setup, (c) 3D schematic of the setup

The cartesian coordinate shear system in Figure 2.19a has four polarization gratings, two on the left-hand side (blue) to shear the wavefield in the vertical direction (y-direction), and the two on the right-hand side (green) to shear the wavefield in the horizontal direction (x-direction). Two leadscrew stages are connected to the two outermost X and Y polarization gratings which translate along the Z-axis to create the shears. The leadscrew stages utilize stepper motors and encoders to accurately determine the stages' position and limit switches for homing the system. Additive manufacturing (3D printing) was used to construct the stage, and accompanying electrical circuitry and software were developed for the closed-loop control system. The two inner gratings are fixed. Since only one grating can move in each grating pair, the shears are limited to only one quadrant (see Figure 2.10a and 2.10b).

An experiment was carried out to validate the previous findings regarding the shear configuration in Figure 2.10a. The results for the first configuration are shown in Figure 2.20, where a total of 24 different shear amounts have been applied (see Figure 2.20a) using an instrument that can independently adjust the x- and y- shears. The object used in this experiment is a simple section of an amplitude USAF target, where the remaining sections are blacked out due to aperture 1 (see Figure 2.18a).

The shears were estimated from experimental data using the auto-correlation method, as discussed in the previous section. Once the shears were estimated, they were given as input to the algorithm to reconstruct the wavefield. A multi-resolution technique [10] was implemented within the reconstruction algorithm to mitigate the effects of initial guesses and improve the convergence. For our dataset with 1024 x 1024 pixels, a 5-level multi-resolution reconstruction starting from the coarsest grid with 64 x 64 pixels was implemented. The estimated wavefield is then up-sampled by a factor of 2, and the reconstruction process happens at a higher resolution (i.e., 128 x 128 pixels) using the newly up-sampled wavefield as the initial guess. This process repeats until the estimated wavefield reaches the original resolution, i.e., 1024 x 1024 pixels. The results for this 5-layer multi-resolution approach are shown in Figure 2.20.

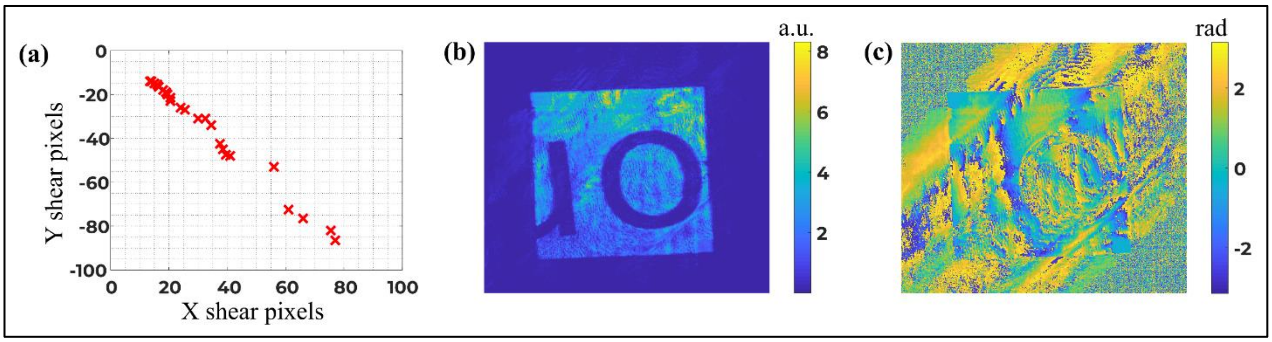

FIGURE 2.20: Reconstructed results from cartesian coordinate shear experiment
(a) Shear selection, (b) Amplitude map, (c) Phase map

The reconstructed amplitude map (Figure 2.20b) shows the object features that would be expected. However, the phase map in Figure 2.20c shows the presence of parasitic signals. This reconstruction is expected given the outcome of previous simulations, see Figure 2.10. This is a direct consequence of the shear selection: most of the shears selected for this experiment are dominant along the -45° angle. This selection has generated parasitic signals along the 45° angle, as seen in Figure 2.20c.

2.3.2. Constant shearing Polar coordinate shear configuration

The other shear configuration that produced consistently better results was the configuration of a fixed shear with a variable shear axis, see Figure 2.10c. An experimental implementation is shown in Figure 2.21, where the xy-shear system in Figure 2.18 is replaced with a simple two grating set up on a rotational mount. Figure 2.22 shows a more detailed view of the shearing mechanism. Notably, the 2-grating setup can be realized in a more compact optical setup; however, we chose to keep the 4f configuration to compare the two setups better. The results for the configuration in Figure 2.21, using 24 different shear amounts, are shown in Figure 2.23. Similar to the case of Figure 2.20, a portion of the USAF target has been selected for the measurement, and the field of view is limited by aperture 1 (see Figure 2.21).

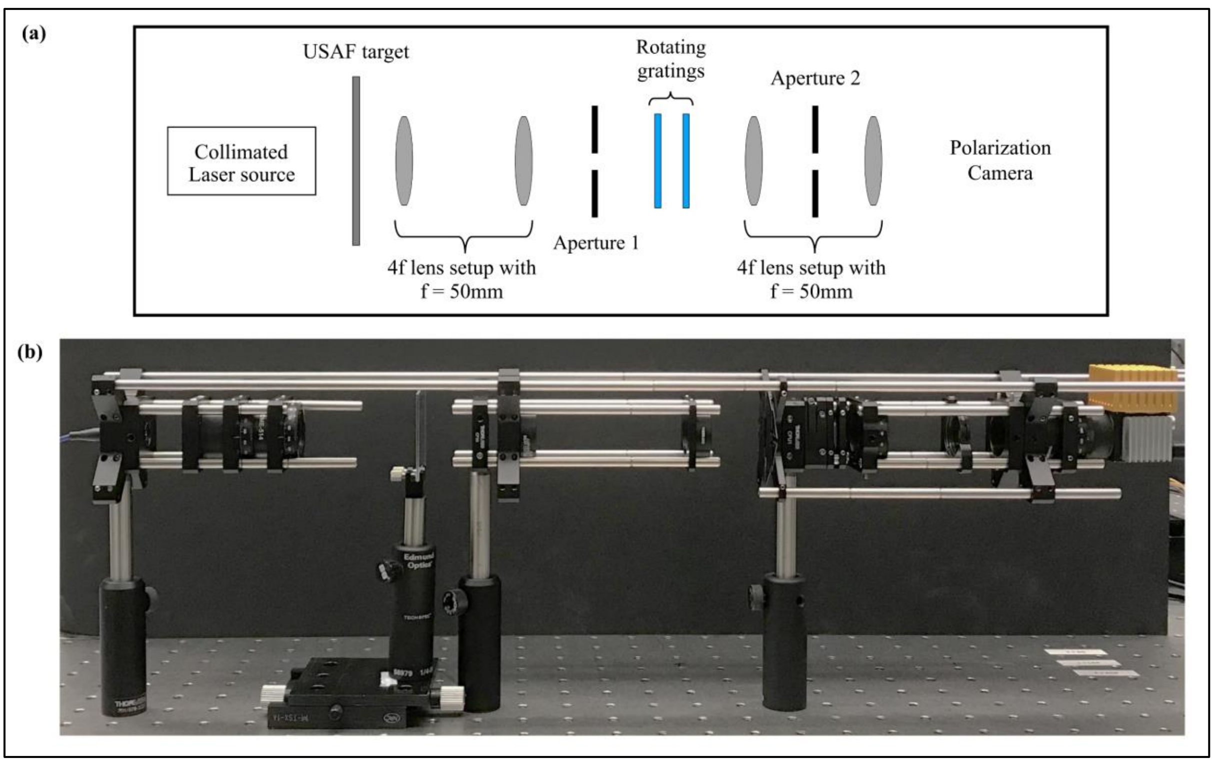

FIGURE 2.21: Experimental setup for polar coordinate shear system,
(a) Schematic, (b) Experiment

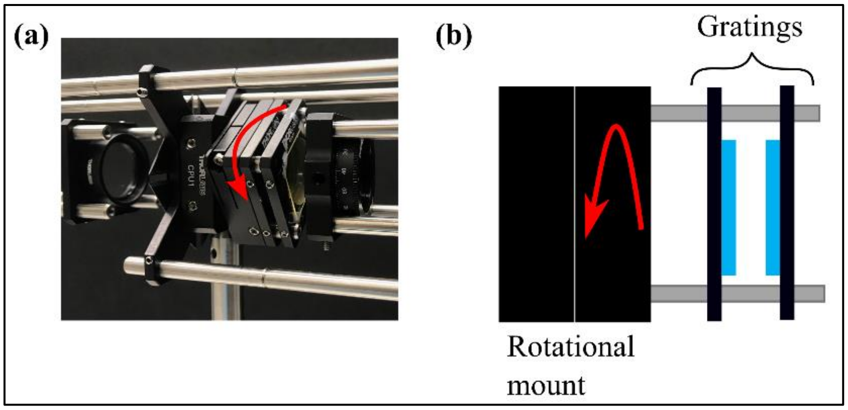

FIGURE 2.22: Gratings arrangement in polar coordinate shear configuration (a) Experimental setup showing the rotation of gratings, (b) Schematic of the grating arrangement

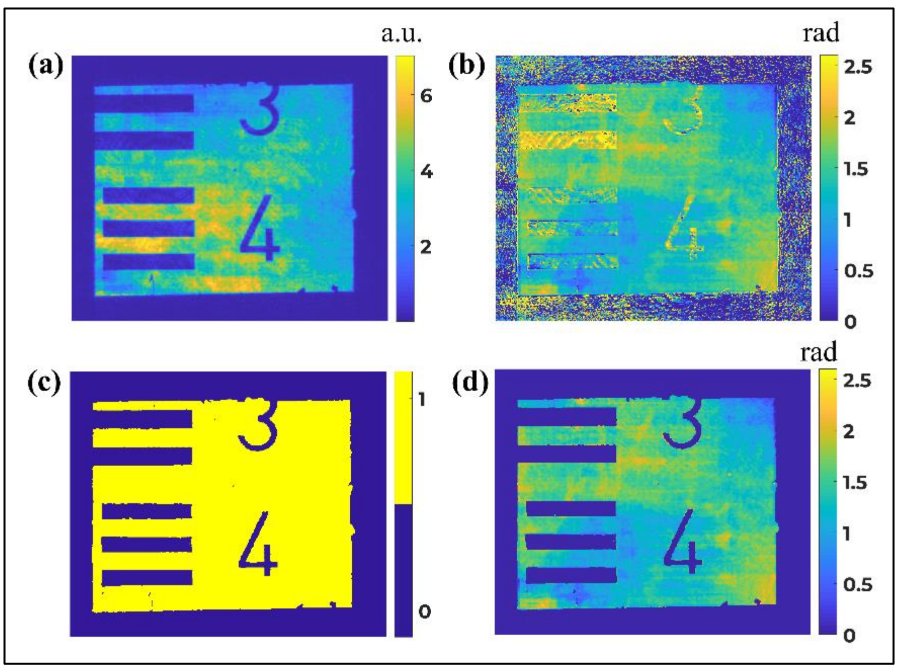

FIGURE 2.23: Reconstructed results (a) Amplitude map (b) Phase map
(c) Mask from amplitude map (d) Phase map with mask applied

Figures 2.23a and 2.23b show that the solver successfully reconstructs both the amplitude and the phase map, free of parasitic fringes. For better visualization, a mask has been generated (see Figure 2.23c) using the amplitude information and applied to the phase data (see Figure 2.23d).

A further experiment has been conducted to verify that the instrument in Figure 2.21 can capture and reconstruct the wavefield at a defocused distance. For this purpose, we shift the camera's position by a distance of ~170mm, so that both the object and the aperture get defocused by the same amount.

The reconstructed wavefield is shown in Figures 2.24a and 2.24c. After reconstruction, the wavefield was numerically refocused to the visually best reconstruction distance (z=162.94 mm) using the Angular Spectrum method [26,27]. The results of the refocused wavefield are shown in Figures 2.24b and 2.24d. For better visualization, various regions of the reconstructions have been zoomed in and are presented in Figure 2.25.

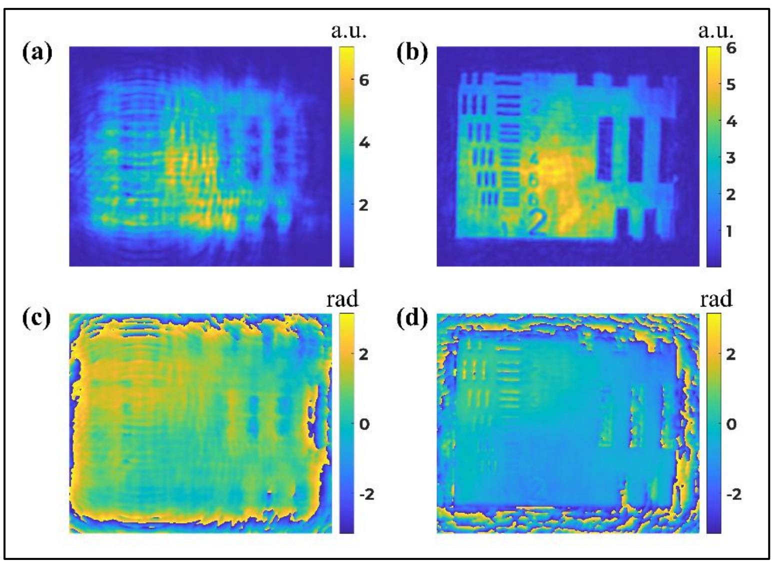

FIGURE 2.24: Reconstructed results from defocused object (a) Amplitude map before numerical refocusing (b) Amplitude map after numerical refocusing (c) Phase map before numerical refocusing (d) Phase map after numerical refocusing

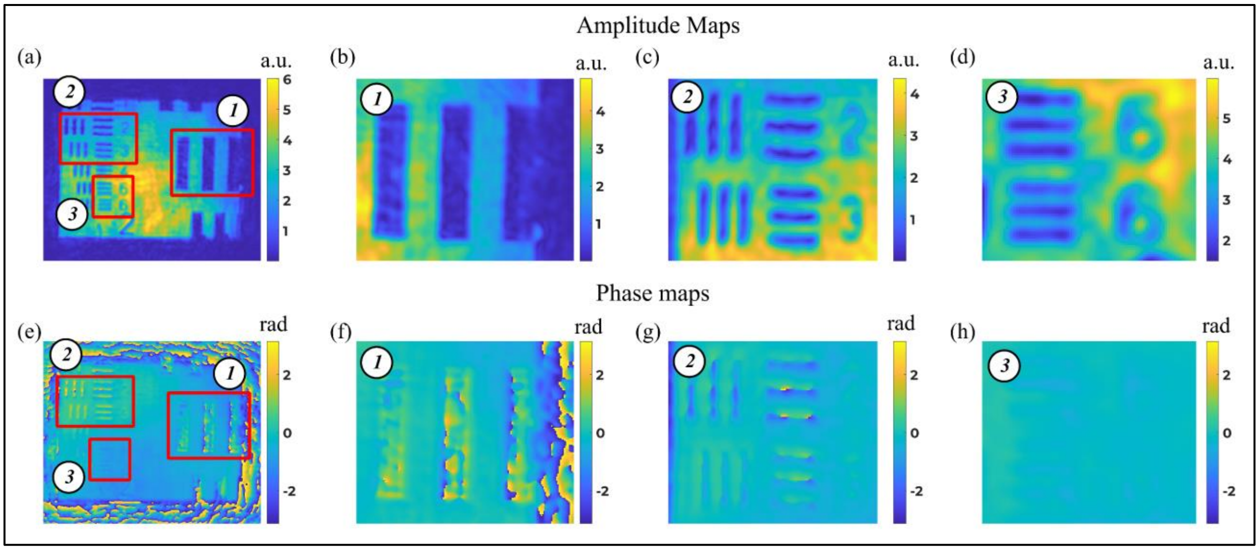

FIGURE 2.25: Reconstructed wavefield of defocused object (zoomed) after post processing: (a) Amplitude map of the full object, (b) Region 1 amplitude map (c) Regions 2 amplitude map (d) Regions 3 amplitude map, (e) Phase map of the full object, (f) Region 1 phase map, (g) Region 2 phase map, (h) Region 3 phase map

2.4. Materials and methods

The light source used for the experiment is an FC-520-040-PM laser system (520 nm, 30 mW) from Civil Laser. The object sample is a combined USAF 1951 and Dot Grid Target (Edmund Optics #62-465). The GP gratings have been purchased from Edmund Optics (#12-677, 96% diffraction efficiency at 550nm, 159grooves/mm, 25 x 25 x 0.45 mm). The light illuminating the object is linearly polarized to produce 50% RHCP and 50% LHCP at the GP grating, maximizing the fringe visibility. The camera used for imaging is a FLIR Blackfly-S model BFS-U3-51S5P-C polarization camera. The lenses used for the 4f-configuration have an effective focal length of 50mm.

2.5. Conclusion

In this work, a GP grating-based shearing holography system has been presented. The GP gratings used in this work have the unique ability to have a polarization-sensitive diffraction angle, where the RHCP and LHCP light beams are diffracted in two different directions. Figures 2.1, 2.2, and 2.3 show how these properties can be exploited with a linear polarizer to create an adjustable shearing interferometer. This paper presented two distinct configurations, (i) one that allows for adjustable xy-shearing, and (ii) one that keeps the shear amount constant but rotates the shear axis. Another aspect of the GP grating-based shearing interferometer is that a series of phase-shifted interferograms can be obtained by either rotating the polarizer (see Figure 2.4) or using a pixelated polarization camera (see Figure 2.17).

The ability to produce a series of phase-shifted interferograms obtained under various shear amounts opens the possibility to obtain high fidelity data that can be processed in a wavefront reconstruction algorithm. In this work, we have implemented the approach of Konijnenberg [16] outlined in Figure 2.5 but added a filtering procedure to remove algorithm-specific artifacts (see Figures 2.6d, 2.7, 2.8, and 2.9). We further investigated the effect of the shear selection. Figure 2.10 showed that choosing the shears to be on a circle in the sx-sy plane provides consistently good results, where the error is of high-frequency nature. These findings are supported using Servin's [22] transfer function analysis and spatial domain support that were referred to as "frequency domain information density" (see Figure 2.11) and "spatial domain information density (see Figure 2.14). One critical step is the estimation of the exact shear amount. Any discrepancy between the actual shear amount and the values used within the wavefront reconstruction algorithms will increase, to some degree, the RMS in the reconstructed phase, see Figure 2.15. However, the results in Figure 2.15 also show that an imperfect shear value has a strong impact on the resolution of the reconstructed wavefield (even if the RMS increases only marginally by 10%, for the case of typical levels of intensity noise). To ensure accurate results, we have reported a shear estimation technique using the second derivative of the autocorrelation function, where the spikes of that function estimate shear amount down to an accuracy of 0.5 pixels, as shown in Figure 2.16. The reconstruction algorithm presented in this paper does not limit the possible applied shears. The algorithm can process sub-pixel shearing as the algorithm primarily operates on FFTs. However, the shear detection technique presented in this paper is limited in identifying shears. The procedure detects twice the values of shears for a sheared interferogram as integer, and hence the shears can be estimated down to integer multiples of 0.5 pixels. More sophisticated shear detection algorithms (using weighted mass algorithms or techniques based on ideas from Guizar-Sicairos M. et al. [28]) might enable finer shearing detection down to 0.01 pixels and are subject to future research.

The previous aspects have been verified experimentally for both shearing configurations, as shown in Figures 2.18 and 2.19 for the xy-shearing component and Figures 2.21 and 2.22 for the configuration that rotates the shear axis. As expected, the system configuration that keeps both gratings fixed while the grating pair rotates about the optical axis provides the visually best reconstruction result with no parasitic fringes, as shown in Figure 2.20 and 2.23. A further advantage of the setup with the variable shear axis is that it requires only two GP gratings and can be, in principle, incorporated into a more compact setup. There are also several motorized rotating mounts available that could automate this process.

Finally, we demonstrate the feasibility of this approach by reconstructing the wavefield of a defocused object at the distance z=162.94 mm. Refocusing using the Angular Spectrum method [26,27] produces Figures 2.24 and 2.25.

These findings show the advantage of GP grating-based shear interferometers compared to conventional dual grating (or dual double-grating) configurations. A conventional dual-axis grating-based variable shearing interferometer with phase shift capabilities requires two independent axial shifts of the x- and y- gratings (to adjust the shear) and lateral shifts of the gratings in x- and y- direction (for phase-shifting). Having to control four mechanical axes independently is a significant system complexity, where the freedom to adjust all parameters appropriately is often compromised due to space constraints. In contrast, the results of this work show that a GP grating configuration with a fixed shear amount, but an adjustable rotational shear axis can provide the shear selections for robust measurements while maintaining phase-shifting capabilities using a pixelated polarization camera. In other words, robust variable shearing interferometry can be made possible by controlling only one mechanical axis (instead of four). This finding has implications for future compact interferometer designs.

REFERENCES

1. K. A. Nugent, D. Paganin, and T. E. Gureyev, "A Phase Odyssey," Phys. Today **54**, 27–32 (2001).

2. J. P. Guigay, M. Langer, R. Boistel, and P. Cloetens, "Mixed transfer function and transport of intensity approach for phase retrieval in the Fresnel region," Opt. Lett. **32**, 1617 (2007).

3. K. Falaggis, T. Kozacki, and M. Kujawinska, "Optimum plane selection criteria for single-beam phase retrieval techniques based on the contrast transfer function," Opt. Lett. **39**, 30–33 (2014).

4. J. Martinez-Carranza, K. Falaggis, and T. Kozacki, "Multi-filter transport of intensity equation solver with equalized noise sensitivity," Opt. Express **23**, 23092 (2015).

5. M. Reed Teague, "Deterministic phase retrieval: a Green's function solution," J. Opt. Soc. Am. **73**, 1434 (1983).

6. P. Almoro, G. Pedrini, and W. Osten, "Complete wavefront reconstruction using sequential intensity measurements of a volume speckle field," Appl. Opt. **45**, 8596 (2006).

7. Z. Zalevsky, R. G. Dorsch, and D. Mendlovic, "Gerchberg–Saxton algorithm applied in the fractional Fourier or the Fresnel domain," Opt. Lett. **21**, 842 (1996).

8. J. R. Fienup, "Phase retrieval algorithms: a comparison," Appl. Opt. **21**, 2758 (1982).

9. J. R. Fienup, "Phase retrieval algorithms: a personal tour [Invited]," Appl. Opt. **52**, 45 (2013).

10. K. Falaggis, T. Kozacki, and M. Kujawinska, "Accelerated single-beam wavefront reconstruction techniques based on relaxation and multiresolution strategies," Opt. Lett. **38**, 1660 (2013).

11. P. F. Almoro, A. M. S. Maallo, and S. G. Hanson, "Fast-convergent algorithm for speckle-based phase retrieval and a design for dynamic wavefront sensing," Appl. Opt. **48**, 1485 (2009).

12. K. Falaggis, T. Kozacki, and M. Kujawinska, "Hybrid single-beam reconstruction technique for slow and fast varying wave fields," Opt. Lett. **40**, 2509 (2015).

13. C. Falldorf, C. von Kopylow, and R. B. Bergmann, "Wave field sensing by means of computational shear interferometry," J. Opt. Soc. Am. A **30**, 1905 (2013).

14. C. Falldorf, M. Agour, and R. B. Bergmann, "Advanced wave field sensing using

computational shear interferometry," Interferom. XVII Adv. Appl. **9204**, 92040C (2014).

15. M. Servin, J. A. Quiroga, and M. Padilla, *Fringe Pattern Analysis for Optical Metrology: Theory, Algorithms, and Applications* (Wiley, 2014).

16. A. P. Konijnenberg, A. C. C. de Beurs, G. S. M. Jansen, H. P. Urbach, S. Witte, and W. M. J. Coene, "Phase retrieval algorithms for lensless imaging using diffractive shearing interferometry," J. Opt. Soc. Am. A **37**, 914 (2020).

17. P. Blain, P. Piron, Y. Renotte, and S. Habraken, "An in-line shearography setup based on circular polarization gratings," Opt. Lasers Eng. **51**, 1053–1059 (2013).

18. K. Choi, J. Yim, and S.-W. Min, "Achromatic phase shifting self-interference incoherent digital holography using linear polarizer and geometric phase lens," Opt. Express **26**, 16212 (2018).

19. L. A. Alemán-Castaneda, B. Piccirillo, E. Santamato, L. Marrucci, and M. A. Alonso, "Shearing interferometry via geometric phase," Optica **6**, 396 (2019).

20. J. C. Wyant and J. E. Millerd, "Simultaneous phase-shifting Fizeau interferometer," U.S. patent US7057738B2 (2003).

21. R. M. Neal and J. C. Wyant, "Polarization phase-shifting point-diffraction interferometer.," Appl. Opt. **45**, 3463–76 (2006).

22. M. Servin, M. Cywiak, and A. Davila, "Extreme shearing interferometry: Theoretical limits with practical consequences," Opt. Express **15**, 17805 (2007).

23. P. Hariharan, *Optical Interferometry*, Second Ed. (Elsevier, 2003).

24. D. Youla, "Generalized Image Restoration by the Method of Alternating Orthogonal Projections," IEEE Trans. Circuits Syst. **25**, 694–702 (1978).

25. C. Falldorf, "Measuring the complex amplitude of wave fields by means of shear interferometry," J. Opt. Soc. Am. A **28**, 1636 (2011).

26. T. Kozacki, K. Falaggis, and M. Kujawinska, "Computation of diffracted fields for the case of high numerical aperture using the angular spectrum method," Appl. Opt. **51**, 7080–7088 (2012).

27. K. Falaggis, T. Kozacki, and M. Kujawinska, "Computation of highly off-axis diffracted fields using the band-limited angular spectrum method with suppressed Gibbs related artifacts," Appl. Opt. **52**, 3288–3297 (2013).

28. M. Guizar-Sicairos, S. T. Thurman, and J. R. Fienup, "Efficient subpixel image registration algorithms," Opt. Lett. **33**, 156 (2008).

CHAPTER 3: (CONFERENCE PROCEEDING) VARIABLE SHEARING HOLOGRAPHY WITH GEOMETRIC PHASE ELEMENTS

Citation

P. Shanmugam, A. Light, A. Turley, K. Falaggis, "Variable shearing holography with geometric phase elements," Proc. SPIE 12223, Interferometry XXI, 122230M (3 October 2022);

doi: 10.1117/12.2634326

Conference

SPIE Optical Engineering + Applications, 2022, San Diego, California, United States

Copyright Permissions

3.1. Introduction

Conventional interferometric and holography methods rely on using a separate reference beam and measuring the deviation in the object wavefield from the reference wavefield. With current capabilities in computational power, it has become more practical to use shear interferometric techniques with optimization algorithms to determine complex wavefields using a series of shear interferograms. Geometric phase elements such as diffractive polarization gratings [1] and geometric phase lenses [2] enable compact common-path shear holographic setups. This paper demonstrates an experimental setup using diffractive polarization gratings to implement shear holography and an alternating projections algorithm to reconstruct the complex wavefield [3]. We discuss the effect of shear selection and aperture effects using information density plots and experimentally demonstrate this effect.

3.2. Shear holography using diffractive polarization gratings

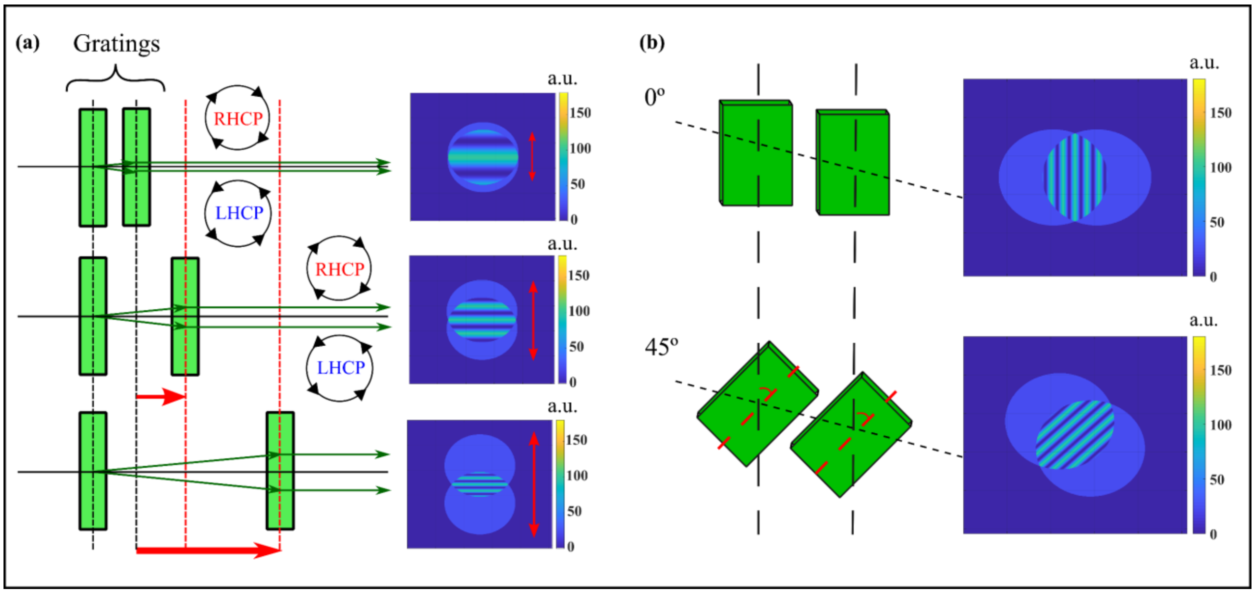

FIGURE 3.1: Effect of grating orientation on shear: (a) axial separation between gratings affect separation between object beams, (b) changing angle of gratings changes the orientation angle of shears

Diffraction polarization gratings are liquid crystal polymers that selectively diffract light based on the polarization state and the diffraction angle conformance with the classical diffraction equation $m\lambda = d \sin(\theta)$. The polarization gratings diffract incoming linearly polarized light into left and right-handed circular polarization lights at positive and negative diffraction angles depending on the polarization state [4]. Using a polarization grating pair enables lateral shear in the spatial domain, and using a linear polarizer in tandem with the gratings enables interference between the sheared beams with geometric phase shifting capabilities. Shears can be varied by adjusting the distance between the gratings or by changing the orientation of the grating pair using a pair of polarization gratings, as shown in Figure 3.1. In this paper, we perform shear holography by changing the angle of the grating pair.

3.3. Alternating Projections for wavefield reconstruction

The grating pair setup creates a copy of the object wavefield and superimposes it on the original object wavefield to produce interference patterns. Recording shear interferograms with different shears provide diversity in the data that allows for reconstructing different spatial frequencies of the object wavefield. If the complex wavefield is denoted as $u(\vec{x})$ then the recorded intensities described as

$$I_\delta(\vec{x}) = \left|u\left(\vec{x} + \overrightarrow{ds}\right)\right|^2 + \left|u\left(\vec{x} - \overrightarrow{ds}\right)\right|^2 + 2\Re\{C(\vec{x}) \exp(-i\delta)\} \tag{3.1}$$

where $\overrightarrow{ds}$ is the shear. The cross-term $C(\vec{x})$ is described as

$$C_n(\vec{x}) = u^*\left(\vec{x} - \overrightarrow{ds}\right) \cdot u\left(\vec{x} + \overrightarrow{ds}\right) = \left(I_0(\vec{x}) - I_\pi(\vec{x})\right) + i\left(I_{\frac{\pi}{2}}(\vec{x}) - I_{\frac{3\pi}{2}}(\vec{x})\right) \tag{3.2}$$

Falldorf et al. [5] demonstrated shear holography using a gradient descent algorithm to reconstruct wavefields for unsymmetrical shear configuration. We have found that that approach cannot be applied to a symmetrical shear configuration. As a result, an alternating projections algorithm was used to reconstruct the wavefield as it does not rely on a gradient function to determine the complex wavefield.

The alternating projections algorithm used in this paper is based on the algorithm developed by Konijnenberg et al. [3]. The algorithm starts with an initial guess and works based on projecting the estimated solution between two constraint equations: measurement constraint and object constraint. This process is summarized in Figure 3.2. After 'n' iterations, the algorithm starts converging to a solution where the deviation in estimated wavefields between the two constraints is below a tolerance limit.

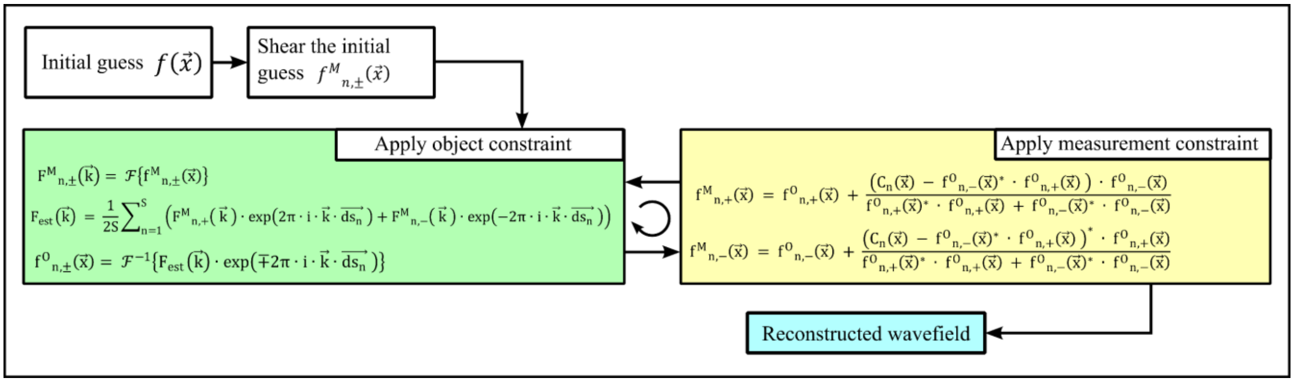

FIGURE 3.2: Principle of the alternating projections algorithm [3].

3.4. Reconstructed results from experiment

The following experiment demonstrates polarization gratings to produce symmetrical shearing and alternating projections algorithm to reconstruct and estimate the object wavefield. A schematic of the experimental setup is shown in Figure 3.3a. The experiment uses a USAF target as the object. The setup comprises two 4f setups with 50 mm lenses. The first 4f setup is placed before the grating pair and ensures the image of the object is in the same plane as aperture 1. Aperture 1 provides spatial boundaries for the reconstruction. The second 4f setup is placed after the grating pair and focuses the image of the object and aperture onto the camera plane. Aperture 2 removes higher-order diffractions from the polarization gratings. The grating pair is placed on a rotational mount, and the different shears are made by rotating the gratings.

For the experiment, the wavelength of the light used was 520 nm. The intensity patterns were recorded using a polarization camera. 24 stereograms were recorded at different grating angular positions (i.e., the shear axis is rotated), and the complex cross-term was evaluated for each shear. To demonstrate that the complex wavefield is being reconstructed here. The reconstruction results are shown in Figures 3.3 (b) and (c). Figure 3.3(b) shows the amplitude map from the reconstruction process and Figure 3.3(c) shows the amplitude map after numerically refocusing the complex wavefield using angular spectrum [6].

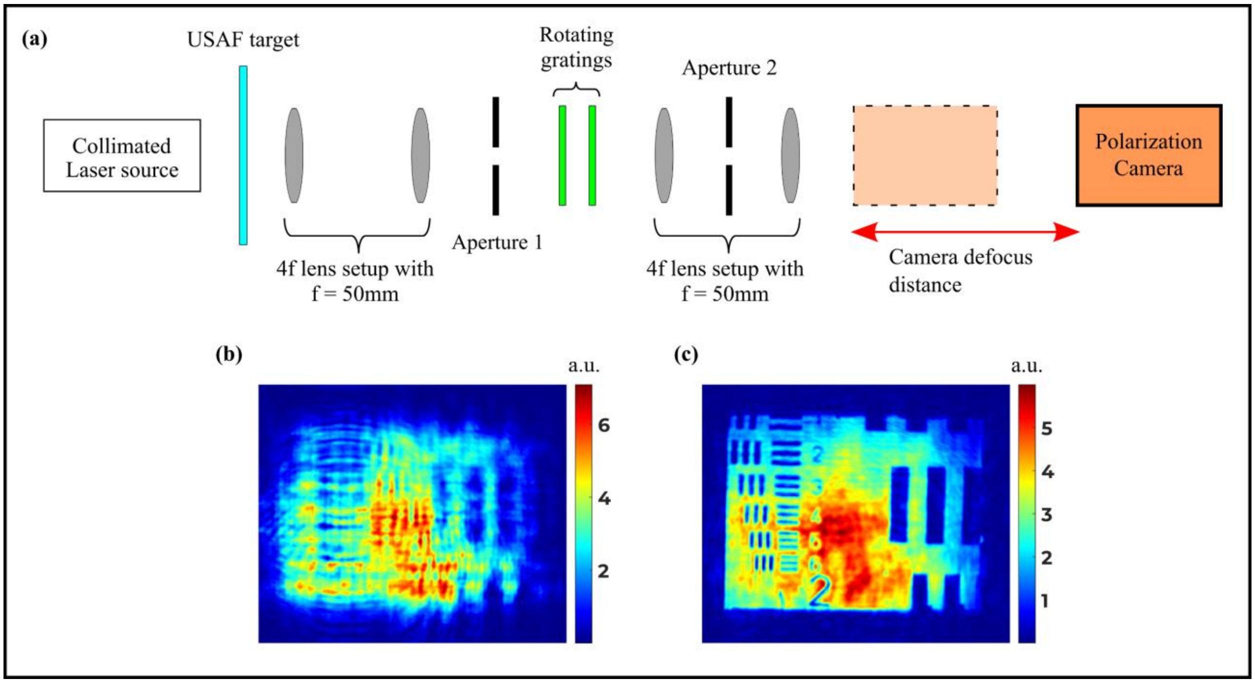

FIGURE 3.3: (a) Experimental configuration; (b) Reconstructed amplitude map of the defocused object; (c) Reconstructed amplitude map after numerical refocusing

3.5. Effect of shear selection and aperture size

Further study was made using information density functions [1,7] to understand the effect of selected shear and aperture size. The effect of aperture size and shear selection is demonstrated in Figure 3.4. When an object beam overlaps with a sheared copy of itself, the interference patterns appear in the overlap regions and provide information to the reconstruction algorithm for the phase component of wavefield estimation. Figure 3.4(a) shows which areas of the beam provide information to the reconstruction algorithm for one shear setting using a circular aperture. Figure 3.4(b) demonstrates the combined effect of 24 shear settings, displaying which areas of the beam provide information to the reconstruction algorithm when the shears are larger than the radius of the aperture. This demonstrates a case where there is no overlap at the center of the beam, and hence no information from that region is provided to the reconstruction algorithm, thus increasing the possibility for the phase reconstruction to fail. An experiment was performed using large shear separation and 24 grating angular positions for a square aperture. The resulting reconstruction results are shown in Figure 3.5 (b) and (c). Figure 3.4(b) shows a complete amplitude map reconstruction with some reconstruction artifacts. Figure 3.5(c) shows a patch of phase information missing at the center of the field of view, and the phase reconstruction is incomplete. Comparing the spatial information density map from Figure 3.5(a) with the reconstructed phase map in Figure 3.5(c) shows that the regions in the spatial information density map with minimum value align with the regions where the reconstruction process failed to reconstruct the phase.

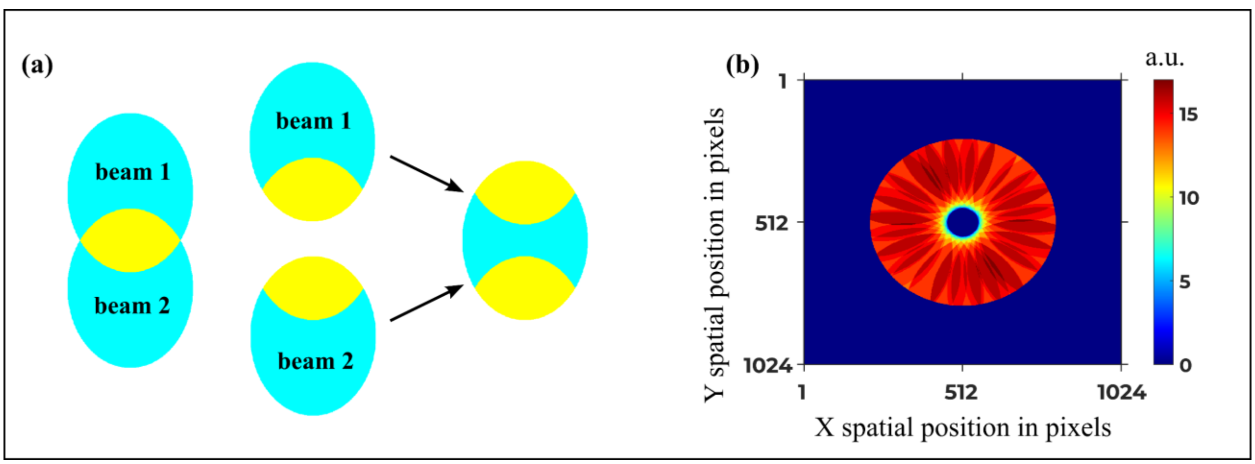

FIGURE 3.4: (a) Spatial information recorded by one shear for a circular aperture; (b) Spatial information density map for 24 shears for large separation distance between gratings that have a fixed shear amount but variable shear axis (24 rotations)

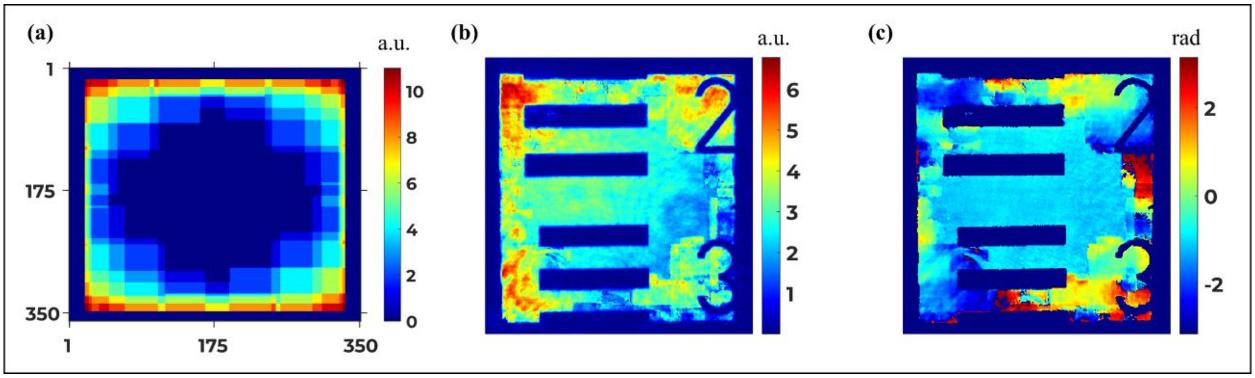

FIGURE 3.5: Experimental demonstration using large shears and square aperture: (a) Spatial information density map demonstrating regions of low value where phase reconstruction can fail; (b) Reconstructed amplitude map; (c) Reconstructed phase map demonstrating failed phase reconstructions in regions with minimum information density values

The result in Figure 3.5 led to a hypothesis that a lack of overlap between the shearing object beams could still produce a successful amplitude reconstruction while the reconstruction of the phase map continued to fail. This hypothesis was verified by separating the gratings by a large distance such that there was no overlap between the object beams in any grating pair angular positions. The results of this experiment were compared with an additional experiment where the gratings were placed close to each other to have large area overlaps, and the intensity maps were recorded at the same grating pair angles. The results are shown in Figure 3.6. To keep the experiment comparable, reconstructions were done using a fixed number of iterations (100 iterations) for both cases.

Figure 3.6(a) shows the information density map for a smaller shear setting (60 pixels shear separation at all angles) where the gratings are placed closed to each other. Figure 3.6(b) shows the information density map for a shear setting with no overlap between the beams in any grating angular positions. Since there is no overlap, the map appears constant at all spatial positions, i.e., spatial information density value = 0 at all spatial positions. Comparing the amplitude maps in Figure 3.6 (b) and (e) show that having no overlap between the object beam can still successfully reconstruct the amplitude map but at the cost of losing the resolution. Comparing the phase maps (Figures 3.6 (c) and (f)) show that having no overlap between the object beams results in no reconstruction of the phase map. Hence, under no overlap conditions, this setup still has the potential to be used as an amplitude imager.

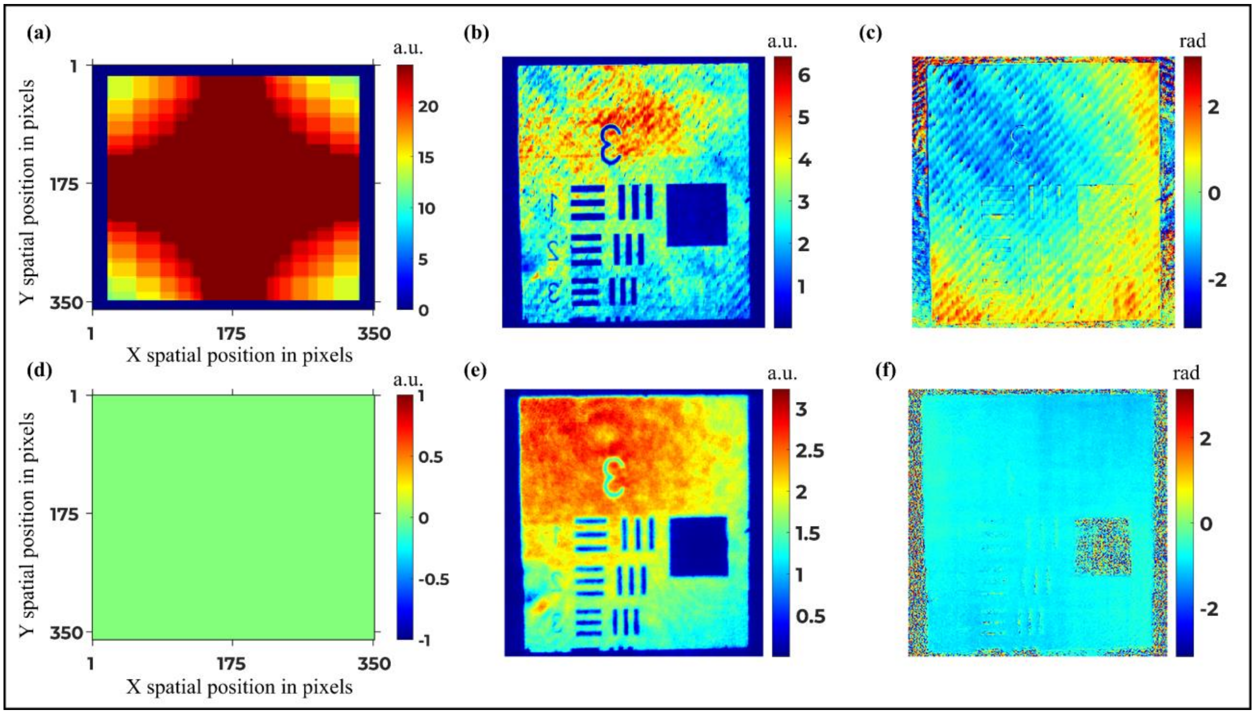

FIGURE 3.6: Reconstructions with large beam overlap (small shear separation, 24 rotations): (a) spatial Information density map, (b) reconstructed amplitude map, (c) reconstructed phase map. For comparison, (d) spatial information density map with no beam overlap, and reconstructions are shown in (e) and (f) for the amplitude and the phase map, respectively.

3.6. Conclusion

This paper shows an experimental demonstration of using diffractive polarization gratings for common-path compact shear holography. We demonstrated a holographic recording by reconstructing a defocused object's complex wavefield. In addition, we demonstrated the effect of selected shears in the reconstruction of amplitude and phase maps. We concluded that the complex cross term from the overlapping regions of the object beam provides information for the phase reconstruction. In cases with no overlap, the reconstruction algorithm is still stable enough to reconstruct the amplitude map, and the system becomes an amplitude imager. The reconstruction process, however, does not produce any phase changes due to a lack of information from having no overlapping regions.

REFERENCES

1. P. Shanmugam, A. Light, A. Turley, and K. Falaggis, "Variable shearing holography with applications to phase imaging and metrology," Light Adv. Manuf. **3**, 1 (2022).

2. K. Choi, J. Yim, and S.-W. Min, "Achromatic phase shifting self-interference incoherent digital holography using linear polarizer and geometric phase lens," Opt. Express **26**, 16212 (2018).

3. A. P. Konijnenberg, A. C. C. de Beurs, G. S. M. Jansen, H. P. Urbach, S. Witte, and W. M. J. Coene, "Phase retrieval algorithms for lensless imaging using diffractive shearing interferometry," J. Opt. Soc. Am. A **37**, 914 (2020).

4. P. Blain, P. Piron, Y. Renotte, and S. Habraken, "An in-line shearography setup based on circular polarization gratings," Opt. Lasers Eng. **51**, 1053–1059 (2013).

5. C. Falldorf, C. von Kopylow, and R. B. Bergmann, "Wave field sensing by means of computational shear interferometry," J. Opt. Soc. Am. A **30**, 1905 (2013).

6. T. Kozacki, K. Falaggis, and M. Kujawinska, "Computation of diffracted fields for the case of high numerical aperture using the angular spectrum method," Appl. Opt. **51**, 7080–7088 (2012).

7. M. Servin, M. Cywiak, and A. Davila, "Extreme shearing interferometry: Theoretical limits with practical consequences," Opt. Express **15**, 17805 (2007).

CHAPTER 4: (PAPER 2) EFFECTIVE SELECTION OF SHEARS IN VARIABLE LATERAL SHEARING HOLOGRAPHY

Authors

Prithiviraj Shanmugam, Konstantinos Falaggis

Publication status

Submitted to Applied Optics. Awaiting reviewer and editorial response.

4.1. Introduction

Interferometry is a common method for the measurement of shape and surface deviations of objects. Although different interferometric systems have different designs [1], most systems use the same principle of generating a known reference wavefield and overlapping it on the object wavefield to produce the interferometric patterns. Modulating one of the wavefields through techniques such as phase shifting methods [2] enable the recovery of three-dimensional information about the object through phase measurements. The same principles can be used for wavefield reconstruction by acquiring both amplitude and phase information of the input wavefields which further extends its applications in the field of wavefront sensing and digital holography [1,3]. The disadvantage of this method is that the system requires producing a well-known wavefield and has high stability and coherency requirements. Shear interferometers enable systems with more relaxed stability requirements that are suitable for harsh environments since they eliminate the need for a reference wave. The general idea of shear interferometer is to create a copy of the input wavefield, also known as object wavefield, then modulate either one or both wavefields by shearing them with respect to each other.

Lateral shear interferometers are systems that split the input wavefield into two and displace one or both beams by a fixed lateral distance. Falldorf et. al. [4,5] demonstrated lateral shearing configuration using a spatial light modulator (SLM) where the first-order diffracted beam from the SLM overlaps with that of the zeroth order to produce the interference patterns. The spatial light modulator also does the phase shifting in this setup. Aleman-Castaneda et. al. [6] implemented a more compact common-path setup shear interferometer with lateral shearing based on geometric phase using a pair of spatially varying axis birefringent plates. Shanmugam et. al. [7] investigated a common-path setup with lateral shearing using diffractive polarization gratings. The phase shifting in this setup was done by geometric phase using a polarization camera.

Radial shear interferometers split the input wavefield into two where the shear is created by resizing each wavefield radially by a different amount. Aleman-Castaneda et. al. [6] showed the presence of interference by using a pair of geometric phase lenses in a common-path design. Choi et. al. [8] investigated wavefront retrieval in an incoherent holographic interferometric system designed using one geometric phase lens. Choi et. al. performed a simultaneous recording of holograms in the red, blue, and green channels and demonstrated wavefront retrieval through a 4-bucket phase shifting method.

Bryngdahl et. al. presented an alternative approach to shearing for studying objects or wavefields that have circular geometries [9]. The authors in [9] present a shear system where the input wavefield is split into two with one wavefield staying constant while the other wavefield is rotated about the optical axis in equal steps using a pair of phase filters. This is an example of an azimuthal shear interferometric system. Longitudinal shear, laterally reversed shear, and radially reversed shear are some examples of other methods found in the literature for shearing input wavefronts in shear interferometric systems [1,9].

In conventional interferometers, the difference in phase between the object wavefield and the reference wavefield forms the interference patterns. So, methods like phase shifting techniques [2] directly evaluate the surface deviations on the object and can recover the wavefront. In shear interferometry, interference occurs due to overlap between different points of the same object wavefield sheared by some known quantity. The difference in the wavefronts at each point of the detector plane can be evaluated using phase-shifting techniques but recovering the object wavefront is still a subject of much interest.

One approach to retrieving the phase is through zonal reconstruction using the least squares approach. Early studies on zonal-based approach were done by Saunders [10] and Rimmer [11] and later improved by several authors for lateral shear configurations. Zou and Rolland [12] showed an improvement in the accuracy of the retrieved wavefield by combining the least squares approach with an iterative process based on Gerchberg-Saxton algorithm. The least squares approach still suffered from low spatial resolution because the sampling intervals of the retrieved wavefront had to be equal to the shear amount. This was solved by Dai et. al. [13] where the authors proposed a new least squares approach combined with Gerchberg-Saxton algorithm and zero padding, to use two orthogonal shears to recover the wavefield. The advantage of this method was that the shears can be selected at arbitrary integral multiple of the wavefield's sampling interval and can still perform wavefield reconstruction at high spatial resolution.

Another approach to retrieving the object wavefield is modal-based phase reconstruction. The performance of this method depends on the choice of the model used for the phase reconstruction and the object being measured. Most optical prescriptions and aberrations in optical systems can be described using the Zernike polynomials. So, models based on Zernike polynomials are a natural choice for measuring optics or for characterizing aberrations in optical systems. Harbers et. al. [14] demonstrated the use of Zernike polynomials-based model to characterize wavefronts measured using lateral shear interferometric systems.

With advances in computational shear interferometry, the use of optimization algorithms for wavefield reconstruction is more prominent for systems that use lateral shear configurations. Falldorf et. al. [4,5,15] studied shear interferometric systems that use a spatial light modulator where one wavefront remains constant while the copied wavefront shears over the constant wavefront. The authors used a gradient descent approach to solve the problem and retrieved the wavefront. Shanmugam et. al. [7,16] studied shear systems that laterally shear both beams symmetrically by using diffractive polarization gratings. The authors used a modified version of Konijnenberg's reconstruction algorithm from [17] which is based on alternating projections algorithm [18]. The major advantage of these techniques is that they do not assume that the shear measurement is related to the surface slope, i.e., no Taylor series approximation have been made in the reconstruction model.

In all the shear configurations, the choice of shears used for the experiments plays an important role in how efficiently the wavefield can be reconstructed. In computational shear interferometry using lateral shear configuration, the choice of shears impacts the surface frequencies that can be reconstructed during wavefield retrieval. Servin et. al. [19] did an extensive study on these effects in symmetrical lateral shearing systems and characterized a filter function that acts as a frequency response transfer function to the selected shear. The authors further investigated the effect of different pupil geometries using single and two orthogonal shears and using support functions that are based on the areas of overlap between the sheared wavefronts. Falldorf defined characteristic transfer functions in [20] for both the amplitude and phase of a wavefield that allows for identifying which frequencies are transmitted during the shear experiments. Inspired by the works presented in [19,20], Shanmugam et. al. investigated the effects of multiple shears in a lateral shear configuration using information density maps and correlated the results with reconstructed wavefields from simulations [7] and from experiments [16]. The authors defined two types of information density maps to characterize the effects of shears on reconstructed wavefields. The frequency information density map maps out the surface frequencies in two orthogonal directions (X and Y) and their relative strengths in their availability to be reconstructed during phase retrieval. The spatial information density map defines the number of times each pixel receives information from the overlapping regions as a result of all the shears used for wavefield reconstruction. None of the previous studies provided a systematic guideline on how to choose the shear amounts for multi-shear reconstruction techniques. At first glance, the shear selection problem resembles the wavelength selection problem often found in multi-wavelength interferometry or the selection of defocus planes in multi-plane phase retrieval problems. However, the aforementioned areas deal with a one-dimensional optimization problem (optimizing a 1D cost function using one parameter), and the shear selection problem presented in this chapter needs to optimize a two-dimensional cost function using two parameters (the shear in x- and y-direction). Failure to obtain an optimum shear selection result in ambiguous measurements where the shear interferometer is not able to measure a series of spatial frequencies.

In this work, we present a systematic shear selection strategy that solves this problem and provides measurements that measure all spatial frequencies that can be captured by the camera detector.

4.2. Symmetric Shearing Configurations

The shearing configurations used for these simulations are based on symmetrical shearing discussed in [7] using geometric polarization gratings. Geometric polarization (GP) gratings, also known as diffractive polarization gratings, are optical elements that diffract light based on its current polarization state. The setup with GP gratings is shown in Figure 4.1. The simulations discussed in this paper use a linearly polarized input wavefield. The first GP grating diffracts the linearly polarized light into right and left-handed circularly polarized light, which are the first-order diffracted beams on either side of the zeroth order respectively. The first-order diffracted circularly polarized beams pass through a second GP grating which corrects the beam angle and makes them parallel to the optical axis. Overall, the setup shown in Figure 4.1 takes an object input wavefield, creates a copy of the wavefield, and symmetrically shears the two object wavefields. The magnitude of shear (fR) is a direct function of the separation between the two gratings (Z_G).

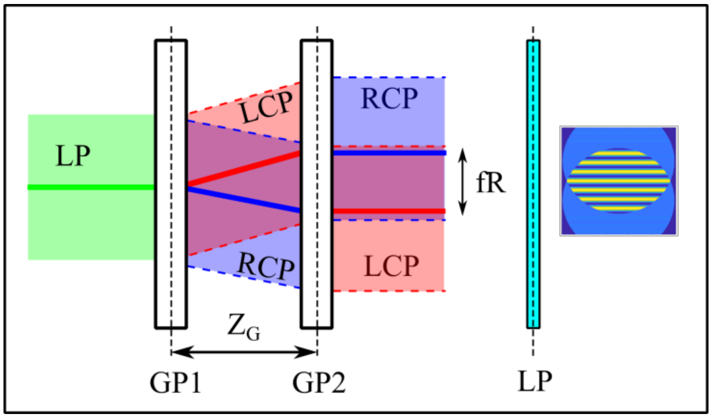

FIGURE 4.1: GP grating setup for lateral shear interferometry

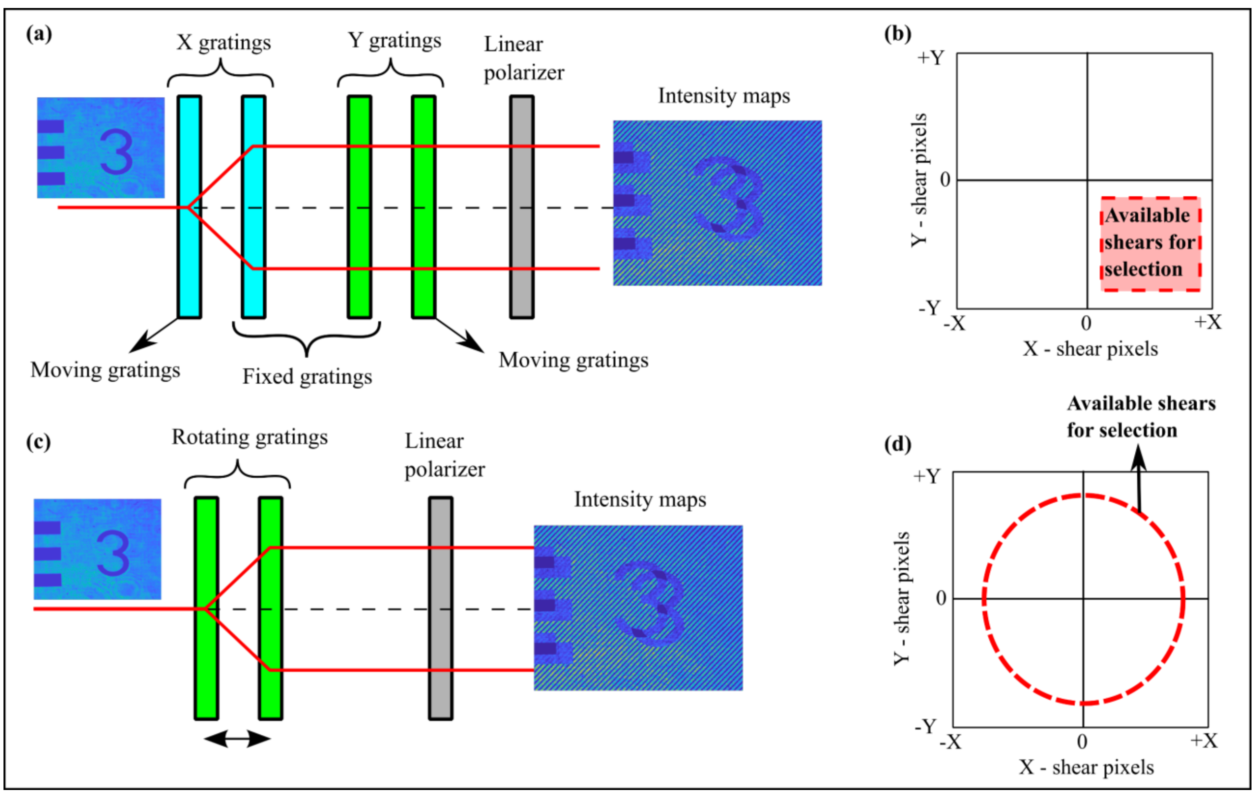

FIGURE 4.2: Experimental setups for lateral shearing: (a) 4-grating setup for XY shear, (b) Available shears in 4-grating setup, (c) 2-grating setup for polar shear, (d) Available shears in 2-grating setup

Based on the experimental setups discussed in [7], two designs are considered for this study.

The first design uses 4 gratings that enable an independent XY shearing system, but the shears are constrained to one quadrant of the shear plane. The second design uses two gratings that rotate together about the optical axis. This makes the setup more compact and enables access to all quadrants on the shear plane. The limitation of the two-grating system is that rotation happens with a fixed shear distance between the object wavefields. The designs are shown in Figure 4.2.

4.3. Need for optimal shears

Each shear when recording the shear interferograms affects the frequencies that are retrieved during the phase reconstruction process. This is demonstrated by simulating phase retrieval of a defocused point source and observing the error maps while using single shears for reconstruction in Figures 4.3a and 4.3b.

The example shown in Figure 4.3a demonstrates that using a shear of 30 pixels in X direction, (i.e.) $S_x = 30\ pixels\ and\ S_y = 0\ pixels$, results in an error map with almost no reconstruction in the vertical direction and incomplete reconstructions that appear at a spacing of 60 pixels in the horizontal direction. The spacing of this periodic error matches the value of $2S_x$ because a shear of 30 pixels would shear both beams symmetrically resulting in a spatial and lateral distance of 60 pixels between the overlapping wavefields. A similar observation is seen in the error map in Figure 4.3b where one shear along a 45-degree angle was used to generate the synthetic interferograms. Based on these observations, it can be concluded that it is plausible to choose a certain combination of shears which can result in longer reconstruction time or incomplete reconstructions. An error map from an incomplete reconstruction is shown in Figure 4.3c which is a consequence of selecting shears that are not capable of retrieving all the frequencies from the input wavefield. This demonstrates the need for optimal shear selection.

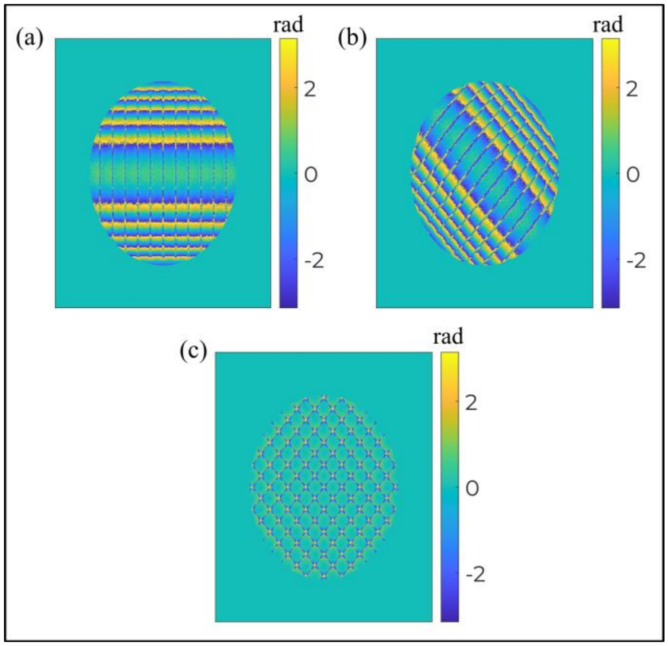

FIGURE 4.3: Error maps demonstrating the effects of shear selection from simulating wavefield reconstruction of a defocused point source: (a) One shear along X-direction, (b) One shear at 45 degrees with respect to X-direction, (c) 4 shears selected along 45, 135, 225 and 315 degrees

4.4. Effect of shear configuration

The effects of shear selection while recording interferograms were previously studied analytically by Falldorf [20] and Servin et. al., [19] and were further explored by studying the combined effect of multiple shears through information density functions by Shanmugam et. al., [7]. The frequency information density function (FIDF) [7], shown in Eq. 4.1, primarily determines which frequencies have a higher potential for being retrieved through phase reconstruction for a given set of shears.

$$FIDF = \sum_{m=1}^{M} \sin^2\left(2\pi \cdot f_x \cdot S_{x,m} \cdot p + 2\pi \cdot f_y \cdot S_{y,m} \cdot p\right) \tag{4.1}$$

where (f_x, f_y) are frequencies in 1/µm in X and Y direction, (S_x, S_y) are the shears in pixels in X and Y direction, p is the spatial resolution in µm, and M is the total number of shear sets used. To understand how the shear configurations discussed in Figure 4.2 affects the phase reconstruction, 256 shear sets were selected from both configurations based on the regions available for shear selection shown in Figures 4.2b and 4.2d. The shear sets were selected such that they formed equispaced points in the area available for shears in configuration 1 and the shear sets in configuration 2 were separated by equal angles across all 4 quadrants. The idea was to characterize the FIDF maps for both configurations using a sufficiently high number of closely spaced points. The results are shown in Figure 4.4.

The 4-grating configuration in Figures 4.4 (b) and (c) shows multiple frequencies at regular intervals that reach near zero values which indicates that the phase reconstruction process would fail in retrieving these frequencies. The values of these failed frequencies are correlated to the spacing between shear points used in Figure 4.4a. Adding random integer noise to the selected shears to perturb periodicity could potentially mitigate this effect but did not prove to be a reliable method as it could also result in reduced frequency information density values resulting in missing frequencies in the reconstructed phase along a 45-degree angle. An example of this effect was discussed in simulations shown in [7]. The results produced by the two-grating system (Figure 4.4e and 4.4f) show consistent retrieval of all frequencies except for the trivial frequency. This comparison shows that the two-grating design is relatively less susceptible to incomplete or failed reconstructions as the FIDF map in Figure 4.4e does not show any pits as a result of this shear selection method.

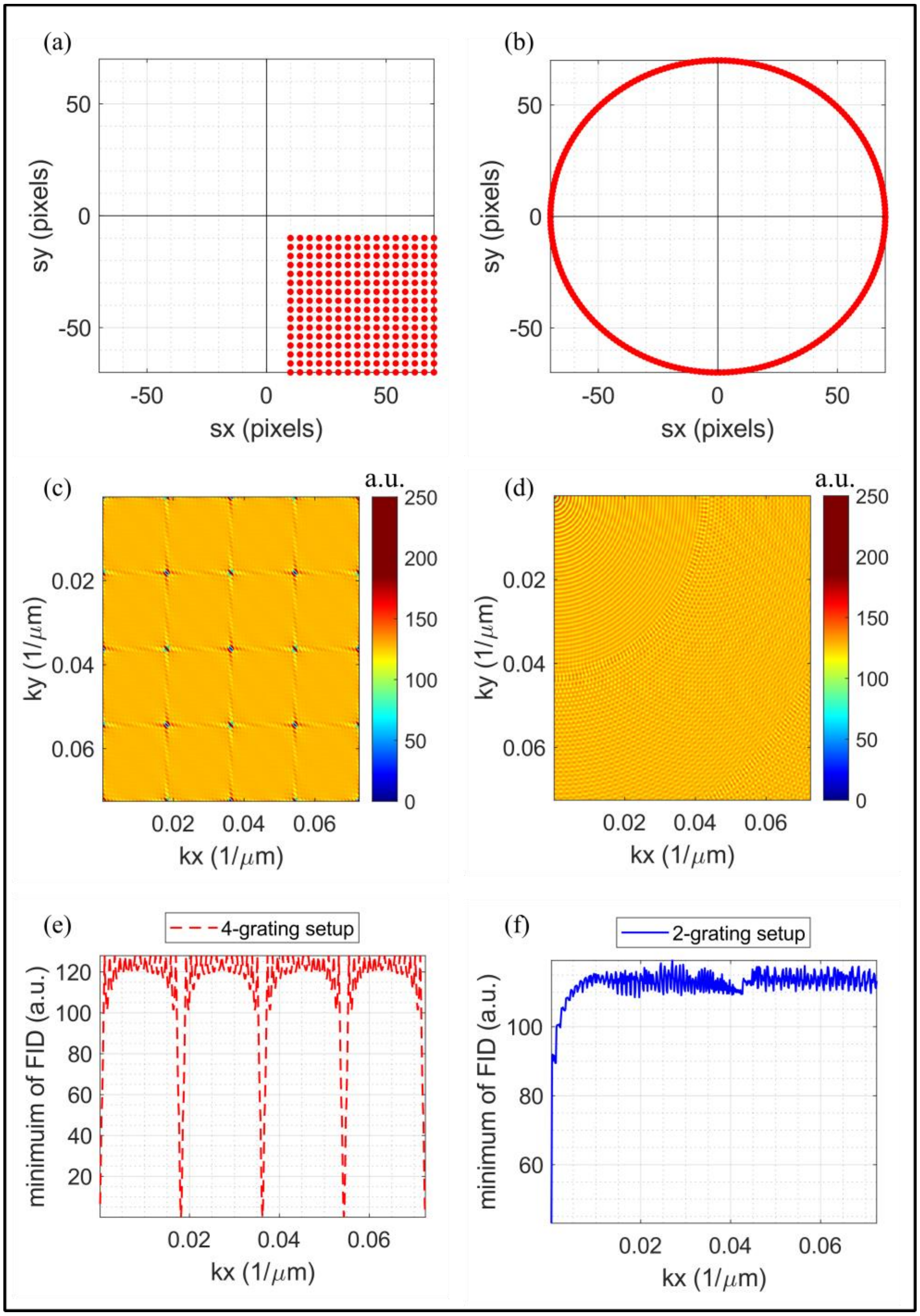

FIGURE 4.4: Systematic shear selection using equal shears on XY and polar configurations: (a) Equal shear spacing in 4-grating configuration, (b) Shears selected with equal angular separation in 2-grating configuration, (c) Frequency information density function (FIDF) map for 4-grating configuration, (d) FIDF map for 2-grating configuration, (e) Minimum FIDF value along X direction for 4-grating configuration, (f) Minimum FIDF value along X direction for 2-grating configuration

4.5. Identification of optimal shear settings: Shear Angle (θ)

Since the optimal design for shear configuration is the two-grating system (Figure 4.2c), shears can be represented using the magnitude of shear (fR) and the angle of shear (θ). So, Eq. 4.1 can be modified as follows.

$$FIDF = \sum_{m=1}^{M} \sin^2\left(2\pi \cdot f_x \cdot S_{x,m} \cdot p + 2\pi \cdot f_y \cdot S_{y,m} \cdot p\right)$$

$$S_{x,m} = fR \cdot \cos(\theta_m)$$

$$S_{y,m} = fR \cdot \sin(\theta_m)$$

$$FIDF = \sum_{m=1}^{M} \sin^2\left(2\pi \cdot f_x \cdot p \cdot fR \cdot \cos(\theta_m) + 2\pi \cdot f_y \cdot p \cdot fR \cdot \sin(\theta_m)\right) \tag{4.2}$$

To identify the optimal shear settings, the effect of three variables in Eq. 4.2 must be explored (i.e.) $fR, \theta_m, and\ M$. For these simulations with M shears, we choose angles (θ) separated by (π/M) to ensure that frequencies from all orientations can be retrieved. To study this effect on the FIDF function, this is incorporated into Eq. 4.2 such that the angle starts from 0 radians and goes up to ((M-1)π/M) radians. So, Eq. 4.2 becomes

$$FIDF = \sum_{m=0}^{M-1} \sin^2\left(2\pi \cdot f_x \cdot p \cdot fR \cdot \cos\left(\frac{m\pi}{M}\right) + 2\pi \cdot f_y \cdot p \cdot fR \cdot \sin\left(\frac{m\pi}{M}\right)\right) \tag{4.3}$$

For the purpose of simplicity to study the effect of using $\theta = \pi/M$, Eq. 4.3 can also be written as

$$FIDF = \sum_{m=0}^{M-1} \sin^2\left(\mathrm{A} \cdot \cos\left(\frac{m\pi}{M}\right) + \mathrm{B} \cdot \sin\left(\frac{m\pi}{M}\right)\right) \tag{4.4}$$

where $A = 2\pi \cdot f_x \cdot p \cdot fR$ and $B = 2\pi \cdot f_y \cdot p \cdot fR$.

To understand the effect of the (pi/M) approach, Eq. 4.4 was studied for “different number of shears” and simplified using Wolfram Mathematica. The results are shown in Table 4.1.

TABLE 4.1. FIDF function for different number of shears M

M	FIDF
4	$\frac{1}{2}(4 - \mathrm{Cos}[2A] - \mathrm{Cos}[2B] - 2\mathrm{Cos}[\sqrt{2}A]\mathrm{Cos}[\sqrt{2}B])$
6	$\frac{1}{2}(6 - \mathrm{Cos}[B](2\mathrm{Cos}[\sqrt{3}A] + \mathrm{Cos}[B]) - \mathrm{Cos}[A](\mathrm{Cos}[A] + 2\mathrm{Cos}[\sqrt{3}B]) + \mathrm{Sin}[A]^2 + \mathrm{Sin}[B]^2)$
7	$\frac{1}{2}(7 - \mathrm{Cos}[2A] - \mathrm{Cos}[2B\mathrm{Cos}[\frac{\pi}{14}] - 2A\mathrm{Sin}[\frac{\pi}{14}]] - \mathrm{Cos}[2(B\mathrm{Cos}[\frac{\pi}{14}] + A\mathrm{Sin}[\frac{\pi}{14}])] - \mathrm{Cos}[2A\mathrm{Cos}[\frac{\pi}{7}] - 2B\mathrm{Sin}[\frac{\pi}{7}]] - \mathrm{Cos}[2(A\mathrm{Cos}[\frac{\pi}{7}] + B\mathrm{Sin}[\frac{\pi}{7}])] - \mathrm{Cos}[2B\mathrm{Cos}[\frac{3\pi}{14}] - 2A\mathrm{Sin}[\frac{3\pi}{14}]] - \mathrm{Cos}[2(B\mathrm{Cos}[\frac{3\pi}{14}] + A\mathrm{Sin}[\frac{3\pi}{14}])])$
12	$\frac{1}{2}(12 - \mathrm{Cos}[B](2\mathrm{Cos}[\sqrt{3}A] + \mathrm{Cos}[B]) - 2\mathrm{Cos}[\sqrt{2}A]\mathrm{Cos}[\sqrt{2}B] - \mathrm{Cos}[A](\mathrm{Cos}[A] + 2\mathrm{Cos}[\sqrt{3}B]) - 2\mathrm{Cos}[\sqrt{2+\sqrt{3}}A]\mathrm{Cos}[\sqrt{2-\sqrt{3}}B] - 2\mathrm{Cos}[\sqrt{2-\sqrt{3}}A]\mathrm{Cos}[\sqrt{2+\sqrt{3}}B] + \mathrm{Sin}[A]^2 + \mathrm{Sin}[B]^2)$

Table 4.1 shows that through this approach, the terms A and B are split between multiple cosine and sine terms enabling efficient retrieval of frequencies for phase reconstruction with FIDF values always greater than zero for all frequencies. The only frequency when FIDF becomes zero is at the trivial frequency (i.e.) $f_x = 0\ \mu m^{-1}\ and\ f_y = 0\ \mu m^{-1}$. Also, with an increased number of shears, more Cosine terms appear with the constants A and B appear as multiplied with irrational numbers making it less probable for FIDF to reach zero value. This shows that the π/M approach is an efficient method for selecting values for shear angle (θ).

4.6. Identification of optimal shear settings: Shear Magnitude (fR) and number of shears (N)

The magnitude of shear fR is directly correlated with the distance (Z_G) between the two GP gratings used in the polar configuration as shown in Figures 4.1 and 4.2. The lowest value of fR is limited by the physical constraint on how close the gratings can be spaced in the physical setup. The thickness of each grating is 0.45 mm, and the gratings are placed in the setup by fixing them to cage plates using thin tapes. For the purpose of simulations, the smallest value fR can reach is assumed to be 10 pixels. The upper limit for fR is provided by the spatial information density function (SIDF) which was defined in [7]. The spatial information density function is a map that shows the summation of overlaps from all shear settings in the field of view of object wavefield when recording the interferograms. Areas with a larger number of overlaps lead to faster reconstruction. Two observations were made in [16] relating to spatial information density function maps when the shear settings produced regions of zero overlap in the field of view of the object wavefield. The first observation was that, while there were no overlaps in the object beams, the reconstruction algorithm was still able to reconstruct the amplitude map. The second observation was, due to lack of overlaps between the object beams to produce interference, no phase information was reconstructed in regions of zero overlap. This leads to the conclusion that the upper limit for fR is the maximum value of fR before regions of zero overlap show up in spatial information density map. For a circular aperture of radius ‘a’, the upper limit for fR would be ‘a/2’. The aperture radius used for these simulations is 350 pixels.

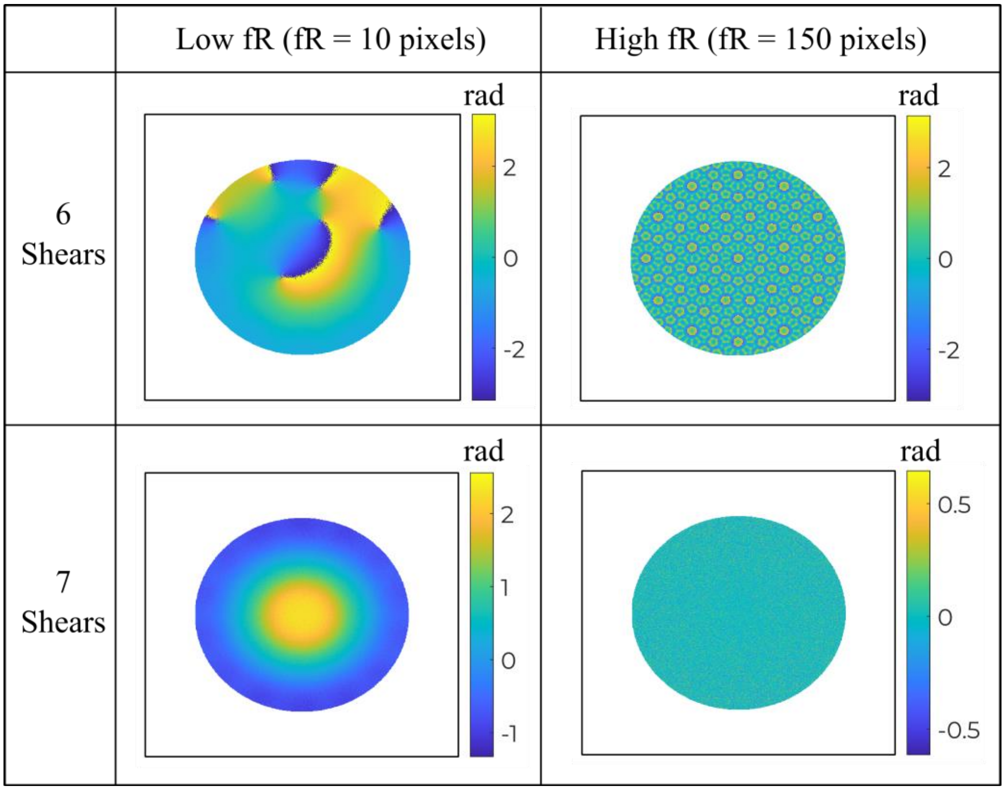

FIGURE 4.5: Effects of low and high values of fR on phase reconstruction

Figure 4.5 shows error maps from phase reconstruction demonstrating the different effects of fR on phase maps when its value is closer to either maximum or minimum limit. This is demonstrated using 6 and 7-shear sets. At low values of fR, the nature of errors in phase is of low frequencies. At fR = 10 pixels for 7 shears, the error map in Figure 4.5 shows a spherical error in the reconstructed phase. At 6 shears, the error maps show the presence of vortex pairs at fR = 10 pixels. At higher fR (i.e., fR = 150 pixels), the errors produced in phase reconstruction are high frequencies in nature. These high-frequency errors either occur in the form of high-frequency noise (see Figure 4.5 for 7 shears and fR 150 pixels) or in the form of structured errors (see Figure 4.5 for 6 shears and fR 150 pixels). So, the optimal value or range for fR must be identified for ideal reconstruction.

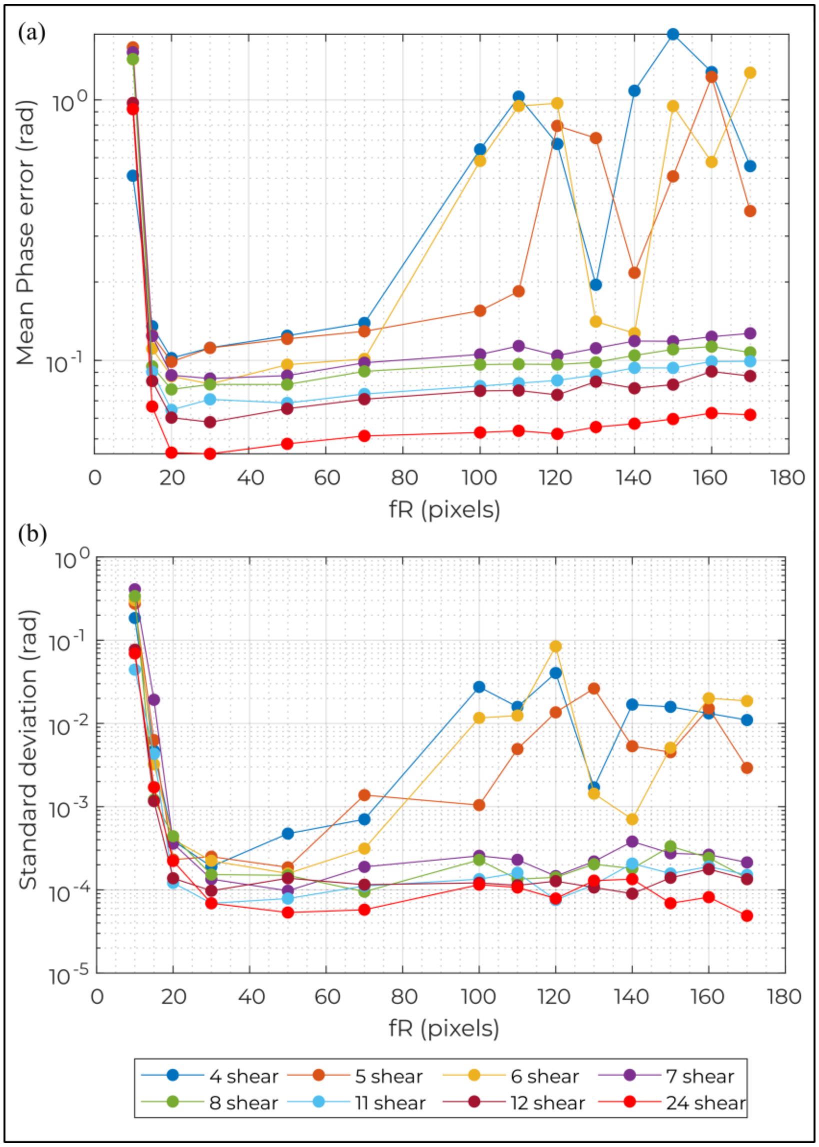

FIGURE 4.6: Simulation data (7 experiments per parameter set): (a) fR vs mean phase error, (b) fR vs standard deviation of phase errors

The optimal range for magnitude of shear 'fR' and number of shears 'M' for ideal reconstruction was identified through an empirical approach. Phase reconstruction simulations were performed using 14 different shear magnitudes ‘fR’ ranging from 10 pixels to 170 pixels for 4, 5, 6, 7, 8, 11, 12 and 24 shears. The synthetic intensity maps generated for these simulations have a random noise factor added to it with an amplitude equal to 20% of maximum intensity value. To account for the variability caused by this noise, the simulations were repeated 7 times and the standard deviations were also evaluated. The phase reconstructions were performed using a 3-layer multiresolution method [21]. The phase reconstruction algorithm used for the simulations is an alternating projections algorithm and more details about the algorithm can be found in [7]. Figure 4.6 shows the mean and standard deviations produced from these simulations.

The mean phase error plots in Figure 4.6a and standard deviation plots in Figure 4.6b show that low values of fR (i.e., fR < 20 pixels) produce high phase errors with high standard deviations. With an increase in the number of shears, it can be observed that the mean phase error decreases. In addition, it can also be observed that the standard deviation values also go down. The mean phase error is relatively low for fR values between 20 and 70 pixels for all shears. For 4, 5, and 6 shears, the mean phase errors for fR greater than 70 pixels are sporadic and high, while for 7, 8, 11, 12, and 24 shears the phase errors do not significantly change for the same values of fR. A similar effect can also be observed in the standard deviation plot in Figure 4.6b. The standard deviation plot demonstrates that the phase reconstruction is more sensitive to the intensity noise and less repeatable for 4, 5, and 6 shears for high values of fR (i.e., fR > 70pixels) and at low values of fR (i.e., fR < 20 pixels). Comparing Figures 4.6a and 4.6b, the following conclusions can be made: (i) Phase reconstruction using 7 or more shears with fR between 20 and 70 pixels is optimal for ideal reconstruction, (ii) An increase in the number of shears decides the lowest error that can be achieved from the phase retrieval process. To better understand the influence of the parameters, the magnitude of shear (fR) and the number of shears (M), the data from simulations were used to evaluate the signal-to-noise ratio for both parameters using Minitab. For this purpose, the simulation data were assumed as custom Taguchi design and the output settings were set to ‘smaller is better’. This makes the software use Eq. 4.5 for evaluating the signal-to-noise ratio.

$$S/N\,ratio = -10 \times \log_{10}(\sum(Y^2)\,/n) \tag{4.5}$$

Where Y = output (i.e., phase error) and n is the number of repetitions. The signal-to-noise ratio was calculated for each parameter set and the mean signal-to-noise ratio was estimated for each value of ‘fR’ and ‘M’. The signal-to-noise ratios for both parameters is plotted in Figure 4.7.

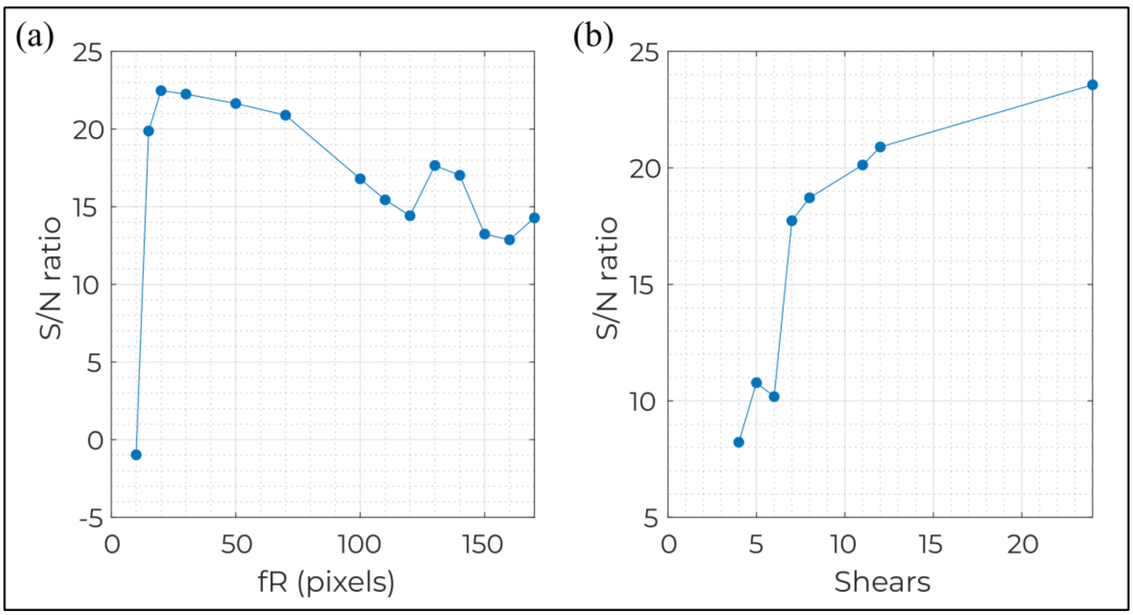

FIGURE 4.7: Signal to noise ratio plot: (a) S/N ratio vs fR , (b) S/N ratio vs number of shears

The plots in Figure 4.7 agree with the conclusions previously derived from Figure 4.6. From both, Figures 4.6 and 4.7, it can be concluded that the magnitude of shear parameter is more robust and produces less phase errors when the value is between 20 and 70 pixels. Also, the significant shift in the signal-to-noise ratio of the number of shears parameter between 6 and 7 shears show that the use of 4, 5 and 6 shears is not reliable, and a minimum of 7 shears should be used to get consistent results with less phase error values. Based on the observations from Figures 4.6 and 4.7, it can be concluded that the optimal setting for the ideal reconstruction of the phase map is to have fR between 20 and 70 pixels with 7 or more shear sets.

4.7. Frequency information density function (FIDF)

To understand how these simulations were influenced by the frequency information density function, the FIDF maps were generated for all simulation parameters. A few example FIDF maps for 4, 6, 7, and 12 shears at shear magnitudes 10, 30, and 150 pixels are shown in Figure 4.8.

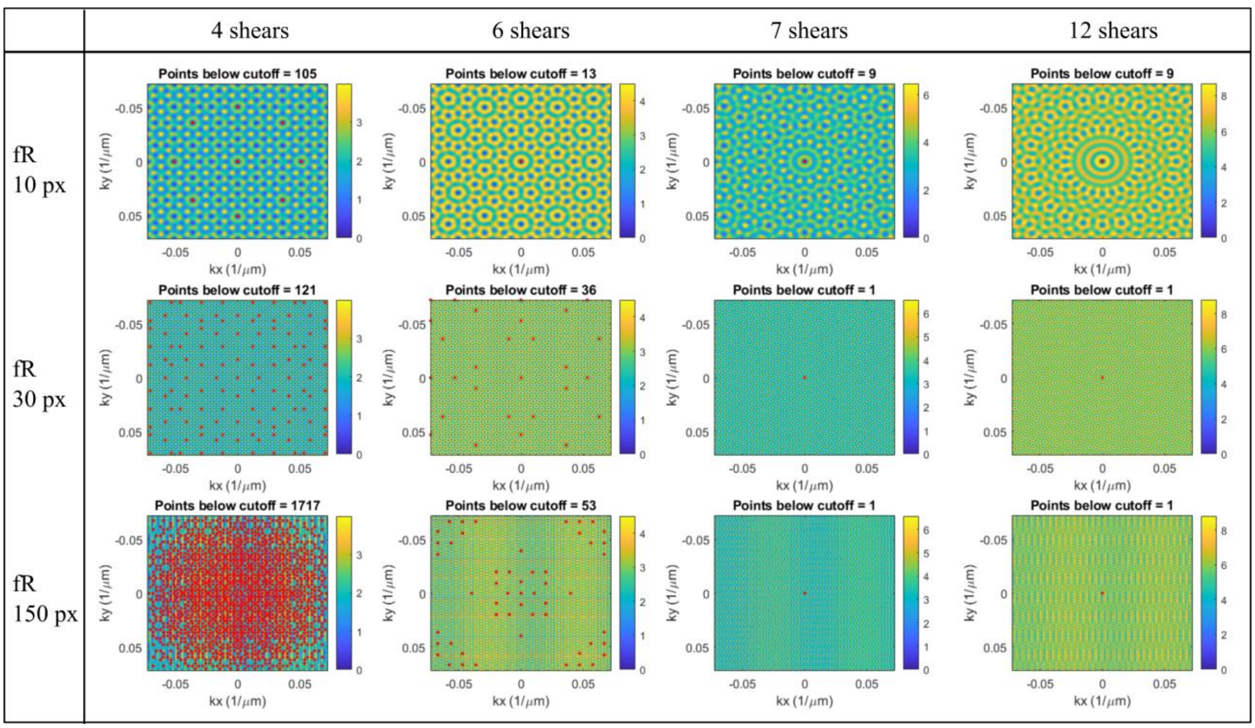

FIGURE 4.8: Frequency information density maps for different shears at low and high fR values

All the observations made in previous sections can be linked to the frequency information density function. The FIDF map shows the distribution of frequencies demonstrating which frequencies can be easily retrieved during the phase reconstruction process. To understand and identify frequencies that could potentially have problems being retrieved during phase reconstruction, a cutoff of 0.05 was set up to identify those points. These frequencies are marked with red dots in Figure 4.8. The FIDF maps in Figure 4.8 show that a very low value of fR (i.e., fR = 10) has more frequencies below the cutoff than fR around 30 pixels. A low number of shears leads to more frequencies below the cutoff. For example, at fR = 30 pixels, 6 shears have fewer points below the cutoff than 4 shears. The number of frequency sets that fail the cutoff is significantly higher at high fR (i.e., fR = 150 pixels) for a low number of shears. In general, a shear-magnitude of fR 30 and 150 pixels shows good potential for retrieving the frequencies provided the number of shears is a minimum of 7. To get a more comprehensive idea, the number of frequencies that are below the cutoff were identified for all simulation parameters and plotted against fR for all shears in Figure 4.9. Figure 4.9 shows similar characteristics to the observations made in Figure 4.6. 4, 5, and 6 shears show that there are more frequencies with FIDF values below the cutoff for all values of fR, thus making it not suitable for efficient phase retrieval.

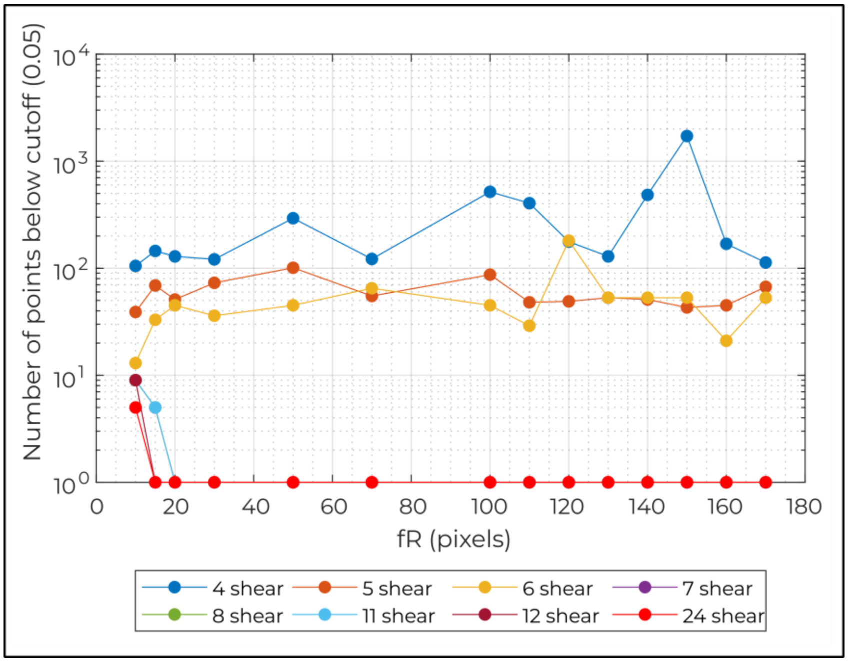

FIGURE 4.9: fR vs number of points below cutoff (0.05) at different number of shears

4.8. Conclusion

Two shearing designs were studied for identifying the optimal set of parameters to identify the ideal shear settings. Through a preliminary simulation using a sufficiently large number of shear sets, the downfall of the 4-gratings arrangement. It was concluded the two-grating arrangement was the best option for optimal reconstruction. For the two-grating arrangement, a π/M approach was adopted where the gratings were rotated together at equal angles to acquire the interferograms. The other parameters that needed to be optimized were the shear-magnitude 'fR' and number of shears 'M'. This was done using an empirical approach through simulations with synthetic intensity maps. The synthetic intensity maps were generated with a noise of amplitude 20% of maximum intensity and the phase maps were reconstructed using alternating projections algorithm. By studying the results of these simulations, it was identified that optimal settings for fR are between 20 and 70 pixels and a minimum of 7 shears should be used for ideal reconstruction. The number of shears affects the lowest error that can be achieved and has an inverse relation between them. For the settings used in the simulations, the best results were obtained for fR = 20 and 30 pixels at 24 shears and the mean phase error was 0.0442 and 0.0438 radians respectively with their corresponding standard deviations being 0.0002 and 0.0001 radians for 7 simulations. The paper concludes by comparing the results to the frequency information density function for the same simulation settings and analyzing the correlation between the observed phase errors and the behavior of the FIDF maps.

REFERENCES

1. D. Malacara, ed., *Optical Shop Testing* (John Wiley & Sons, Inc., 2007).

2. Y. Surrel, "Design of algorithms for phase measurements by the use of phase stepping," Appl. Opt. **35**, 51 (1996).

3. T.-C. Poon, ed., *Digital Holography and Three-Dimensional Display* (Springer US, 2006), Vol. 148.

4. C. Falldorf, C. von Kopylow, and R. B. Bergmann, "Wave field sensing by means of computational shear interferometry," J. Opt. Soc. Am. A **30**, 1905 (2013).

5. C. Falldorf, M. Agour, and R. B. Bergmann, "Digital holography and quantitative phase contrast imaging using computational shear interferometry," Opt. Eng. **54**, 024110 (2015).

6. L. A. Alemán-Castaneda, B. Piccirillo, E. Santamato, L. Marrucci, and M. A. Alonso, "Shearing interferometry via geometric phase," Optica **6**, 396 (2019).

7. P. Shanmugam, A. Light, A. Turley, and K. Falaggis, "Variable shearing holography with applications to phase imaging and metrology," Light Adv. Manuf. **3**, 1 (2022).

8. K. Choi, J. Yim, and S.-W. Min, "Achromatic phase shifting self-interference incoherent digital holography using linear polarizer and geometric phase lens," Opt. Express **26**, 16212 (2018).

9. O. Bryngdahl and W.-H. Lee, "Shearing interferometry in polar coordinates," J. Opt. Soc. Am. **64**, 1606 (1974).

10. J. B. Saunders, "Measurement of wave fronts without a Reference Standard: Part 1. The wave-front-shearing interferometer," J. Res. Natl. Bur. Stand. Sect. B Math. Math. Phys. **65B**, 239 (1961).

11. M. P. Rimmer, "Method for Evaluating Lateral Shearing Interferograms," Appl. Opt. **13**, 623 (1974).

12. W. Zou and J. P. Rolland, "Iterative zonal wave-front estimation algorithm for optical testing with general-shaped pupils," J. Opt. Soc. Am. A **22**, 938 (2005).

13. F. Dai, F. Tang, X. Wang, and O. Sasaki, "Generalized zonal wavefront reconstruction for high spatial resolution in lateral shearing interferometry," J. Opt. Soc. Am. A **29**, 2038 (2012).

14. G. Harbers, P. J. Kunst, and G. W. R. Leibbrandt, "Analysis of lateral shearing interferograms by use of Zernike polynomials," Appl. Opt. **35**, 6162 (1996).

15. C. Falldorf, M. Agour, and R. B. Bergmann, "Advanced wave field sensing using computational shear interferometry," Interferom. XVII Adv. Appl. **9204**, 92040C (2014).

16. P. Shanmugam, A. Light, A. Turley, and K. Falaggis, "Variable shearing holography with geometric phase elements," in *Interferometry XXI*, M. B. North-Morris, K. Creath, and R. Porras-Aguilar, eds. (SPIE, 2022), p. 21.

17. A. P. Konijnenberg, A. C. C. de Beurs, G. S. M. Jansen, H. P. Urbach, S. Witte, and W. M. J. Coene, "Phase retrieval algorithms for lensless imaging using diffractive shearing interferometry," J. Opt. Soc. Am. A **37**, 914 (2020).

18. D. Youla, "Generalized Image Restoration by the Method of Alternating Orthogonal Projections," IEEE Trans. Circuits Syst. **25**, 694–702 (1978).

19. M. Servin, M. Cywiak, and A. Davila, "Extreme shearing interferometry: Theoretical limits with practical consequences," Opt. Express **15**, 17805 (2007).

20. C. Falldorf, "Measuring the complex amplitude of wave fields by means of shear interferometry," J. Opt. Soc. Am. A **28**, 1636 (2011).

21. K. Falaggis, T. Kozacki, and M. Kujawinska, "Accelerated single-beam wavefront reconstruction techniques based on relaxation and multiresolution strategies," Opt. Lett. **38**, 1660 (2013).

CHAPTER 5: (PAPER 3) SUB-MILLIMETER FRINGE PROJECTION PROFILOMETRY AT METER-SCALE FIELD OF VIEWS

Authors

Prithiviraj Shanmugam, Konstantinos Falaggis

Publication status

Submitted to Applied Optics. Awaiting reviewer and editorial response.

5.1. Introduction

Advancements in tactile and optical approaches to performing three-dimensional measurements of complex surfaces are gaining interest to researchers and industries. Most tactile approaches, such as profilometry for surface roughness measurements and coordinate measuring machines (CMM) [1–4] for small-to-large scale form measurements, have a common limitation of having large measurement times. Optical measuring instruments such as interferometry and confocal microscopes are more common for commercial applications. Optical approaches leverage the advantages inherent to their working principles to offer improved accuracy while achieving relatively high measurement speeds [5]. Most interferometric system relies on generating a reference wavefield and overlapping with the object wavefield to produce interference patterns. The surface height map can be retrieved with well-established phase shifting techniques with constant phase shifts [6] or variable phase shifts [7,8] between successive frames. Most phase-shifting interferometric techniques are limited to measuring smooth surfaces and often have high coherency and mechanical stability requirements [9]. Solutions such as shear interferometry [10,11] exist to perform phase measurements with systems with low coherency requirements while more robust to environmental effects. The most common interferometric option for diffused surfaces is white light interferometry based on coherence scanning [12,13], and other options include incoherent digital holography methods [14]. However, these systems are still limited to small fields of view.

Structured Light Illumination (SLI) systems [15–17] play a significant role in 3D surface measurements across various technological and scientific domains. These systems are valued for their simplicity, as they project one or more illumination patterns onto an object and capture the resulting distorted patterns with a camera. The information in these measurement frames is then used to determine the object's shape. Several projection patterns can be utilized for this purpose. Sinusoidal SLI systems [15,16] uses a series of phase-shifted sinusoidal patterns, and the measured intensities are processed using a temporal phase-shifting algorithm [18] to generate the phase map, which reveals the surface information. However, unlike some coherent measurement techniques [19,20], sinusoidal SLI introduces an ambiguity in the phase, necessitating phase unwrapping to achieve accurate absolute shape measurements [21–26]. Various techniques have been employed for this purpose, using either a multi-frequency approach [27–30], or binary and grey-level coding [31,32].

A major disadvantage of digital light projector (DLP) based techniques is the limited depth of focus and the pixel count. Both limited the size of the smallest fringe period, especially when projecting onto a tilted plane. Systems that overcome this problem exist but have a significantly higher complexity [33]. However, in general producing sinusoidal fringe patterns with high contrast and implementing methods for accurate phase shifting is often challenging in fringe projection systems. A common method is project gratings using incoherent light sources, which often suffer from fringe visibility, uniform irradiance, and distortions due to imperfections in gratings [34].

An alternative approach that can mitigate most of these limitations is using coherent and collimated light sources to produce interference patterns between two planer wavefronts [35]. This produces high-contrast fringes, but the system is more prone to errors from vibrations and speckles from rough surfaces. According to [34,36], a good fringe projection system should have the following characteristics: good quality fringes with high contrast over large height variations, less sensitivity to vibrations, flexibility to adapt to different object sizes, and easy, consistent, and accurate phase shifting methods.

Oreb and Dorsch [34] proposed a method with Talbot self-imaging using a sinusoidal grating with phase-shifting capabilities that are introduced by laterally moving the grating. The Talbot image created in [34] averages out imperfections in the grating and produces sinusoidal fringes with better quality and contrast. Stoykova et. al. also conducted a similar study [37], where the authors produced sinusoidal fringes through coherent illumination of sinusoidal gratings. The authors studied the visibility and effect of higher-order diffractions at different wavelengths in the Fresnel zone. The optimal plane to have the best fringe contrast was identified at different wavelengths.

One method explored by Yoneyama et. al. [35] was designed specifically to measure objects moving at a constant speed while fringes were projected onto the object. With the object moving at a constant speed and the camera recording the deformed fringe patterns, the constant spatial offset of the moving object between the recorded intensity maps automatically provides the constant phase shift without additional mechanisms. This makes the system more suitable for analyzing discrete and continuous components in manufacturing industries. The authors studied this experimentally by producing fringe patterns with a Michelson interferometry system and projecting them on a moving object. The velocity of the moving object was evaluated based on fringe characteristics and the frame rate of the camera used for recording. Quan et al. [38] proposed an alternative and unconventional phase-shifting approach of using only two phase shifts with an increment of π. The experiment was conducted by projecting the fringes using an LCD projector, enabling phase-shifting capabilities. The results of this method were compared with that of a conventional 4-step phase shifting method, and a discrepancy of 4.2% was observed. Another phase-shifting method explored by Wu et. al. [39] was through frequency modulation of a single-mode laser diode. The frequency modulation was done by modulating the injection current. This system offers the advantage that no moving parts are involved in producing the phase shifts. This makes the system mechanically stable, but modulating the frequency causes changes in the power, which introduces more errors when recovering the phase through phase shifting techniques. The authors propose a 10-step phase-shifting algorithm to make the system more robust to these power changes and also errors from phase shifting. Moreau et. al. [36] investigated an interferometric fringe projection system where the fringes were produced by splitting the input light into two orthogonal polarization states using a prism with Bragg grating and combining them after passing through a linear polarizer. A phase retarder is used to control the phase shifts between the interfering beams. The spatial shearing introduced between the interfering beams affects the fringe spacing. This shearing is introduced by a glass substrate fixed to the side of the prism along with the grating. Although patterns with multiple fringe-spacings are possible, they are limited to discrete values depending on the geometry of the glass substrate attached to the prism. However, more flexibility is needed to select optimum fringe periods [30].

It should be noted, that although adjustable fringe periods can be achieved using an interferometric fiber-optic fringe projection system [39] the system stability if limited by the environmental vibrations.

Creating stable fringes has highest priority. For instance, Sánchez et. al. [40] reported a stable fringe projector based on a common-path Gates interferometer, but the fringe period is not adjustable, nor the fringes cannot be rotated. This does not allow unwrapping the phase using either a multi-frequency approach [31] or a technique that rotates the fringes [27].

In this paper, we explore the use of geometric phase gratings for interferometric fringe projection systems. The system is designed to be common-path which makes the fringe pattern more stable to any environmental effects. The study is based on a coherent laser source which ensures high fringe contrast and extremely high depth of focus. The gratings enable polarization splitting and lateral shearing, and the beams travel along a common path through a linear polarizer and interfere. Rotating the linear polarizer enables polarization phase shifting. In this paper, the phase recovery is done using the Fourier transform method [41] and the results are discussed. The paper concludes by demonstrating the flexibility of the system to do a fringe projection on objects with a wide range of sizes and the ability of the system to produce fine sub-millimeter fringe spacing to perform measurements with high resolution. The system has the advantage of producing fringes that are not limited by the grating parameters or projector parameters and are only limited by the pixel size of the camera to resolve the fringes.

5.2. Realization of Fringe projection system using GP gratings

Geometric phase gratings [42], also known as, polarization gratings, are thin optical gratings that selectively diffract light based on the polarization state of the incoming light. For linear polarized light, those gratings convert an incoming beam into two beams of equal intensity that are left and right circular polarized but diffracted at distinct angles. Based on these properties, a pair of GP gratings can be used to realize an interferometric holography system with lateral shearing and phase-shifting capabilities. This was previously demonstrated in [11] and [43] which used an alternating projections algorithm to perform wavefield reconstruction. In this paper, we demonstrate the use of a GP grating pair as a fringe projection system. Figure 5.1 shows how a fringe projection system can be realized using a GP grating pair.

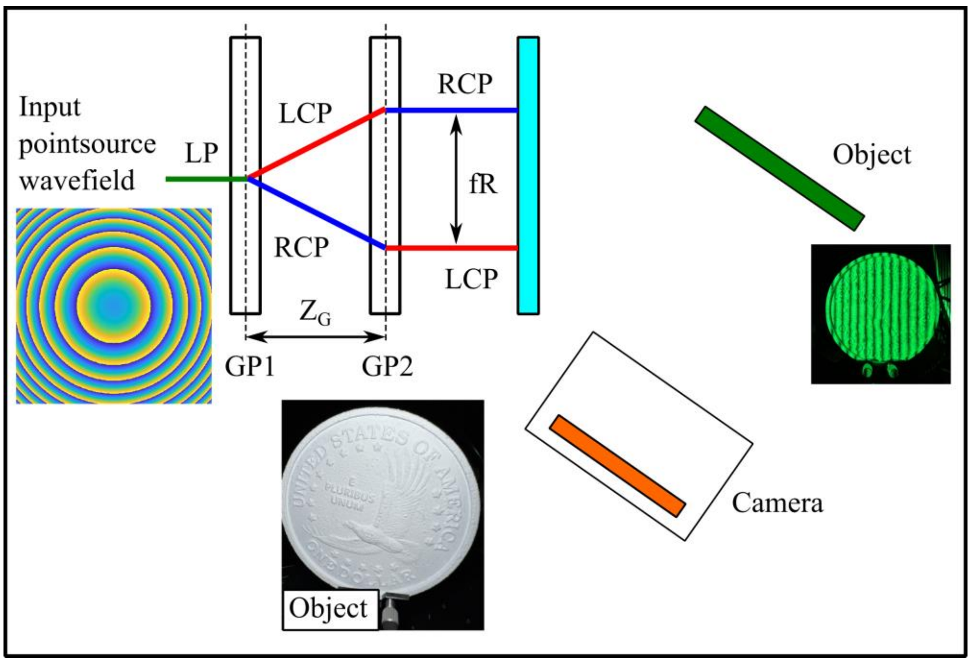

FIGURE 5.1: Realization of a fringe projection system using GP gratings

For the fringe projection system, the GP grating pairs use a linearly polarized point source as the input. The first grating splits the input light into left and right circular polarized in two equal and opposite directions. The second grating corrects for this angle and makes the wavefronts parallel. After the beams pass through a linear polarizer, both beams are in the same state of linear polarization and interfere.

Consider an arbitrary wavefield $U(x, y)$ that is Fourier transformed by a lens of focal length F. At the Fourier plane, the Fourier transform of the wavefield is given as $U(f_x, f_y)$, where $f_x = \frac{x}{\lambda F}$ and $f_y = \frac{y}{\lambda F}$. When placing a pair of GP gratings at the Fourier plane, two beams are generated which can be expressed as

$$U_1 = \frac{1}{\sqrt{2}} U(f_x - f_0, f_y) \tag{5.1}$$

and

$$U_2 = \frac{1}{\sqrt{2}} U(f_x + f_0, f_y) \tag{5.2}$$

where $f_0 = \frac{s}{\lambda F}$ and s is the shear produced by the GP gratings. A second lens with focal length F can transform the two wavefields back to the image plane and so Eq. 5.1 and 5.2 become

$$U_1 = \frac{1}{\sqrt{2}} U(x, y) e^{i2\pi f_0 x} \tag{5.3}$$

and

$$U_2 = \frac{1}{\sqrt{2}} U(x, y) e^{-i2\pi f_0 x} \tag{5.4}$$

When these two wavefields pass through a linear polarizer, they interfere, and the final intensity is given as:

$$I(x, y) = [U_1 + U_2][U_1 + U_2]^*$$

$$I(x, y) = I_1 + I_2 + 2Re[U_1 U_2^*]$$

$$I(x, y) = |U(x, y)|^2 + |U(x, y)|^2 \cos(4\pi f_0 x) \tag{5.5}$$

Eq. 5.5 shows that an interferometric shearing system at the Fourier plane, produces a perfect sinusoidal modulation.

The shear in X and Y directions in this system is a function of the distance between the gratings (Z_G) and the orientation of the gratings. This directly affects the value of f_0 in Eq. 5.5. With the gratings mounted on a rotational mount, the system enables variable fringe spacing by changing the spacing Z_G between the gratings and also variable fringe orientation through grating rotation. This is demonstrated in Figure 5.2. Furthermore, since the system requires the use of a linear polarizer to produce interference, this grating pair can also be set up in tandem with polarization phase shifting by rotating the linear polarizer. This is shown in Figure 5.3.

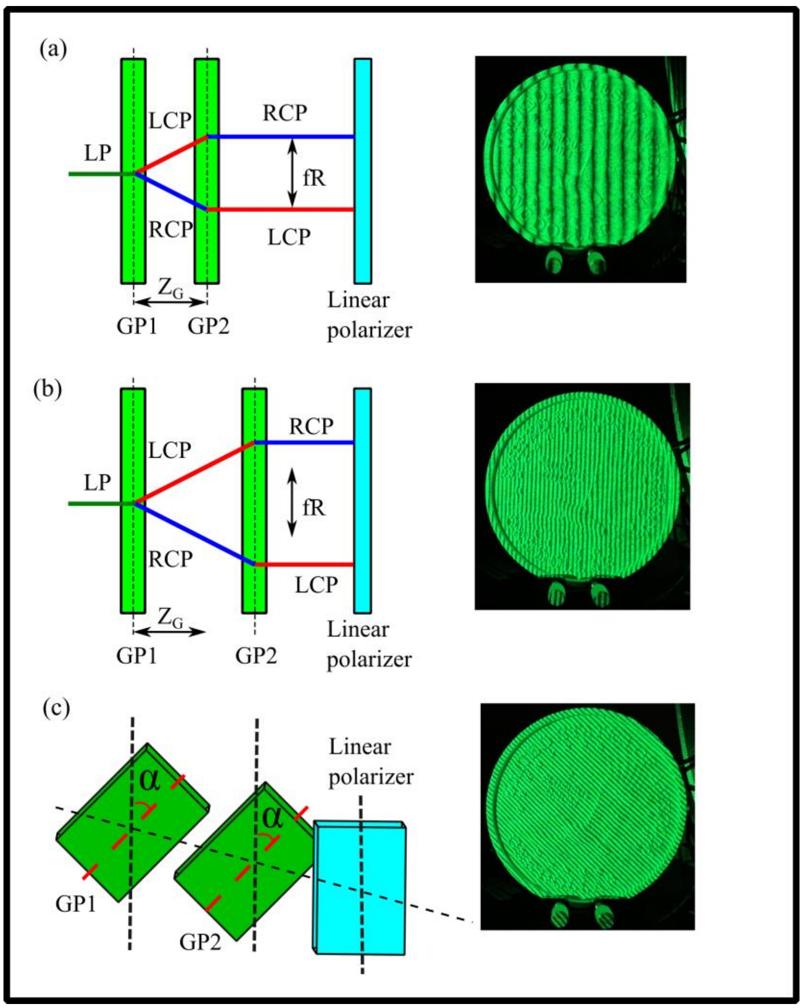

FIGURE 5.2: Effect of grating positions on projected Fringes. (a) Original orientation of gratings, (b) Changing the distance between gratings changes fringe spacing, (c) Grating pair orientation affects the fringe orientation.

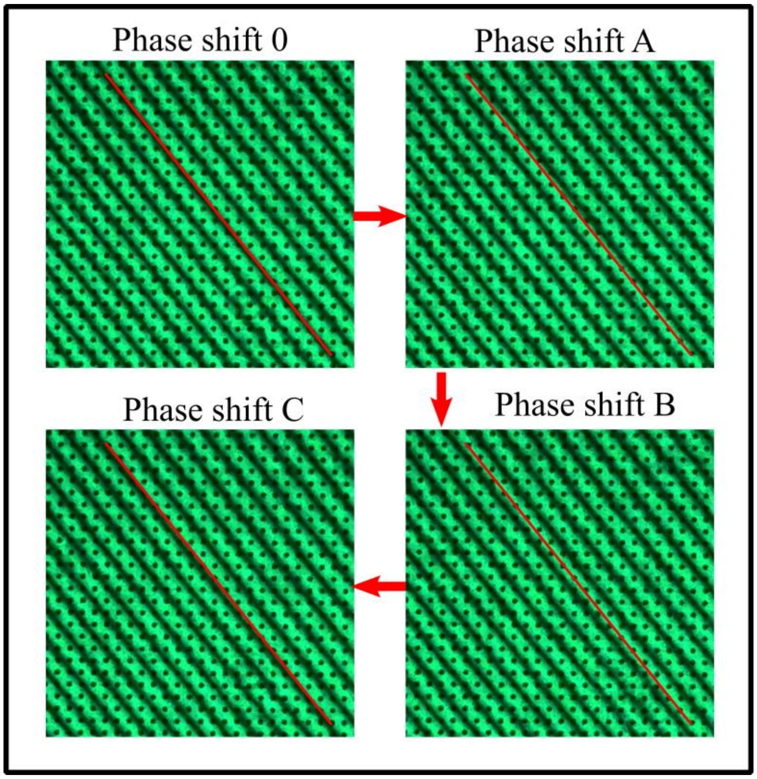

FIGURE 5.3: Fringe patterns at four different angles of linear polarizers demonstrating phase shifting

5.3. Experimental Setup

Figure 5.4a shows the schematic and Figure 5.4b shows the experimental setup used for the fringe projection experiments. The light source used is a class 3B, 520 nm wavelength, 30 mW green laser collimated with a 40 mm focal length triplet lens. The object used for the study is a 3-inch replica of a one-dollar coin and a 3D printed PLA plate with the Charlotte logo. The objects used for the experiment were painted with white acrylic to improve the scattering properties of the surface for the experiment and are shown in Figure 5.5. The GP gratings used for the experiment were from Edmund Optics (#12-677). The GP grating pair were mounted on a Thorlabs ELL14K rotation piezoelectric resonant motor. The motor was placed right before the Fourier plane of the 4f setup. The 4f setup was made with a 50 mm focal length and a 100 mm focal length lenses. The gratings were placed in the Fourier plane to minimize the area of interaction between the input wavefield and the gratings to mitigate any distortions from external stresses applied to the gratings. The 4f setup with the grating pairs produces two collimated sheared wavefields. A variable aperture was placed next to the GP grating pair to block any higher-order diffractions from the gratings. Under this setup, there is a limitation on the distance between the gratings over which the sheared beams stop overlapping. This limitation is removed by using a lens with a short focal length (20 mm) after the 4f setup. This lens expands both beams indefinitely enabling the beams to overlap irrespective of the separation distance between the gratings. The output beams are left and right circularly polarized. Using a linear polarizer at the end of the setup brings both beams to a linear polarized state and the wavefields interfere to produce linear fringe patterns on the object. These fringe patterns are projected onto the object which is placed at 45 degrees to the optical axis of the fringe projection setup. The projected fringes are recorded using a FLIR FL3-U3-13E4M-C monochrome camera with a 50 mm focal length camera lens. Linear fringe patterns were projected on the object and were recorded by the camera.

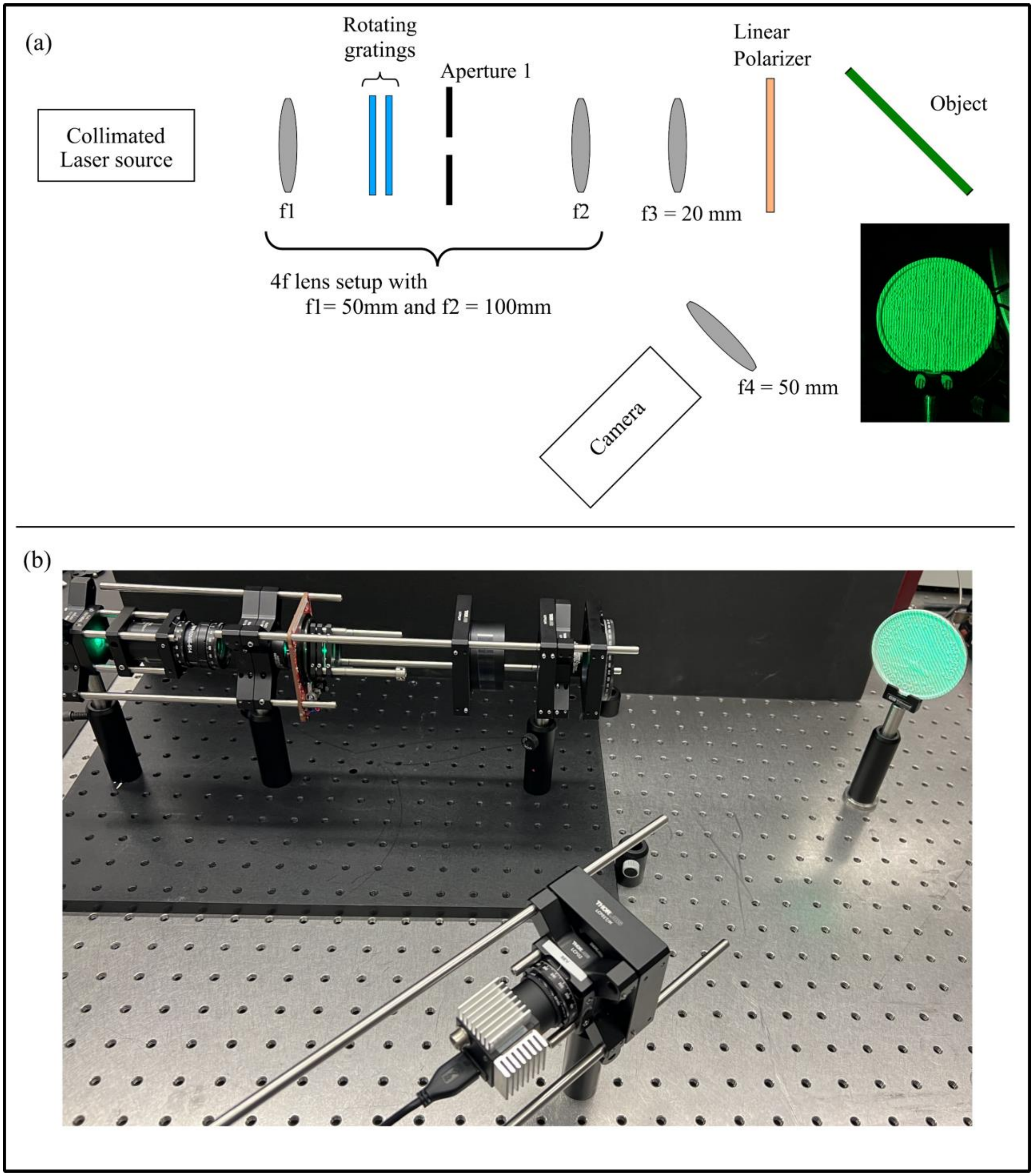

FIGURE 5.4: Fringe projection. (a) Schematic of the setup, (b) Experimental setup

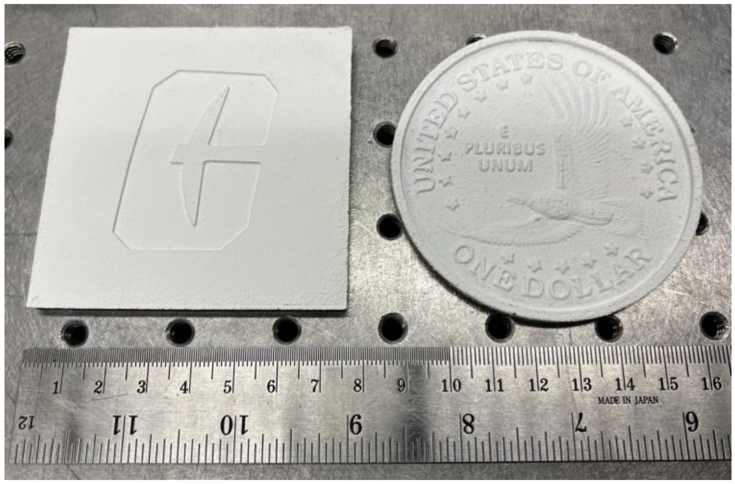

FIGURE 5.5: Objects used for fringe projection experiment

5.4. Results

The recorded intensity maps were processed using a Fourier transform phase estimation technique proposed by Takeda et. al. in [41] and the phase maps were reconstructed. To reconstruct the phase free from system distortions and errors, a reference phase was created by recording the fringe patterns on a flat ceramic plate placed at the same angle as the object with respect to the optical axis of the system. The phase maps were recovered from both the objects and the reference flat ceramic plate, and the final phase map was recovered by subtracting the reference phase map from the object phase maps. This is demonstrated in Figure 5.6. Figure 5.6a shows the intensity map of the fringe patterns projected on the coin. The fringe patterns are of very high frequency and can be seen on a zoomed image in Figure 5.6a. Figure 5.6b shows the distortions and errors in the phase map from the system and is considered the reference phase map. Figure 5.6c is the phase map acquired from the projected fringes on the coin. Some similarities can be seen in the phase maps in Figures 5.6b and 5.6c due to the presence of system errors in the recovered phase map shown in Figure 5.6b. Figure 5.6d shows the resulting phase map after subtracting the reference phase map (Figure 5.6b) from the coin phase map (Figure 5.6c) and Figure 5.6e shows the unwrapped phase map of the object.

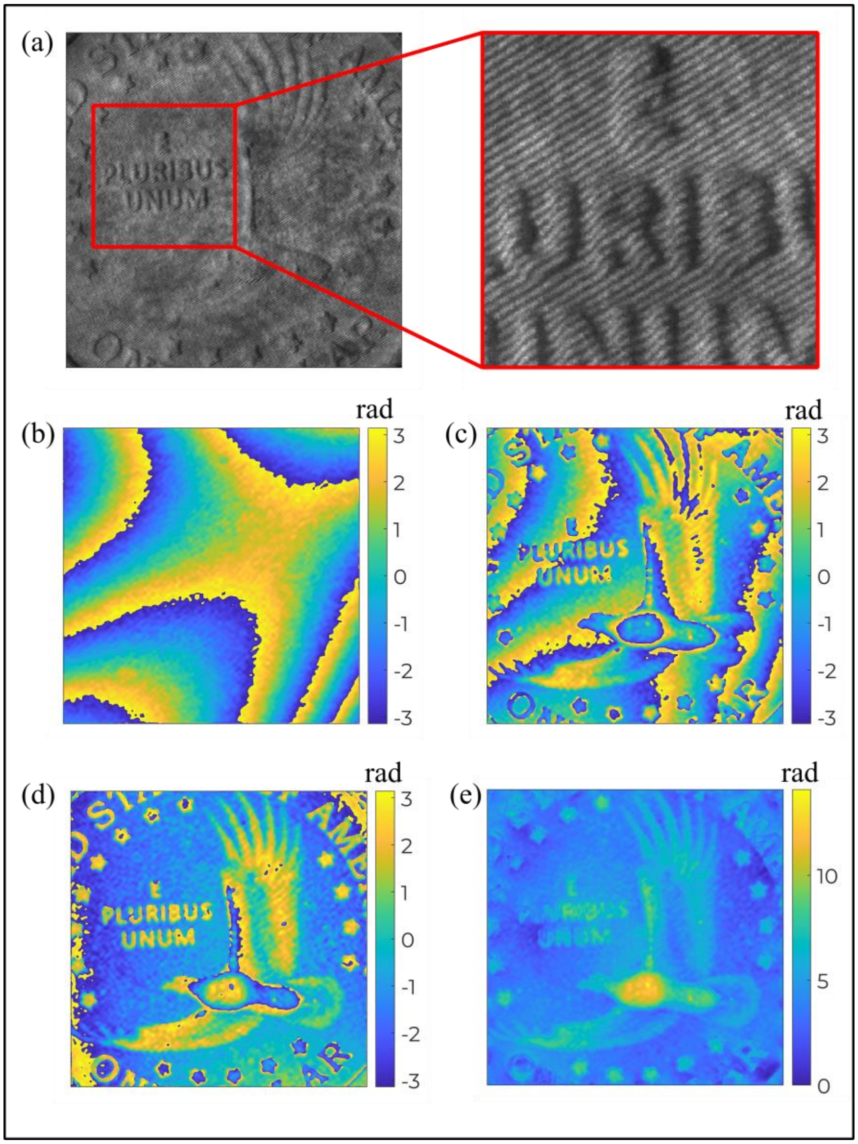

FIGURE 5.6: Recovered phase maps using the fringe projection system on coin replica. (a) Intensity map as acquired by the camera with a zoomed image showing fringe patterns, (b) Phase map of reference flat, (c) Phase map of the object (coin), (d) Final wrapped phase map after subtracting reference phase map from the object phase map, (e) Unwrapped phase map.

Similar experiments were conducted on a second object (3D printed PLA plate with Charlotte logo). The 3D-printed object was also coated with white acrylic paint to enhance the scattering properties of the surface as shown in Figure 5.5. The experiment was repeated by projecting fringes on the object and the images were recorded and processed. The phase maps recovered from Fourier transform phase estimation by Takeda et. al. [41] and unwrapped phase maps are shown in Figure 5.7.

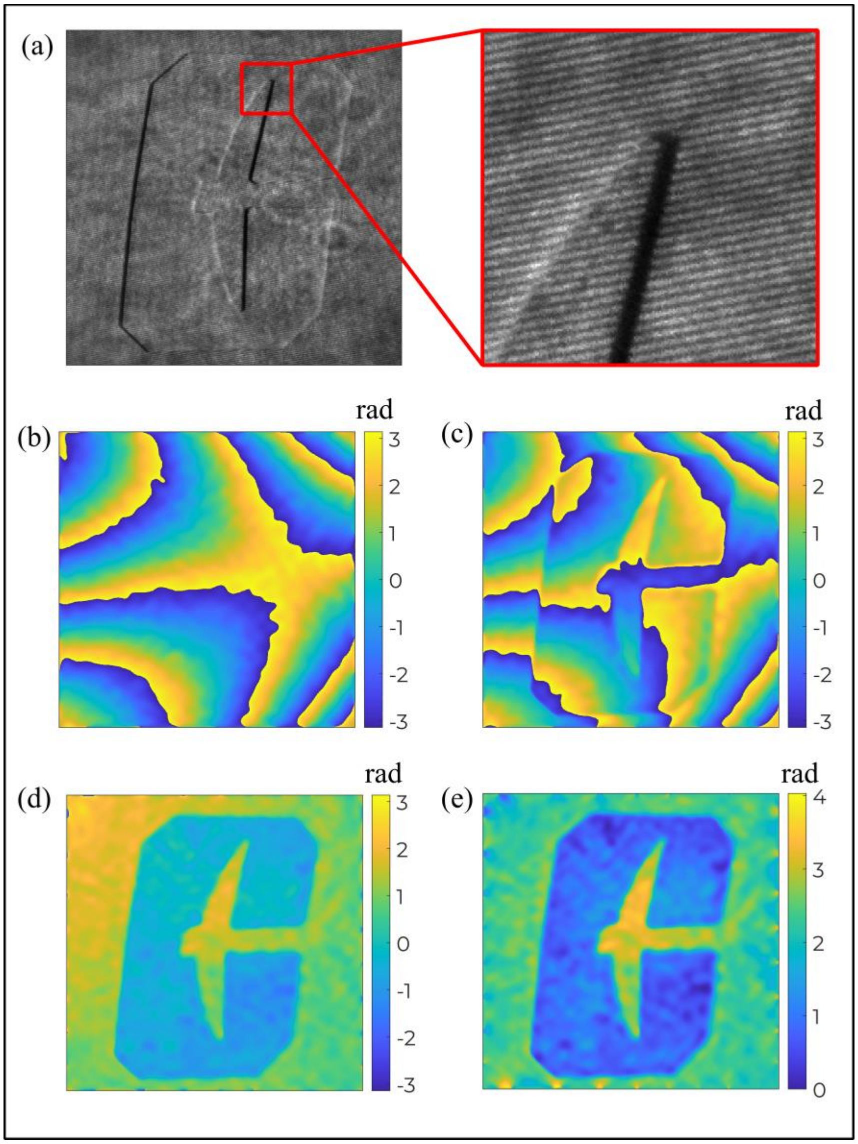

FIGURE 5.7: Recovered phase map of 3D printed plate showing Charlotte logo. (a) Projected fringe patterns on the 3D printed plate with a zoomed images showing fringes, (b) Recovered phase map of reference flat showing system distortions, (c) Recovered phase map of 3D printed plate, (d) Final wrapped phase map after subtracting reference phase map, (e) Unwrapped phase map.

Figure 5.7a shows the intensity map as recorded by the camera. Figure 5.7b shows the phase map of the system errors as recorded when the fringes are projected on a flat plate. Figure 5.7c also shows these errors along with the logo printed on the PLA plate. Figure 5.7d shows the wrapped phase map after subtracting the reference phase map (Figure 5.7b) from the object phase map (Figure 5.7c). The unwrapped phase map in Figure 5.7e shows a clear distinction between the top surface topography and bottom surface topography of the logo enabling measurement of step heights along the contour of the logo. An example step height feature is shown in Figure 5.8 and is compared to a measurement from a Zygo Nexview coherence scanning interferometer on the same region. Figure 5.8a shows the region on the object where the step heights were compared. The step height measurement on the Zygo Nexview reported a value of 600 µm for Figure 5.8b. Figure 5.8c shows the unwrapped phase map from the fringe projection system. The phase values in Figure 5.8c varied between 2.3 radians and 2.5 radians on the top layer while the bottom surface varied between 0.6 radians and 0.8 radians. So, the average step height was 1.7 radians in Figure 5.8c.

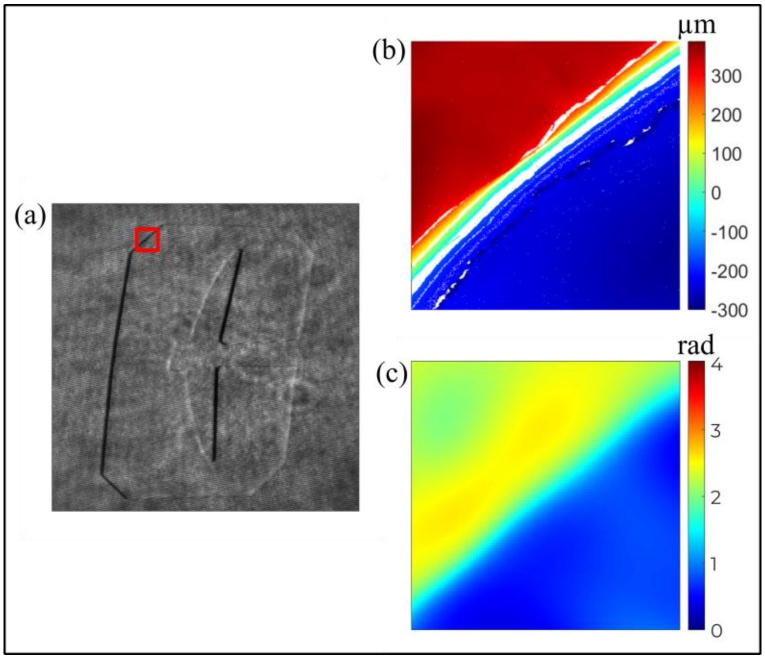

FIGURE 5.8: Step height comparison. (a)Intensity map of 3D printed plate highlighting region of comparison, (b) Measurement from Zygo Nexview coherence scanning interferometer, (c) Measurement from Fringe projection system

5.5. Applications of the setup

The setup was shown to have the capabilities to change fringe spacing and fringe orientation in Figure 5.2. The distance between the grating can be changed to adjust the fringe spacing. The gratings were mounted on a motorized rotational mount. So, rotating the grating enables different fringe orientations. The setup was also shown to have the ability to employ phase shifting techniques (Figure 5.3) and was shown to work with single shot techniques like Takeda's Fourier spectrum phase recovery method (Figures 5.6 and 5.7). The fringe spacing is a function of the separation distance between the gratings in the pair. In such designs, the maximum separation distance between the gratings is limited by the beam diameter beyond which the beams stop overlapping to produce fringe patterns. The presence of the short focal length lens in the proposed system after the 4f setup causes the overlapping beams to expand indefinitely and so, the beams will continue to overlap irrespective of the distance between the gratings. This allows for a large separation distance between the gratings which enables high-frequency fringe patterns to be produced. Figure 5.9 shows this capability. The object used in Figure 5.9 is a 3" x 3" low reflective grid distortion Target (Edmund optics #62-954). The diameter of the dots in the target is 0.5 mm and the center-to-center spacing between the dots is 1 mm. The fine fringes in Figure 5.9c show an average of 3 to 4 fringes between two consecutive dots. This indicates a fringe spacing between 250 μm and 330 μm.

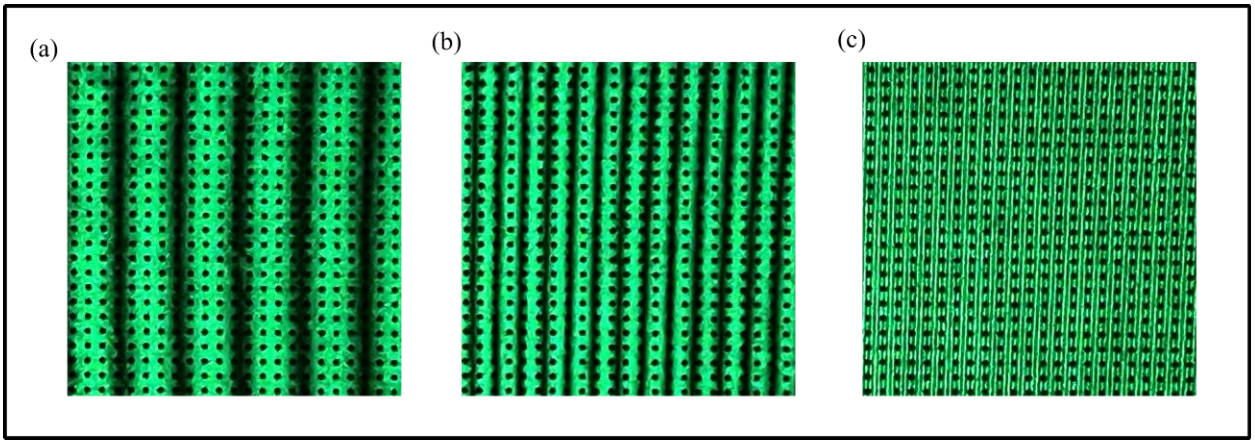

FIGURE 5.9: Demonstrating the ability to produce different fringe spacing. (a) Large spacing , (b) Medium spacing, (c) Sub-millimeter spacing

Due to the use of the short focal length lens at the end of the setup, this setup also enables projecting fringes on objects of different scales. The objects on which this fringe projection system was tested are shown in Figure 5.5. The coin replica is a 3-inch diameter disk and the 3D printed PLA plate is a 3” x 3” square plate. Figure 5.10 demonstrates the use of these setups on a much larger scale. The fringes were projected in a classroom in Duke Centennial Hall at the University of North Carolina at Charlotte. Figure 5.10a shows low-frequency fringes which can be visibly seen. Figure 5.10b shows the same classroom with a calibration board at the end of the room. The distance between the fringe projection setup and the calibration board is approximately 20 meters. The fringes are of very high frequency that cannot be visibly observed in Figure 5.10b unless viewed up close as shown in Figure 5.10c. The calibration board used in this demonstration has dots with a diameter 10 mm and the center-to-center distance between the dots was 30mm. The ability to change fringe spacing over such a large area by adjusting the separation distance between the gratings and also by changing the focal length of the last lens (short focal lens), expands the potential applications of this setup in different fields for large form measurements.

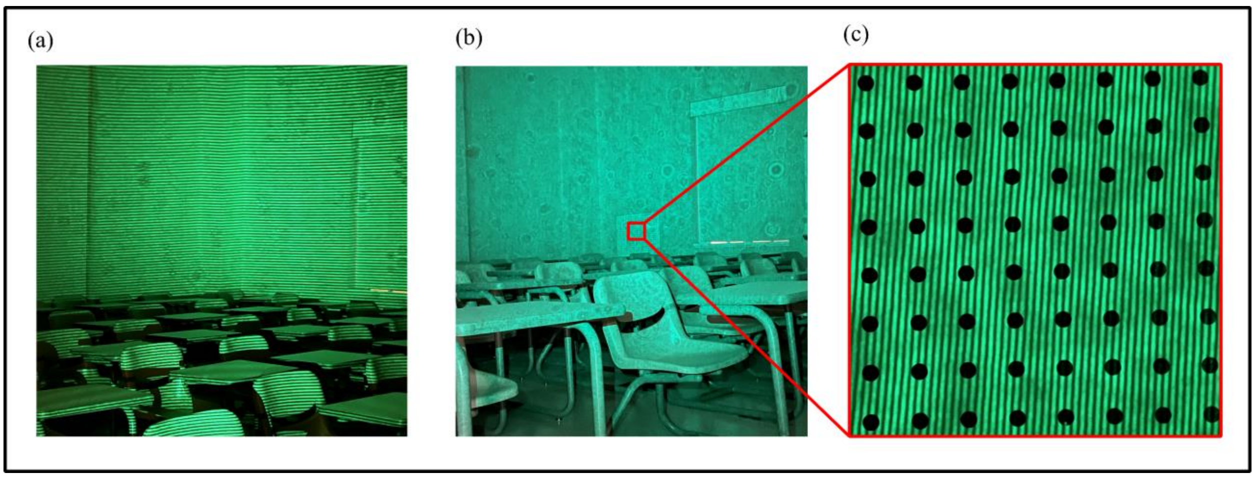

FIGURE 5.10: Use of the proposed fringe projection system at larger scales. (a) Low frequency visible fringes projected in a classroom, (b) High frequency fringes projected on calibration board placed at 20 meters from the fringe projection system, (c) Zoomed view of the calibration board showing the projected fringes.

5.6. Conclusion

The setup presented in this paper using GP grating pair mounted on a rotational mount offers the flexibility to work with adjustable fringe spacing and fringe orientations. The system is capable of producing sub-millimeter fringe spacing and can be used for very large field of views extending over several meters. The versatility of different fringe characteristics comes from the property that the fringe properties can be changed by just adjusting the distance between the grating pairs and the grating pair rotation. The use of a coherent light source produces high-contrast fringe patterns for large measurement volumes without losing fringe contrasts. The common-path interferometric design enables the system to be robust to environmental effects. Depending on the object surface being measured, the use of coherent light might produce speckles. Further investigations into mitigating the speckle effect through post-processing can improve the efficiency of the proposed fringe projection setup. Applications for this work are found in in-situ measurements for laser powder bed fusion, where sub-millimeter fringe periods are required for large field of views.

REFERENCES

1. M. M. P. A. Vermeulen, P. C. J. N. Rosielle, and P. H. J. Schellekens, "Design of a High-Precision 3D-Coordinate Measuring Machine," CIRP Ann. **47**, 447–450 (1998).

2. E. J. C. Bos, "Aspects of tactile probing on the micro scale," Precis. Eng. **35**, 228–240 (2011).

3. M. B. Bauza, S. C. Woody, B. A. Woody, and S. T. Smith, "Surface profilometry of high aspect ratio features," Wear **271**, 519–522 (2011).

4. H. Zhao, J.-P. Kruth, N. Van Gestel, B. Boeckmans, and P. Bleys, "Automated dimensional inspection planning using the combination of laser scanner and tactile probe," Measurement **45**, 1057–1066 (2012).

5. K. Venditti, C. Evans, K. Falaggis, A. Blum, R. Chaudhuri, J. Goodsell, and J. P. Rolland, "Design for metrology for freeform optics manufacturing," Procedia CIRP **84**, 169–172 (2019).

6. Y. Surrel, "Design of algorithms for phase measurements by the use of phase stepping," Appl. Opt. **35**, 51 (1996).

7. Z. Wang and B. Han, "Advanced iterative algorithm for phase extraction of randomly phase-shifted interferograms," Opt. Lett. **29**, 1671 (2004).

8. A. Albertazzi, A. V. Fantin, D. P. Willemann, and M. E. Benedet, "Phase Maps Retrieval from Sequences of Phase Shifted Images with Unknown Phase Steps Using Generalized N-Dimensional Lissajous Figures—Principles and Applications," Int. J. Optomechatronics **8**, 340–356 (2014).

9. E. R. Cochran, "Limitations of phase-measuring interferometry for surface characterization and testing: a review," in *Interferometry: Surface Characterization and Testing*, K. Creath and J. E. Greivenkamp, eds. (1992), Vol. 1776, pp. 151–157.

10. C. Falldorf, M. Agour, and R. B. Bergmann, "Advanced wave field sensing using computational shear interferometry," Interferom. XVII Adv. Appl. **9204**, 92040C (2014).

11. P. Shanmugam, A. Light, A. Turley, and K. Falaggis, "Variable shearing holography with applications to phase imaging and metrology," Light Adv. Manuf. **3**, 1 (2022).

12. P. Pavliček and O. Hýbl, "White-light interferometry on rough surfaces—measurement uncertainty caused by noise," Appl. Opt. **51**, 465 (2012).

13. P. Pavliček and O. Hýbl, "White-light interferometry on rough surfaces--measurement uncertainty caused by surface roughness," Appl. Opt. **47**, 2941–2949 (2008).

14. K. Choi, J. Yim, and S.-W. Min, "Achromatic phase shifting self-interference incoherent digital holography using linear polarizer and geometric phase lens," Opt. Express **26**, 16212 (2018).

15. J. Geng, "Structured-light 3D surface imaging: a tutorial," Adv. Opt. Photonics **3**, 128 (2011).

16. J. Burke, T. Bothe, W. Osten, and C. F. Hess, "Reverse engineering by fringe projection," in *Interferometry XI: Applications*, W. Osten, ed. (2002), Vol. 4778, p. 312.

17. J. Salvi, J. Pagès, and J. Batlle, "Pattern codification strategies in structured light systems," Pattern Recognit. **37**, 827–849 (2004).

18. M. Servin, J. A. Quiroga, and M. Padilla, *Fringe Pattern Analysis for Optical Metrology: Theory, Algorithms, and Applications* (Wiley, 2014).

19. K. A. Nugent, D. Paganin, and T. E. Gureyev, "A Phase Odyssey," Phys. Today **54**, 27–32 (2001).

20. J. Martinez-Carranza, K. Falaggis, and T. Kozacki, "Multi-filter transport of intensity equation solver with equalized noise sensitivity," Opt. Express **23**, 23092 (2015).

21. C. G. Treviño-Palacios, "Unfolding wrapped phase," Opt. Eng. **54**, 110503 (2015).

22. R. M. Goldstein, H. A. Zebker, and C. L. Werner, "Satellite radar interferometry: Two-dimensional phase unwrapping," Radio Sci. **23**, 713–720 (1988).

23. D. C. Ghiglia and M. D. Pritt, *Two-Dimensional Phase Unwrapping: Theory, Algorithms, and Software* (Wiley, 1998).

24. T. J. Flynn, "Two-dimensional phase unwrapping with minimum weighted discontinuity," J. Opt. Soc. Am. A **14**, 2692 (1997).

25. M. A. Herráez, D. R. Burton, M. J. Lalor, and M. A. Gdeisat, "Fast two-dimensional phase-unwrapping algorithm based on sorting by reliability following a noncontinuous path," Appl. Opt. **41**, 7437 (2002).

26. L. da Silva Maciel and A. G. Albertazzi, "Swarm-based algorithm for phase unwrapping," Appl. Opt. **53**, 5502 (2014).

27. W. Nadeborn, P. Andrä, and W. Osten, "A robust procedure for absolute phase measurement," Opt. Lasers Eng. **24**, 245–260 (1996).

28. C. Wagner, S. Seebacher, W. Osten, and W. Jüptner, "Digital recording and numerical reconstruction of lensless Fourier holograms in optical metrology," Appl. Opt. **38**, 4812 (1999).

29. K. Falaggis, D. P. Towers, and C. E. Towers, "Algebraic solution for phase unwrapping problems in multiwavelength interferometry," Appl. Opt. **53**, 3737 (2014).

30. K. Falaggis, D. P. Towers, and C. E. Towers, "Method of excess fractions with application to absolute distance metrology: theoretical analysis," Appl. Opt. **50**, 5484 (2011).

31. R. Porras-Aguilar and K. Falaggis, "Absolute phase recovery in structured light illumination systems: Sinusoidal vs. intensity discrete patterns," Opt. Lasers Eng. **84**, 111–119 (2016).

32. R. Porras-Aguilar, K. Falaggis, and R. Ramos-Garcia, "Error correcting coding-theory for structured light illumination systems," Opt. Lasers Eng. **93**, 146–155 (2017).

33. H. Xu, L. Wang, S. Tabata, Y. Watanabe, and M. Ishikawa, "Extended depth-of-field projection method using a high-speed projector with a synchronized oscillating variable-focus lens," Appl. Opt. **60**, 3917 (2021).

34. B. F. Oreb and R. G. Dorsch, "Profilometry by phase-shifted Talbot images," Appl. Opt. **33**, 7955 (1994).

35. S. Yoneyama, "Three-dimensional surface profile measurement of a moving object by a spatial-offset phase stepping method," Opt. Eng. **42**, 137 (2003).

36. V. Moreau, D. Laboury, B. Tilkens, and Y. L. M. Renotte, "Interferometric fringes projection system for 3D profilometry and relief investigation," in *Optical Methods for Arts and Archaeology*, R. Salimbeni and L. Pezzati, eds. (2005), Vol. 5857, p. 58570A.

37. E. Stoykova, G. Minchev, and V. Sainov, "Fringe projection with a sinusoidal phase grating," Appl. Opt. **48**, 4774 (2009).

38. C. Quan, C. J. Tay, X. Kang, X. Y. He, and H. M. Shang, "Shape measurement by use of liquid-crystal display fringe projection with two-step phase shifting," Appl. Opt. **42**, 2329 (2003).

39. F. Wu, H. Zhang, M. J. Lalor, and D. R. Burton, "A novel design for fiber optic interferometric fringe projection phase-shifting 3-D profilometry," Opt. Commun. **187**, 347–357 (2001).

40. J. R. Sánchez, A. Martínez-García, J. A. Rayas, and M. León-Rodríguez, "LED source interferometer for microscopic fringe projection profilometry using a Gates' interferometer configuration," Opt. Lasers Eng. **149**, 106822 (2022).

41. M. Takeda, H. Ina, and S. Kobayashi, "Fourier-transform method of fringe-pattern analysis for computer-based topography and interferometry," J. Opt. Soc. Am. **72**, 156 (1982).

42. P. Blain, P. Piron, Y. Renotte, and S. Habraken, "An in-line shearography setup based on circular polarization gratings," Opt. Lasers Eng. **51**, 1053–1059 (2013).

43. P. Shanmugam, A. Light, A. Turley, and K. Falaggis, "Variable shearing holography with geometric phase elements," in *Interferometry XXI*, M. B. North-Morris, K. Creath, and R. Porras-Aguilar, eds. (SPIE, 2022), p. 21.

CHAPTER 6: CONCLUSION AND FUTURE WORK

The focus of the dissertation is to design, develop and characterize interferometric holography systems based on shear interferometry that records interferograms through lateral shearing and reconstruct the object wavefield through an iterative optimization process. To our knowledge, based on the available literature, this is the first study to design, develop and characterize the effects of shears in a GP gratings-based coherent shear interferometry system for reflective and transmissive objects. The second objective of this dissertation is to further explore and expand potential applications of using GP grating pairs to perform fringe projection and extend this study to measure diffused surfaces as well.

Chapter 2 focuses on the shear interferometry system. Two designs for shear interferometry were discussed in this chapter by placing the GP grating pairs in different configurations and their performance was compared. These two designs varied in methods for shear selection for recording the interferograms and reconstructing the complex wavefield. The effect of shear selection was studied using synthetic data and verified by defining two transfer functions namely, spatial information density function (SIDF) and frequency information density function (FIDF). The SIDF identifies potential regions in the phase map where reconstructions could fail based on the overlap of the interfering beams while the FIDF identifies potential surface frequencies that the algorithm could fail to reconstruct. After studying and mitigating the artifacts created by the algorithm, the stability of the algorithm was also studied through Monte Carlo simulations. Chapter 2 concludes by demonstrating a holography system by recording a wavefield in a defocused plane and bringing the wavefield into refocus using numerical refocusing techniques.

Chapter 3 studies the limitations offered by the spatial information density function. The chapter concludes that the complex cross-term used in the alternating projection algorithm during wavefield reconstruction has phase information only in regions where the sheared object beams overlap. The presence of zero regions in the SIDF map indicates that no phase information will be recovered in these regions. However, this chapter also shows that the complex cross-term still has amplitude information, and the reconstruction algorithm can still successfully generate the amplitude map. So, in the absence of object beam overlap, the system functions as an amplitude imager.

Chapter 4 studies effective shear selection methods for optimal wavefield reconstruction with minimal errors. This study was done using synthetic intensity maps created by shearing a synthetically generated defocused point source wavefield. Although few studies exist in the literature that addresses the effect of individual shears on the reconstruction of different surface frequencies, to our knowledge, this is the first study that studies the combined effect of shears and provides strategies for shear selection for effective wavefield reconstruction. The study is done through simulations of a defocused point source wavefield reconstruction under varying shear conditions and the results are analyzed through a statistical analysis to highlight the major findings.

Chapters 2 and 3 discuss the use of GP gratings for shear interferometry and holography system suitable for reflective and transmissive surfaces. Chapter 4 discusses effective shear selection methods for the shear holography system. Chapter 5 expands the study to diffused surfaces by converting the system into a fringe projection system. The fringe projection system proposed and tested in this chapter has the flexibility to adjust the fringe patterns both in fringe orientation and also fringe spacing. The system can produce a wide range of fringe spacing varying from large spacing to sub-millimeter spacing. Further, the produced fringe patterns can be projected on objects of a wide range of sizes. This was demonstrated by comparing projecting fringes on small objects such as 3D printed objects and replica coins and on large objects such as large calibration boards placed at 2 meters from the fringe projection setup in a classroom located in Duke Centennial Hall at the University of North Carolina at Charlotte.

The dissertation demonstrates the flexibility to use the GP grating pairs as both, a shear holography system that can measure transmissive and reflective surfaces and as a fringe projection system that can measure diffused surfaces.

The use of flat optics such as GP gratings and GP lenses to make compact and robust optical metrology systems is relatively a novel and emerging area of interest among researchers. Very few works are available in literature that have explored potential designs for implementing optical metrology systems using these types of optics [1–3]. This dissertation explores the use of GP grating pairs for holographic interferometric systems using a coherent light source to measure reflective and transmissive surfaces. Preliminary experiments using incoherent light sources, such as a green LED, showed problems with getting good fringe contrast. Further work could be explored on this aspect to extend the use of GP grating pair in holographic systems to measure diffused surfaces. Developing holography systems using GP grating pairs for diffused surfaces could enable the design of complex and hybrid systems that can measure all types of surfaces. Further, these system designs could be combined with systems that use GP lenses to make complex yet robust systems for different applications.

Another aspect of future works could focus on shear selection. To our knowledge, this dissertation is the first in the literature that explores existing works, such as [4,5] on correlating surface frequencies with individual shears and studies the combined effect of N shears (Chapter

2 and Chapter 3). Based on this study, Chapter 4 provides a fundamental approach to selecting the shears effectively. This work could still be expanded on to further optimize the shear selection strategy.

REFERENCES

1. K. Choi, J. Yim, and S.-W. Min, "Achromatic phase shifting self-interference incoherent digital holography using linear polarizer and geometric phase lens," Opt. Express **26**, 16212 (2018).

2. L. A. Alemán-Castaneda, B. Piccirillo, E. Santamato, L. Marrucci, and M. A. Alonso, "Shearing interferometry via geometric phase," Optica **6**, 396 (2019).

3. P. Shanmugam, A. Light, A. Turley, and K. Falaggis, "Variable shearing holography with applications to phase imaging and metrology," Light Adv. Manuf. **3**, 1 (2022).

4. M. Servin, M. Cywiak, and A. Davila, "Extreme shearing interferometry: Theoretical limits with practical consequences," Opt. Express **15**, 17805 (2007).

5. C. Falldorf, "Measuring the complex amplitude of wave fields by means of shear interferometry," J. Opt. Soc. Am. A **28**, 1636 (2011).

APPENDIX-A: JONES MATRIX FOR GP GRATINGS

The optical systems presented in this dissertation use geometric phase (GP) grating pairs to implement holographic shear interferometric system and fringe projection system. Appendix-A shows how different wavefields with different polarized states interact with GP grating pairs using Jones Calculus. As previously discussed in Chapter 1, the Jones matrix for the GP grating pair can be presented as two opposite circular polarizers with a phase difference $(\phi = \phi_2 - \phi_1)$ between them. The Jones matrix for the GP grating pair is shown in Eq.A.1.

$$J_{out} = \frac{j}{2}\left\{exp(j\phi_1)\begin{bmatrix}1 & +i\\ -i & 1\end{bmatrix} + exp(j\phi_2)\begin{bmatrix}1 & -i\\ +i & 1\end{bmatrix}\right\} \tag{A.1}$$

If the input to the GP grating pair is a linearly polarized light with a polarization angle α, the Jones vector for the input wavefield is

$$LP = \begin{bmatrix}1\\ \tan(\alpha)\end{bmatrix} \tag{A.2}$$

The interaction of the input wavefield (LP) with the GP grating pair is

$$J_{out}\cdot LP = \frac{j}{2}\left\{\exp(j\phi_1)\begin{bmatrix}1 & +i\\ -i & 1\end{bmatrix} + \exp(j\phi_2)\begin{bmatrix}1 & -i\\ +i & 1\end{bmatrix}\right\}\cdot\begin{bmatrix}1\\ \tan(\alpha)\end{bmatrix}$$

$$J_{out}\cdot LP = \frac{j}{2}\left\{\left(1 + jtan(\alpha)\right)\cdot\exp(j\phi_1)\cdot\begin{bmatrix}1\\ -j\end{bmatrix} + \left(1 - jtan(\alpha)\right)\cdot\exp(j\phi_2)\cdot\begin{bmatrix}1\\ j\end{bmatrix}\right\} \tag{A.3}$$

Eq. A.3 shows that when linear polarized wavefield at any polarization angle (α) interacts with the GP grating pair, the input light is split as a right circular polarized beam and a left circular polarized beam. The Jones vector for right circular polarized (RCP) beam and left circular polarized (LCP) beam are shown in equation (A.4).

$$RCP = \begin{bmatrix}1\\ -j\end{bmatrix} \quad ; \quad LCP = \begin{bmatrix}1\\ j\end{bmatrix} \tag{A.4}$$

Similarly, the interaction of a left circular polarized beam and right circular polarized beam with the GP grating pair produces outputs as shown in Eq.A.5 and Eq.A.6.

$$J_{out} \cdot RCP = \frac{j}{2}\left\{\exp(j\phi_1)\begin{bmatrix}1 & j\\ -j & 1\end{bmatrix} + \exp(j\phi_2)\begin{bmatrix}1 & -j\\ j & 1\end{bmatrix}\right\} \cdot \begin{bmatrix}1\\ -\mathrm{j}\end{bmatrix} = j \cdot \exp(j\phi_1) \cdot \begin{bmatrix}1\\ -\mathrm{j}\end{bmatrix} \quad \text{(A.5)}$$

$$J_{out} \cdot LCP = \frac{j}{2}\left\{\exp(j\phi_1)\begin{bmatrix}1 & j\\ -j & 1\end{bmatrix} + \exp(j\phi_2)\begin{bmatrix}1 & -j\\ j & 1\end{bmatrix}\right\} \cdot \begin{bmatrix}1\\ \mathrm{j}\end{bmatrix} = j \cdot \exp(j\phi_2) \cdot \begin{bmatrix}1\\ \mathrm{j}\end{bmatrix} \quad \text{(A.6)}$$

Eqs. A.5 and A.6 show that the GP grating pair preserve the polarization state when the input is a circular polarized wavefield.

Eqs. A.3, A.5 and A.6 show how the GP grating-pair affects the polarization states of the input wavefield. When a linearly polarized beam passes through a GP grating pair, it is split into left and right circular polarized beams (Eq. A.3). When a left or right circular polarized beam passes through a GP grating pair, the polarization state is preserved (Eq. A.5 and A.6). In addition to the effects on the polarization state of the input beam, a GP grating pair also laterally shifts the position of the output beam depending on its polarization state and the orientation of the GP grating pair. The magnitude of lateral shift depends on the separation distance between the gratings in the grating pair, and the orientation of lateral shift depends on the grating orientation. For a fixed separation distance between the gratings in the pair, the left and right circular polarized beams are laterally and symmetrically shifted about the optical axis. In other words, if the left circular polarized beam is shifted by a lateral distance 's', then the right circular polarized beam is shifted by a lateral distance '-s'. This effect can be presented using J_{out} from Eq. A.1 as shown in Eq. A.7

$$[Output\ wavefield] = (\, J_{out} \cdot [Input\ wavefield]\,) * f(s,\theta) \quad \text{(A.7)}$$

where $f(s,\theta)$ is a function lateral shear 's' and grating angle θ.

The output wavefield, according to Eq. A.7, is a convolution of the matrix from Jones calculus with a function $f(s, \theta)$ to laterally shift the output beam by $\pm s$ depending on its polarization state, and along the orientation θ depending on the orientation of the GP grating pair.

APPENDIX-B: JONES CALCULUS FOR POLARIZATION PHASE SHIFTING

The phase shifting used in this dissertation is based on polarization phase shifting. Appendix-A demonstrates the relation between polarization shift angle (δ) and phase shift angle (θ) through Jones Calculus, while recording the interferograms. The GP grating pair splits a linearly polarized object wavefield into a right circular polarized (RCP) beam and a left circular polarized (LCP) beam. The LCP and RCP beam overlap on the detector plane of a polarized camera. Each pixel on the polarized camera records the signal at a fixed polarization state. The polarization angle (δ) defines the phase shift angle (θ) introduced between the overlapping wavefields.

The Jones matrix for a linear polarizer at polarization angle (δ) is shown in Eq. B.1.

$$LP = \begin{bmatrix} \cos^2(\delta) & \cos(\delta)\sin(\delta) \\ \cos(\delta)\sin(\delta) & \sin^2(\delta) \end{bmatrix} \tag{B.1}$$

The LCP and RCP wavefields from the GP grating pair are shown in Eq.B.2 and Eq.B.3.

$$LCP = \begin{bmatrix} 1 \\ j \end{bmatrix} \exp(j\phi_1) \tag{B.2}$$

$$RCP = \begin{bmatrix} 1 \\ -j \end{bmatrix} \exp(j\phi_2) \tag{B.3}$$

The wavefields $u_1(x)$ and $u_2(x)$ after passing through the linear polarizer are shown in Eq.B.4 and Eq.B.5.

$$u_1(x) = LP \times LCP = \begin{bmatrix} \cos(\delta) \\ \sin(\delta) \end{bmatrix} \exp(j\phi_1 + j\delta) \tag{B.4}$$

$$u_2(x) = LP \times RCP = \begin{bmatrix} \cos(\delta) \\ \sin(\delta) \end{bmatrix} \exp(j\phi_2 - j\delta) \tag{B.5}$$

The resulting wavefield $u(x)$ from $u_1(x)$ and $u_2(x)$ is shown in Eq.B.6.

$$u(x) = |u_1(x)|^2 + |u_2(x)|^2 + u_2^*(x)u_1(x) + u_1^*(x)u_2(x)$$

$$u(x) = 2 + 2\cos(2\delta + \Delta\phi) \tag{B.6}$$

From Eq. B.6, it can be concluded that

$$2\ \times polarization\ angle\ shift\ (\delta) = phase\ shift\ (\theta) \tag{B.7}$$

The polarization camera uses super-pixels each with 4 pixels having polarization angles 0, 45, 90 and 135 degrees. This results in producing phase shifts of 0, 90, 180 and 270 degrees.

Eqs. B4 and B5 were derived by considering only the effect of GP gratings on the polarization states of the input beams. If the lateral shift effect, as discussed in Appendix-A, is considered here, then Eqs B.4 and B.5 can be rewritten as Eqs. B.8 and B.9.

$$u_1(x+s) = LP\ \times LCP = \left\{ \begin{bmatrix} \cos(\delta) \\ \sin(\delta) \end{bmatrix} \exp(j\phi_1 + j\delta) \right\} * f(s,\theta) \tag{B.8}$$

$$u_2(x-s) = LP\ \times RCP = \left\{ \begin{bmatrix} \cos(\delta) \\ \sin(\delta) \end{bmatrix} \exp(j\phi_2 - j\delta) \right\} * f(s,\theta) \tag{B.9}$$

where convolving with the function $f(s,\theta)$ laterally shifts the output beam by magnitude $\pm s$ depending on the polarization state and in orientation θ depending on the orientation of the grating pair.

The resulting wavefield $u(x)$ from $u_1(x+s)$ and $u_2(x-s)$ is shown in Eq.B.10.

$$u(x) = |u_1(x+s)|^2 + |u_2(x-s)|^2 + u_2^*(x-s)\cdot u_1(x+s) + u_1^*(x+s)\cdot u_2(x-s)$$

$$u(x) = |u_1(x+s)|^2 + |u_2(x-s)|^2 + 2Re\{u_1^*(x+s)\cdot u_2(x-s)\} \tag{B.10}$$

Eq. B.10 shows that the interference occurs only in the regions of overlap between the wavefields $u_1(x+s)$ and $u_2(x-s)$. Simplifying Eq. B.10 results in the same equation as Eq. B.6 and ends with the same conclusion as Eq. B.7 in the regions overlapped by the wavefields $u_1(x+s)$ and $u_2(x-s)$.